RICE UNIVERSITY

Electromechanical Investigation of Low Dimensional Nanomaterials for NEMS Applications

By

Hao Lu

A THESIS SUBMITTED
IN PARTIAL FULFILLMENT OF THE
REQUIREMENTS FOR THE DEGREE

Doctor of Philosophy

APPROVED, THESIS COMMITTEE

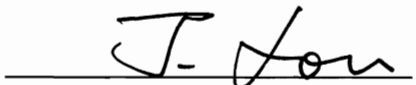

Dr. Jun Lou, advisor
Assistant Professor
Mechanical Engineering and Material Science

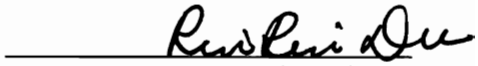

Dr. Rui-Rui Du
Professor
Physics and Astronomy

Dr. Qilin Li
Assistant Professor
Civil and Environmental Engineering

HOUSTON, TEXAS
DEC 2010

Abstract

Electromechanical Investigation of Low Dimensional Nanomaterials for NEMS Applications

By

Hao Lu

Successful operation of Nano-ElectroMechanical Systems (NEMS) critically depends on their working environment and component materials' electromechanical properties. It is equally important that ambient or liquid environment to be seriously considered for NEMS to work as high sensitivity sensors with commercial viabilities.

Firstly, to understand interaction between NEMS oscillator and fluid, transfer function of suspended gold nanowire NEMS devices in fluid was calculated. It was found that NEMS's resonance frequency decreased and energy dissipation increased, which constrained its sensitivity. Sensitivity limit of NEMS oscillators was also considered in a statistical framework. Subsequently, suspended gold nanowire NEMS devices were magnetomotively actuated in vacuum and liquid.

Secondly, electromechanical properties of gold nanowires were carefully studied and the observed size effect was found to agree with theory, which predicted small changes of electromechanical property compared with bulk gold materials.

Finally, it is well recognized that continuous development of new NEMS devices demands novel materials. Mechanical properties of new two-dimensional hexagonal

Boron Nitride films with a few atomic layers were studied. Outlook of utilizing ultrathin BN films in next generation NEMS devices was discussed.

Acknowledgement

I would like to greatly thank my advisor Dr. Jun Lou for his guidance and full support of my research. His critical scientific thinking and vision inspired my passion for research. I would also like to thank Dr. Yong P. Chen from Purdue University, for allowing me using his equipments in Purdue and inspiring talks. In addition, I would like to thank Dr. Li Song for his help and suggestions on my experiments and research. I owe great thanks to Dr. Zheng Liu for helping me setting up experiments and samples preparation.

I would like thank all colleagues I always enjoying working with. Luis Jauregui from Purdue University helped me with magnetomotive actuation of NEMS devices. I appreciate useful discussions with Dr. Lijie Ci, Dr. Yongjie Zhang, and my group members including but not limited to Yang Lu and Yogeeswaran Ganesan.

Last but not least, I would like to express my great thanks to my committee members Dr. Ruirui Du, Dr. Qilin Li.

Table of Contents

List of Figures

List of Tables

Chapter 1 Introduction

1.1 Introduction

Nanoelectromechanical devices (NEMS) are nano devices mechanically coupled with electrical control and sensing units. We have seen remarkable progresses in NEMS in recent years as sensors. Due to their sizes and large surface volume ratio, NEMS sensors achieved ultrahigh sensitivity of mass[1-2], gas[3], and force[4].

Among those NEMS sensors, the mechanical part is either excited to resonance (NEMS resonator) or remains static. NEMS resonator under high vacuum can reach radio frequency resonance and ultra high quality factor (Q), which is the reason for their ultrahigh sensitivity. While NEMS resonator's ultrahigh sensitivity in vacuum is promising for their potential use, there is still a larger area remaining untouched: in-situ chemical and biological sensors in liquid which is the environment the sensors will be deployed. When operated in ambient condition or liquid, both NEMS resonator's resonance frequency and Q factor drop significantly due to the high damping and thus their sensitivities are limited. A few pioneer works [5-6]have successfully demonstrated operation of NEMS resonators in high pressure gas or liquid. In this dissertation, I will analysis dynamics of NEMS resonators and study properties of novel nanomaterials and their potential as nanosensors.

1.2 NEMS resonators

Mechanical vibration is widely observed from unwanted bridge oscillation to desired vibration of guitar strings. Mechanical vibration can be deliberately generated as probes to

physical properties as viscosity[7], pressure[8]. While these large scale vibrators have been commercialized and massively fabricated, bringing down the size of vibration devices opens new gate to frontier of scientific research. Basic operation of vibrating sensors requires electromechanical actuation and mechanical sensing. In actuation part, electrical energy is transferred to mechanical energy and vice versa in sensing part. Generally speaking, the actuation and sensing of NEMS are transducers, which transfer energy in one form to another. Many actuation and sensing techniques have been demonstrated on numerous of NEMS devices. In the following sections, the theory of the sensors and actuation and detection techniques will be discussed.

1.2.1 Operation principal of NEMS

NEMS devices take various geometry forms depending on the materials been used; they can be simple beam[9-10], string[11], membrane[12] or other optimized shapes[13-14]. The following discussion restricted to simple beam structure.

When the NEMS deviates small distance from their equilibrium position, they could be modeled as simple harmonic oscillator (SHO) independent of their geometries. In SHO model, deformation shape of the NEMS is represented by one position parameter x. The equation can be written as

$$\frac{d^2x}{dt^2}+\eta\frac{dx}{dt}+\frac{kx}{M}=\frac{F_{ext}}{M} \tag{1.1}$$

Where M is the effective mass, η is damping, k is the spring constant, and F_{ext} is the external excitation force. The resonance frequency of a SHO is given by

$$f_0=\frac{1}{2\pi}\sqrt{\frac{k}{M}} \tag{1.2}$$

If a small amount of mass is attached to the NEMS, the resonance frequency shifts and can be written as

$$f_0' = \frac{1}{2\pi}\sqrt{\frac{k}{M+\Delta M}} = f_0 + \Delta f_0 \approx f_0 - \frac{1}{2} f_0 \frac{\Delta M}{M}$$
$$\Delta M = -\frac{\Delta f_0}{2 f_0} M \tag{1.3}$$

Thus, change of resonance frequency due to added mass is proportional to the added mass. It is also observed that the added mass is proportional to the initial mass of the system. Minute mass of the NEMS indicates a very high sensitivity of the added mass.

Due to damping, energy is lost. Quality (Q) factor is used to quantify energy loss during each cycle and defined by

$$Q = 2\pi \frac{\text{total stored energy}}{\text{energy loss during each cycle}} \tag{1.4}$$

Relationship between Q factor and damping η is $Q = \frac{\omega_0}{\eta}$.

Parameters in SHO model could be measured but are not able to be predicted from NEMS geometries and material properties. Continuous mechanics can predict resonance frequencies given NEMS geometries and material. Olsson et al.[15] have compared continuous mechanics and molecular dynamic simulation results and they agree well with each other. Analytic solutions are available for simple beam structure; finite element analysis is used for other geometries.

When the length is much larger than width and height, the object can be described by beam theories. The Bernoulli-Euler beam theory can be written as[15]

$$EI\frac{\partial^4 w(x,t)}{\partial x^4} + \sigma A\frac{\partial^2 w(x,t)}{\partial x^2} + \mu(x,t)\frac{\partial^2 w(x,t)}{\partial t^2} = f(x,t) \tag{1.5}$$

Where E is Young's modulus, I is momentum of inertia, σ is pre-stress, A is cross section area, $\mu(x,t)$ is mass and w is deflection.

Solution of equation (1.5) can be represented by linear combination of basis functions with each of them satisfy boundary conditions $w(x,t) = \sum w_n(x) z_n(t)$.

If the pre-stress can be ignored, analytical solution of basis function can be written as

$$w_n(x) = A\cosh\frac{\lambda_n x}{L} + B\cos\frac{\lambda_n x}{L} + C\sinh\frac{\lambda_n x}{L} + D\sin\frac{\lambda_n x}{L} \tag{1.6}$$

Where A, B, C, D are constant determined by the boundary condition, L is length of the beam, x is distance along the beam and λ_n is characteristic wave number for different modes.

Time dependent part of equation (1.5) can be written as

$$\mu\frac{\partial^2 z_n(t)}{\partial t^2} + (EI + \sigma A) z_n(t) = f(t) \tag{1.7}$$

If we add damping turn to equation(1.7), it is similar to equation(1.1); justifying suitable of modeling a beam as a damped SHO.

Resonance frequency for unstressed beam is written as

$$f_n = \frac{n^2\pi}{2L^2}\sqrt{\frac{EI}{\rho A}} \tag{1.8}$$

Euler beam theory has been applied to NEMS resonators and agrees with experiment results [16-17].

When pre-stress can't be ignored, resonance frequency of stressed beam can be written as

$$f_n = \frac{n^2\pi}{2L^2}\sqrt{\frac{EI}{\rho A}}\sqrt{1 + \frac{\sigma L^2}{n^2 EI\pi^2}} \tag{1.9}$$

Compared with unstressed beam, stressed beam showed better performance with much higher quality factor[18]. It has been proposed that increased Q factor is due to increased stored energy but not a decrease in damping[19]. Highly stressed silicon nitride (SiN) was used in those experiments, and the pre-stress was determined by manufacturing process. Kozinsky et al.[20] demonstrated tuning of the resonance frequency by dynamically changing stress using a side gate. They found an increase of stress with increasing gate voltage and hence the stored energy. While stress introduced during fabrication or gate tuned is static, increasing oscillation amplitude leads to increase of axis stress in the beam. This stress has to be taken into account and equation (1.5) has to be modified as[21]

$$EI\frac{\partial^4 w(x,t)}{\partial x^4}+\left[\sigma A+\frac{EA}{2L}\int_0^L\left\{\frac{\partial w(x,t)}{\partial x}\right\}^2 dx\right]\frac{\partial^2 w(x,t)}{\partial x^2}+\mu(x,t)\frac{\partial^2 w(x,t)}{\partial t^2}=f(x,t) \quad (1.10)$$

Using separation of variables method, $w(x,t)=\sum w_n(x)z_n(t)$, the first vibration mode shape of time dependent function can be written as[21]

$$\begin{aligned}
&[\alpha+\beta\sigma A]z(t)+\gamma z(t)^3+\eta\frac{d^2z(t)}{dt^2}=f(t)\\
&\alpha=\frac{16EI\pi^4}{3L^3}\\
&\beta=\frac{4\pi^2}{3L}\\
&\gamma=\frac{8\pi^4EA}{9L^3}\\
&\eta=\sqrt{\frac{2}{3}}\rho AL
\end{aligned} \quad (1.11)$$

Compared with linear equation(1.5), equation (1.11) is a nonlinear Duffing type equation.

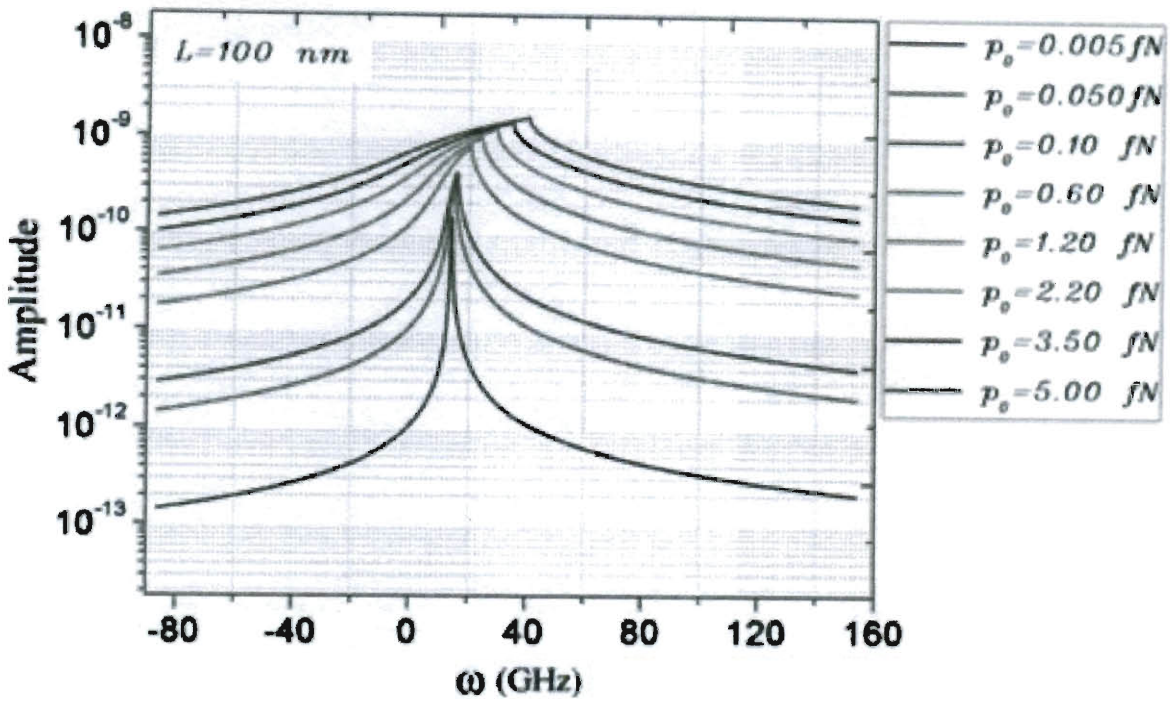

Figure 1-1 Resonance curve of 100nm length CNT, increase of excitation force p_0 leads to Duffing nonlinearity[21]

Onset of this nonlinearity from (1.5) to (1.11) is given by a critical amplitude[22]. A typical Duffing nonlinearity response of CNT is shown in Figure 1-1[21]. Resonance peak shifts upward as the actuation forces increases. Dai et al.[21] discussed the mass detection with nonlinear NEMS oscillators and found a contrast trend of resonance frequency with added mass compared with linear model.

Most of the NEMS oscillators operate at the fundamental resonance mode. Higher operation modes have been considered by several researchers [23-24]. There are several advantages by operating NEMS in higher resonance mode such as location and mass sensitivity[23], less fluid damping[25] etc. Mechanism of mass sensor based on equation (1.3) for first mode oscillation assumes uniform attachment of mass on beam structure. However, it is desired to

measure point mass attachment that can locate at any position on the cantilever. It has been found that point mass sensitivity depends on the location of the added mass for first mode oscillators[26-28]. Dohn et al.[23, 29] considered more than one modes and concluded detection of both mass and location by monitoring resonance frequencies shifts of more than one modes. Another advantage of higher modes is their less susceptible to viscous damping[25] as discussed in more detail in page 20 and section 2.3.

In spite of advantages for higher oscillation modes, there are other problems need to be considered. Euler beam theory ignores shearing and rotating inertia, which can be ignored for lower mode vibration. When the displacement is sufficiently large or higher resonance mode is considered, Timoshenko theory has to be used to account for shearing and rotating. Dynamic equations governing Timoshenko beam are given as[15]

$$\begin{aligned}(\sigma A + k_s GA)\frac{d^2 w}{dx^2} - k_s GA\frac{d\psi}{dx} + \omega^2 \rho A w = 0 \\ I(\sigma + E)\frac{d^2 \psi}{dx^2} + k_s GA\left(\frac{dw}{dx} - \psi\right) + \omega^2 \rho A r^2 \psi = 0\end{aligned} \tag{1.12}$$

Where ψ is rotation of cross section, k_s is cross sectional reduction factor, G is shear modulus, and r is radius of gyration. Olsson et al.[15] compared results of Molecular dynamic simulation, Euler beam theory and Timoshenko beam theory. They found soften of Timoshenko beam compared with Euler beam; and the Timoshenko theory agrees well with MD results. Discrepancy of the results from Euler theory and Timoshenko theory become more significant when higher oscillation modes are considered.

1.2.2 Actuation techniques

Electrical energy transportation is determined by its electromagnetic field. Transferring electrical energy into mechanical energy involves magnetic and electrical forces. Two common techniques, magnetomotive and electrical actuation have successfully actuated NEMS devices based on wide ranges of materials.

Magnetomotive actuation

In magnetomotive actuation technique [16, 20, 30], Lorentz force brings the NEMS device into action. As shown in Figure 1-2, when an AC current flow in the conducting nanostructure in a strong magnetic field, Lorentz force is applied on the nanostructure. Depending on the direction of the magnetic field, the NEMS moves in-plane or out-plane. Lorentz force for a double clamped beam with length l is given by $F = IlB$ (I current, l beam length, B magnetic field). In order to vibrate nanostructure to amplitude large enough to be detectable in magnetomotive actuation schematics, strong magnetic field is generated from superconductor coil, which limit application of magnetomotive actuation. Another drawback is that the resistance of the beam should not be large ($< k\Omega$, $M\Omega$) since large resistance limits driving current due to characteristic mismatch between nanostructure and external excitation source (characteristic resistances of most coaxial cables are 50Ω). Metal film was coated onto nonconductive material providing electrical conductance [10, 31], and may change nanodevices' mechanical properties and increase dissipation[32] at the same time.

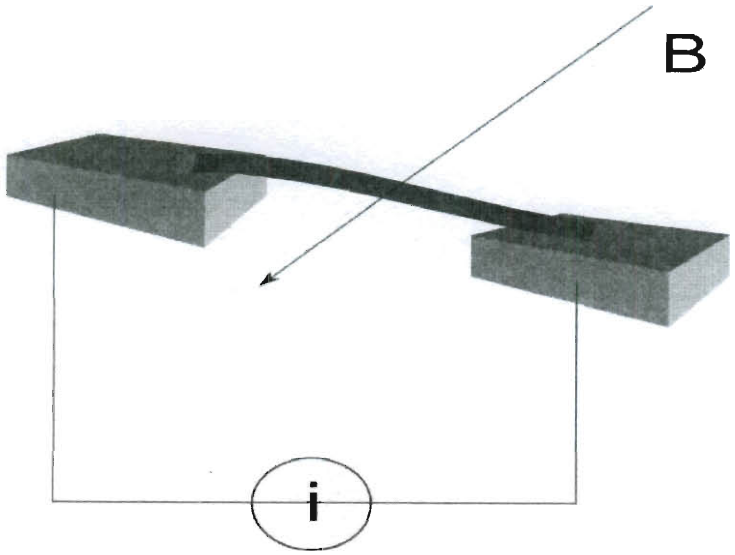

Figure 1-2, magnetomotive actuation, AC current passes through a double clamped nanostructure inside a static magnetic field.

Electrical actuation

Electrical actuation relies on electrostatic force between two electrodes of a capacitor. In electrical actuation, an AC voltage is applied between nanostructure and a counter electrode; and by charging/discharging the capacitor, force is generated on the nanostructure. The force can be calculated as $F = -\frac{\partial U}{\partial d} = -\frac{\partial}{\partial d}\left(1/2Cu^2\right)$, C is the capacitance, d is the distance; and u is voltage. A common schematic configuration used to actuate from semiconductor to metal nanowires [33-35] is shown in Figure 1-3.

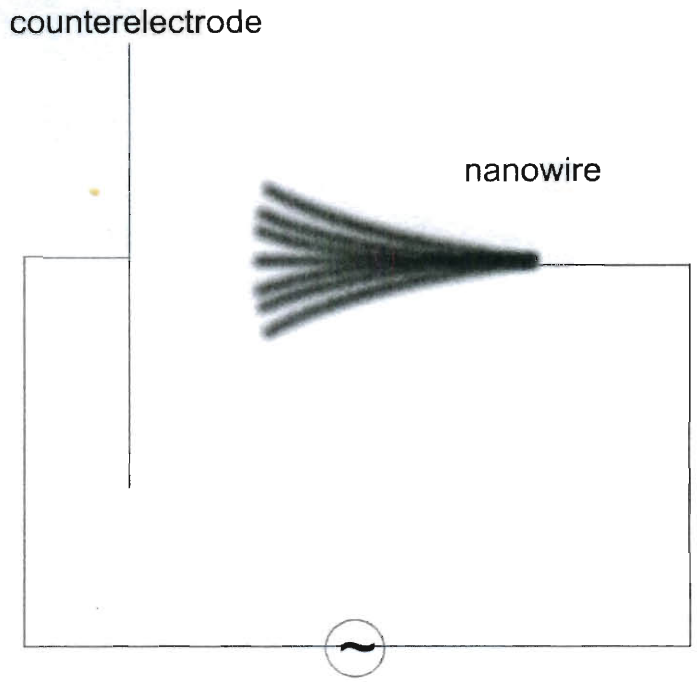

Figure 1-3, electrical actuated nanowire

Electrical actuation technique is not restricted by the conductance, however, parasitic capacitors orders of magnitude larger than nanodevices' capacitor may limit maximum actuation frequency[36] and detecting becomes problematic.

Piezoelectric actuation

In this setup, the NEMS device is placed on a mechanically vibrating piezoelectric disk; the NEMS is thus driven to the frequency of the piezo disk [13]. Piezo actuation is simple to realize and able to deliver enough force to actuate NEMS devices in highly damped liquid environment[37]. Actuation frequency is restricted by piezo crystal's frequency and commercial piezo disks have resonance frequency in the KHz to lower MHz range; which are

much lower than resonance frequencies of NEMS devices (MHz~GHz). Another drawback is that the piezo requires driving voltage in the range of volts; which introduces noise in the NEMS device through parasitic capacitors and inductors. Recent progress in integrating piezoelectric materials into the NEMS shows promising sign of resolving problems mentioned above [14, 38-39]. Integrated piezoelectric NEMS usually contains three layers: the top and bottom conductance layer, and the middle piezoelectric active layer. When a voltage is applied on the top and bottom layers, electric field causes mechanical deformation of the piezoelectric layer.

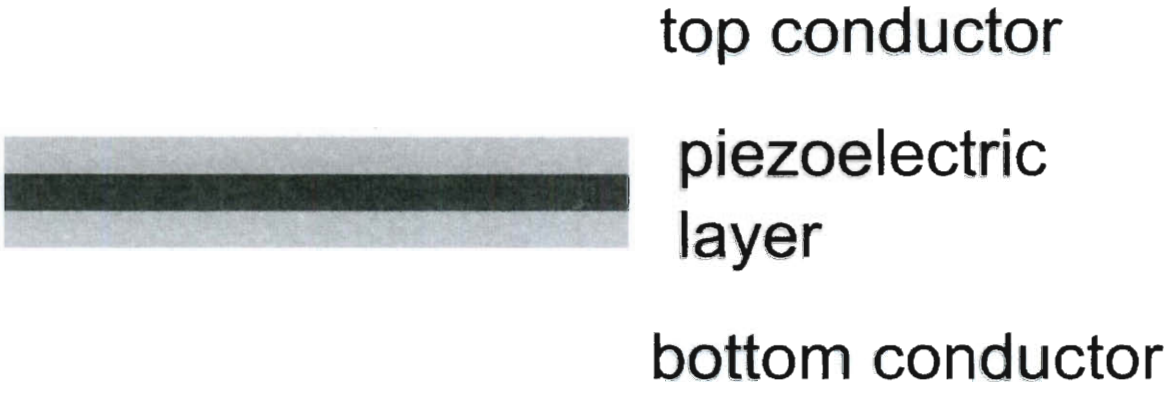

Figure 1-4, structure of integrated piezoelectric NEMS

1.2.3 Self oscillation

Actuation techniques discussed in 1.2.2 treat NEMS as passive device. NEMS are forced to oscillate by external driving force either electric force or magnetic force etc. Practical implementation of NEMS sensors required shrinking down of the system, forced oscillation is difficult to miniaturize due to the size of actuation equipments and the performance of NEMS is restricted by the driving source. Self sustained oscillation of NEMS integrated with CMOS which is driven using easily implemented DC source would be desirable.

Positive feedback is introduced to form a close loop and when the self oscillation condition is satisfied, NEMS starts to oscillate. The positive feedback can be deliberately introduced to the NEMS system with external electronic devices. Feng et al.[56] added finely tuned circuit to a magnetomotive actuated NEMS devices and achieved self-sustained oscillation. This technique is not restricted to magnetomotive actuation but any type of actuation techniques. The difficulty of this technique is the fine tuning of external circuits to nullify parasitic noise. Yet another self actuation method is only possible with electrical actuation. This technique combines mechanical oscillators and field emission. Weldon et al.[57] observed self oscillation of nanotube when a DC voltage applied across the nanotube and the counter electrode exceeded a threshold voltage. The vibration originated from competition of nanotube's bending stiffness and electrostatic force. While field emission current depleted charge on nanotube, electrostatic force weakens and nanotube bounce away from counter electrode due to bending stiffness; charges are built up again when field emission current is low and electrostatic force starts to dominate. Lazarus et al.[58] modeled the system as a LC oscillator and field effect transistor and found the threshold voltage of self oscillation. Compared with external circuit feedback, field emission self oscillation is simpler to implement. However, it is also restricted to field emission effect which requires vacuum and constrains its future applications.

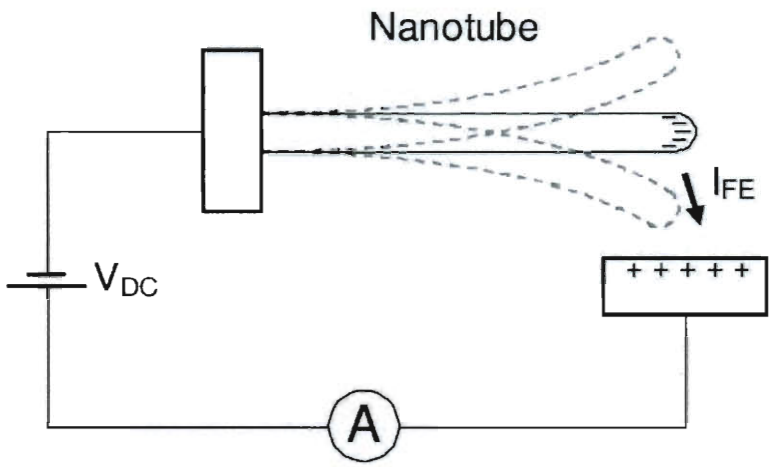

Figure 1-5, self oscillation model of carbon nanotube due to field emission[57]

1.2.4 Sensing principals

Detecting tiny movement in NEMS system requiring supreme sensitivity is challenging. Difficulties come from requirement of supreme sensitivity due to tiny motion; and ultra fast response time due to high resonance frequencies. Methods been developed till today include magnetomotive, optical, capacitive etc.

Magnetomotive sensing

This technique is associated with the magnetomotive actuation technique (page 8). Motion of the NEMS in a static magnetic field generates time varying potential and this potential can be written as $v = \frac{d\varphi}{dt} = \xi Bl\frac{dx}{dt}$, ξ is a factor taking into account of the geometry of double clamped beam, B is magnetic field, l is the length of the beam, and x is center point displacement. Displacement of the middle point can be modeled as Simple Harmonic Oscillator (SHO) if oscillation amplitude is low. Equation of the system can be written as

$$m\frac{d^2x}{dt^2} + \xi m\frac{dx}{dt} + kx = lBI \qquad (1.13)$$

This equation is comparable to RLC oscillation circuit and thus the NEMS resonator is modeled as parallel RLC [40-41]. Detecting NEMS motion is thus simply viewed as detecting characteristic impedance of the RLC network using a network analyzer [16, 30, 42]. Characteristic impedance of RLC network can be either measured by measuring transmitted signal[42]; or reflected signal[30]. Due to small change of characteristic resistance, resistive bridge technique was used to achieve higher resolution [40, 43].

Piezoresistive

Piezoresistive sensing relies on the fact that resistance changes when external strain is applied. Ratio of relative change of resistance with respect to strain is defined as strain gauge factor.

$$GF = \frac{\Delta R / R}{\varepsilon} \tag{1.14}$$

While NEMS is in motion, strain causes resistance change at the same frequency as the mechanical motion. This small change of resistance, similar to magnetomotive method, could be potentially measured using a resistive bridge method[44]. In NEMS, parasitic capacities and resistance forms low pass filter and significantly damped this high frequency signal. Bargatin et al[45] developed heterodyne mixing method to use a lower frequency signal to carry piezoresistive signal. Instead of using DC voltage, an AC voltage at $\omega_d + \Delta\omega$ is applied on the bridge; and the driving signal to the NEMS is chosen to be ω_d. The output voltage is proportional to relative change of resistance and oscillates at frequency of $\Delta\omega$, which can be measured using a lock-in amplifier. Chose of materials for piezoresistive transducer ranges from metals[46] to doped semiconductors[47-48]. Benefit of using

piezoresistive measurement is its high integration with NEMS and can be fabricated as a lab on the chip.

Optical method

In optical interference method, a laser with a spot size of few microns was focused on to the NEMS device[49]. Two commonly used interferometries are path-stabilized Michelson interferometry and Fabry-Perot interferometry. Difference between these two techniques are demonstrated in Figure 1-6[50]. In Michelson interferometry, light reflected from suspended NEMS interferes with light reflected from reference mirror (RM). In Fabry-Perot interferometry, interference happens between reflected light from suspended NEMS and reflected light from substrate. Intensity of interference light is measured with photo detector.

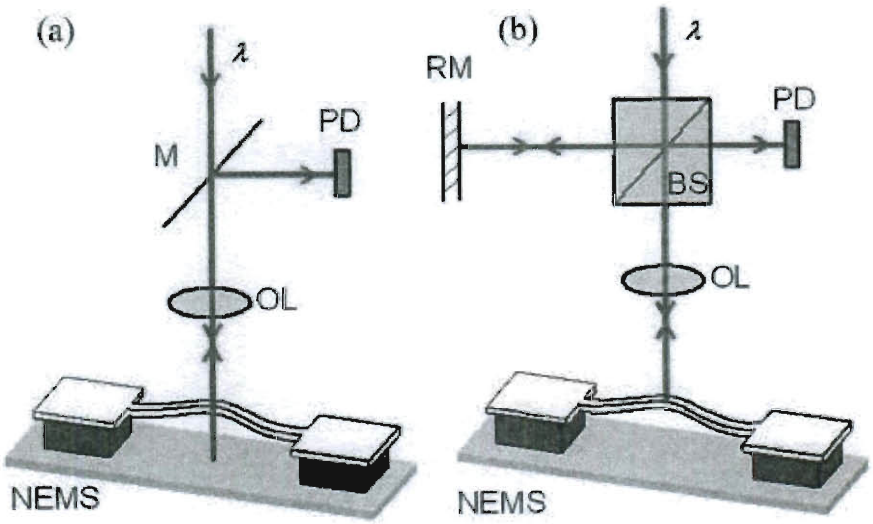

Figure 1-6, Michelson interferometry (a) and Fabry-Perot interferometry setup (b) for detecting displacement of NEMS [50].

Fast optical method is able to profile real time displacement of vibrating NEMS devices and capture the damping [5, 51]. Another advantage of optical method is that it also able to

detect signals reflected from liquid[37]. However, while the width of device is comparable to wavelength of the light, diffraction limits application of optical method[52]. A recent noninterferometric method uses Mie scattering analysis[53] has demonstrated new approach for high resolution detection.

Direct imaging

Direct imaging is straight forward. Resonance of NEMS is observed in a SEM or TEM [34-35]. AFM is also been used to capture the resonance envelope of resonating NEMS though the resonance frequency of a NEMS is much higher than response time of AFM control circuit [54]. Using amplitude modulation, Sanchez et al.[55] were able to detect mechanical vibrations of suspended graphene sheets. The advantage of using AFM technique is its high lateral resolution. Compared with other techniques that are only able to obtain one average displacement signal, AFM is able to probe local deformations[55].

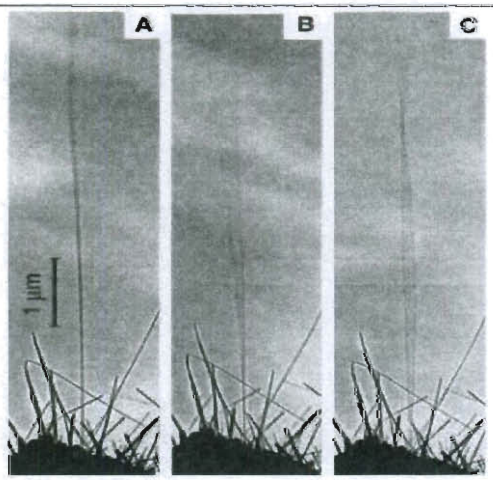

Figure 1-7, carbon nanotube resonates in TEM[35]

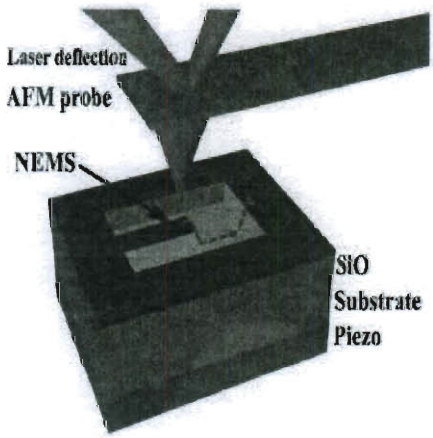

Figure 1-8, AFM measures NEMS resonance[54]

1.2.5 Damping in NEMS

Stored energy in NEMS resonators dissipates energy through interactions with their environment. Quality factor is used to qualify energy dissipation in NEMS system and is defined by the ratio of total stored energy to the energy loss during each resonating cycle. The inert mass sensitivities of NEMS system depend on the quality factors of the system given by[59] $\delta M \sim \left(\Delta f \frac{1}{Q\omega_0} \right)^{1/2}$; δM is mass sensitivity, Δf is measurement bandwidth, ω_0 is free resonance frequency, and Q is the quality factor. To increase mass sensitivity, higher quality factor is desired. Energy is lost through various channels and can be categorized as the intrinsic loss and extrinsic loss. System's total Q factor is given by

$$\frac{1}{Q_{\text{total}}} = \sum \frac{1}{Q_{\text{intrinsic}}} + \sum \frac{1}{Q_{\text{extrinsic}}} \tag{1.15}$$

Intrinsic loss

The fundamental process of the intrinsic loss is phonon-phonon interaction. Mechanical vibration of the NEMS resonator perturbs phonon distribution of solid[60]. Dissipation mechanism depends on relative magnitudes of three parameters: thermal phonon mean-free path l, thermal phonon wavelength λ, and characteristic NEMS device size L.

Thermoelastic dissipation

When $l \ll L$, perturbed phonons are quickly thermalized and a local temperature can be defined. Thermoelastic dissipation is due to coupling of local strain and local temperature analogous to compressing/inflating process of thermal dynamic gas. Zener [61-62] first studied thermoelastic effect and found Q factor can be written as

$$Q^{-1} = \frac{\alpha_T^2 TE}{C_p} \frac{v_0 v}{v_0^2 + v^2} \tag{1.16}$$

Where T is temperature, E is Young's modulus, C_p is thermal capacity, α_T is thermal expansion coefficient, v_0 is constant.

Lifshitz and Roukes[63] gave exact solution

$$Q^{-1} = \frac{E\alpha^2 T_0}{C}\left(\frac{6}{\xi^2} - \frac{6}{\xi^3}\frac{\sinh\xi + \sin\xi}{\cosh\xi + \cos\xi}\right) \tag{1.17}$$

ξ is a variable defined as $\xi = b\sqrt{\frac{\omega_0}{2\chi}}$, χ is thermal diffusivity.

Thermoelastic dissipation indicates linear increase in dissipation with shrinking system. The relationship between Q factor and temperature has been exploited to the fabrication of temperature sensor by monitoring the Q factor change[64].

Akhieser effect

When $l \gg L$, disturbed phonon distribution acquires equilibrium through local phonon-phonon interaction. Akhieser effect was first studied by Akhieser and further developed by Woodruff and Ehrenreich[65]. Woodruff et.al [65] gave attenuation Γ ,and the Q factor can be deduced from Γ.

$$\Gamma = \frac{C_v \gamma^2 \Omega^2 T\tau}{3\rho c^3}$$
$$Q = \frac{\Omega}{c\Gamma} = \frac{\rho c^2}{\gamma^2 c_v T\Omega} \tag{1.18}$$

Where ρ is density, c is sound speed, γ is Grüneisen parameter, T is temperature, and Ω is wave number of vibration.

Extrinsic loss

Extrinsic loss is loss due to interaction with environment such as support of nanomaterials, surface structure etc.

Support loss

The support loss, or clamp loss, is the transfer of energy from the beam to supporting clamp. Elastic waves are excited at the clamping boundary due to shear stress at the clamping. Assuming same thin thickness at the clamping side and beam, Zhili et.al[66] derived close form of clamping loss for clamped-free and clamped-clamped beams. The resultant Q factor due to support loss scales with geometry and vibration mode order as

$$Q_{clamp} \sim \left(\frac{L}{b}\right)^3 \frac{1}{(\beta_n \chi_n)^2} \tag{1.19}$$

Where L is length of the beam, b is width of the beam, and β_n ,χ_n are mode parameters.

Photiadis et al. [67] considered different substrate thickness than beam thickness and deduced Q factors for thin (1.20) and thick (1.21) supporting medium

$$Q^{-1} \approx 0.95 \frac{w}{l} \frac{h^2}{h_b^2} \tag{1.20}$$

$$Q^{-1} \approx 0.31 \frac{w}{l} \left(\frac{h}{l}\right)^4 \tag{1.21}$$

h_b is the thickness of supporting medium in equation (1.20).

Surface loss

Surface loss comes from surface defects or absorbate, which cause modification of local stress. Surface defects originated from several sources including plasma damage[68], ion implantation, absorbates from air[69]. Surface energy loss can be modeled using a complex number Young's modulus $E = E_1 + iE_2$ and a surface layer thickness δ, and the Q factor due to surface loss can be written as [70]

$$Q_{surface} = \frac{wt}{2\delta(3w+t)} \frac{E_1}{E_2^s} \tag{1.22}$$

E_2^s is the imaginary part of surface Young's modulus, w is beam width, and t is beam thickness.

Surface losses can be reduced using annealing[69], oxidation[68] and surface termination[71].

Fluid loss

For NEMS oscillator working in low vacuum or higher pressure, energy is transferred from oscillating beam to fluid. Fluid loss is the dominant loss in high pressure and liquid. Due to their low scale, continuous fluid theory may not work for NEMS resonators. Depending on NMES size and gas pressure, fluid effects are described by continuous or noncontinuous flow. Knudsen number (Kn), defined as the ratio of mean free path over characteristic device size, is the parameter used to separate flow regions. For Kn>10, free molecular flow is accurate; for Kn<0.01, continuous Navier Stokes theory can be applied; and in the intermediate Kn, transition flow happens[72]. For NEMS resonators with dimension of nanometers in gas, free molecular flow can span a large range to atmosphere pressure. Continuous model is

accurate in liquid. Joseph et.al [73] calculated free molecular collision induced energy loss and gave Q factor as

$$Q_{collison} = \frac{t\rho_s \omega}{c\rho}\sqrt{\frac{M}{RT}} \tag{1.23}$$

Where t is beam thickness, ρ_s and ρ are densities of solid and fluid respectively, M and R are molecular weight and gas constant, and c is a constant.

Martin et.al[74] considered damping of carbon nanotube in the same free molecular region and was able to fit experimental data.

When gas pressure increase to transition region, none of above theories accurately models the system. Yakhot [75] analyzed transition region gas damping and used by Svitelskiy[5] to study NEMS damping behavior from free molecular to continuous flow.

In the continuous flow region, Sader et.al [24-25, 76-79] gave analytic solutions for rectangular beam oscillating in liquid.

1.3 Thesis outline

This document has four more chapters. In chapter two, the sensitivity of NEMS resonators considering nonlinear fitting uncertainties was analyzed followed by calculations of amplitudes response with added mass for NEMS resonators in liquid. At the end of chapter two, preliminary results of magnetomotively actuated suspended gold NEMS device were shown. In the third chapter, electromechanical properties of suspended gold nanowire were studied. Traditional Fuchs theory was used to describe the size effect of electromechanical properties of gold nanowires.

In chapter four, the mechanical properties of few layer boron nitride films were measured and their potential for future NEMS devices in conjunction with graphene was briefly discussed. Conclusion and future work were discussed in the final chapter.

Chapter 2 Sensitivity limit of NEMS mass sensors

2.1 Introduction

In this chapter, theoretical analysis of resonator based inertial mass sensors was discussed. It contains three parts. In the first part, the NEMS resonator was modeled by a simple harmonic oscillator (SHO). Nonlinear fitting technique used to fit data to theory was discussed and its implication to sensitivity limit was analyzed. In second part, NEMS was described using Euler Beam theory and transfer functions of the beam under different liquids are calculated. Effects of added point mass to the shift of resonance frequency and change of quality factor were examined. In the final part, magnetomotive actuation results of suspended gold nanowire NEMS devices in liquid were shown.

2.2 Sensitivity analysis using nonlinear fitting technique

2.2.1 Introduction

Nanoelectromechanical resonators, due to their high resonance frequency and high quality factor (Q), have being actively studied for their potential as ultrahigh sensitivity, low power consumption mass sensors. Methods used to actuate and detect NEMS resonators motion include magnetomotive force [30], mixing[80], electromechanical actuation[35] and optical interference[51]. NEMS devices can be either continuously excited using sweeping frequency excitation (frequency domain measurement) or unit pulse excitation (time domain measurement). Similar to crystal mass sensor, detection of

resonance frequency shift of NEMS resonators has been used to detect masses [2, 81]. Steady progresses have been reported about their sensitivities. The increase of sensitivity, however, will finally reach a limit. Ekinci et.al[59] analyzed the fundamental limits to the sensitivities based on phase lock loop (PLL) locking technique and pointed out that higher resonance frequency and higher Q factor will lead to better resolution . Frequency shift method relies on accurate detection of resonance peak. If no PLL is used, function fitting was used to find resonance frequency (ω_0) and quality factor (Q)[81-82]. For sweeping excitation, Lorentz function is used; while for pulse excitation, damped Simple Harmonic Oscillator (SHO) function is used. Uncertainties of fitting parameters (resonance frequency and quality factor) will be affected by data noise. Here, "statistical noise" is defined as the uncertainty associated with fitting parameters. In this section, I will analyze the statistical noises for a variety of ω_0 and Q combinations.

2.2.2 Nonlinear fitting errors

NEMS resonators can take many architectural forms; they can be double clamped beam, single clamped beam or tuning forks[83]. For simplicity, only clamped beam structure and fundamental resonance mode was considered. On such condition, the damped beam equation can be simplified to a damped simple oscillator (SHO). The equation is given by

$$\frac{d^2x}{dt^2} + 2\xi\omega_0 \frac{dx}{dt} + \omega_0^2 x = \frac{F}{m^*} \tag{2.1}$$

ξ is the damping parameter ($\xi = \frac{1}{2Q}$), ω_0 is the resonance frequency without damping, and $\boldsymbol{m}^*$ is the effective mass of the beam.

In pulse excitation mode, after a pulse excitation, beam deflection is measured in time domain of the free damping. The excitation external force is given by

$$\boldsymbol{F} = \begin{cases} \boldsymbol{F}_0, & \boldsymbol{t} < 0 \\ 0, & \boldsymbol{t} > 0 \end{cases} \tag{2.2}$$

The displacement of the beam at free end can be written as

$$x(t) = A_0 e^{-\xi\omega_0 t} \sin(\sqrt{1-\xi^2}\,\omega_0 t + \varphi) \tag{2.3}$$

And A_0 is deflection at time zero.

In continuous sweeping configuration, periodic external excitations with sweeping frequencies are applied on the beam and response amplitudes are measured.

Relationship between response amplitude and excitation frequency is given by Lorentz function

$$A(\omega) = \frac{A_0}{\sqrt{(\omega^2/\omega_0^2 - 1)^2 + (2\xi\omega/\omega_0)^2}} \tag{2.4}$$

A_0 is response amplitude at zero frequency.

Fundamental resonance frequency and damping parameter could be determined by nonlinear fitting using equation (2.3) in pulse mode or equation (2.4) in sweeping mode. The standard deviations of fitted ω_0 and ξ depend on root mean square of measured data and fitting equations. The covariance matrix of fitting parameters are given by [84]

$$\boldsymbol{Cov}(\omega_0, \xi) = (\boldsymbol{J}(\omega_0, \xi)^T \boldsymbol{J}(\omega_0, \xi))^{-1} \tag{2.5}$$

While Jacobian $\boldsymbol{J}(\omega_0,\xi)$ is given by

$$\boldsymbol{J}(\omega_0,\xi)=\begin{pmatrix} \frac{1}{\sigma_1}\frac{\partial \boldsymbol{f}_1}{\partial \omega_0} & \frac{1}{\sigma_1}\frac{\partial \boldsymbol{f}_1}{\partial \xi} \\ \cdots\cdots & \\ \frac{1}{\sigma_m}\frac{\partial \boldsymbol{f}_m}{\partial \omega_0} & \frac{1}{\sigma_m}\frac{\partial \boldsymbol{f}_m}{\partial \xi} \end{pmatrix} \tag{2.6}$$

$\boldsymbol{f}$ is the fitting equation given by (2.3) or (2.4), and $\frac{\partial \boldsymbol{f}_i}{\partial \square}$ is the derivative evaluated at data point $\boldsymbol{i}$ ($\boldsymbol{i}=1,2,3...\boldsymbol{m}$).

Equation (2.5) can be explicitly written as

$$\boldsymbol{Cov}(\omega_0,\xi)=\frac{1}{\left(\sum\left(\frac{1}{\sigma_i}\frac{\partial \boldsymbol{f}_i}{\partial \xi}\right)^2\right)\left(\sum\left(\frac{1}{\sigma_i}\frac{\partial \boldsymbol{f}_i}{\partial \omega_0}\right)^2\right)-\left(\sum\frac{1}{\sigma_i^2}\frac{\partial \boldsymbol{f}_i}{\partial \xi}\frac{\partial \boldsymbol{f}_i}{\partial \omega_0}\right)^2}\begin{pmatrix} \sum\left(\frac{1}{\sigma_i}\frac{\partial \boldsymbol{f}_i}{\partial \xi}\right)^2 & -\sum\frac{1}{\sigma_i^2}\frac{\partial \boldsymbol{f}_i}{\partial \xi}\frac{\partial \boldsymbol{f}_i}{\partial \omega_0} \\ -\sum\frac{1}{\sigma_i^2}\frac{\partial \boldsymbol{f}_i}{\partial \xi}\frac{\partial \boldsymbol{f}_i}{\partial \omega_0} & \sum\left(\frac{1}{\sigma_i}\frac{\partial \boldsymbol{f}_i}{\partial \omega_0}\right)^2 \end{pmatrix} \tag{2.7}$$

Covariance matrix $\boldsymbol{Cov}(\omega_0,\xi)$ is a function of the model parameters (ω_0,ξ) and auxiliary parameter (in pulse mode, it is time $\boldsymbol{t}$ when position of resonator is measured; in sweeping mode, it is excitation frequency ω). Discrete equation (2.7) can be simplified to continuous equation if sample data points are dense. In sweeping mode, element at fist row and first column in (2.7) can be written as

$$\sum\left(\frac{1}{\sigma_i}\frac{\partial \boldsymbol{f}_i}{\partial \xi}\right)^2=\frac{1}{\Delta\omega}\sum\left(\frac{1}{\sigma_i}\frac{\partial \boldsymbol{f}_i}{\partial \xi}\right)^2\Delta\omega\approx\frac{1}{\Delta\omega}\int\left(\frac{1}{\sigma}\frac{\partial \boldsymbol{f}}{\partial \xi}\right)^2\boldsymbol{d}\omega \tag{2.8}$$

Applying similar transformation to other terms in (2.7)

$$Cov(\omega_0,\xi)=\frac{\Delta x}{\int\left(\frac{1}{\sigma}\frac{\partial f}{\partial \xi}\right)^2 dx\int\left(\frac{1}{\sigma}\frac{\partial f}{\partial \omega_0}\right)^2 dx-\left(\int\left(\frac{1}{\sigma^2}\frac{\partial f}{\partial \xi}\frac{\partial f}{\partial \omega_0}\right)dx\right)^2}\begin{pmatrix}\int\left(\frac{1}{\sigma}\frac{\partial f}{\partial \xi}\right)^2 dx & -\int\frac{1}{\sigma^2}\frac{\partial f}{\partial \xi}\frac{\partial f}{\partial \omega_0}dx\\ -\int\frac{1}{\sigma^2}\frac{\partial f}{\partial \xi}\frac{\partial f}{\partial \omega_0}dx & \int\left(\frac{1}{\sigma}\frac{\partial f}{\partial \omega_0}\right)^2 dx\end{pmatrix} \tag{2.9}$$

And Δx is the spacing between adjacent data points (time in pulse mode and frequency in sweeping mode). Furthermore, once we know analytical expression of the fitting function f , $Cov(\omega_0,\xi)$ does not depend on values of measurement data points but depends on their deviation σ. It will be shown that, with given auxiliary parameter, model parameters' variances behave differently in pulse mode and sweeping mode measurement.

2.2.3 Numerical calculations

Covariance matrix can be evaluated numerically using equation (2.7) or analytically using equation(2.9). The results are the same using both methods. Analytic expressions of covariance matrix elements given by (2.9) are shown in the appendix. To numerically evaluate trends of model parameters' variances with respect to model parameters, a range of (ω_0,ξ) pairs are selected with fixed auxiliary parameter. All parameters are listed in Table 2-1. It is assumed normalized root mean squares of measurement data were constant independent of frequency and time.

ξ	ω_0 (MHz)	Frequency domain range (MHz)	Time domain range (μsec)
0.01:0.01:0.5	50:1000	0:0.5:2000	0:0.0005:2

Table 2-1, Range of parameters. Two ranges of damping parameter, one represents low damping, and another represents large damping were selected. Units of frequencies and times could be scaled up or down simultaneously without affecting results.

Normalized Root Mean Squares (RMSs) of damping parameter and resonance frequency measured in pulse mode and sweeping mode were shown in Figure 2-1 and Figure 2-2. Results were shown in unit of normalized measurement RMS σ. RMSs in pulse mode and sweeping mode measurements have contrasting trend. In pulse mode, larger RMS results from high resonance frequency and larger damping. In sweeping mode, on the other hand, larger RMS happens in low resonance frequency and high damping region. This indicated that in region of high damping such as liquid, time domain measurement of a NEMS resonator with high resonance frequency would be more accurate than measurement in frequency domain in terms of standard deviation. This is supported by experiment results[85].

Furthermore, with low Q factor (Q<1/2), the SHO system is over damped and the system may not be able to be actuated using sweeping mode. In this situation, pulse mode excitation and measurement will be able to track the exponential decay of the SHO.

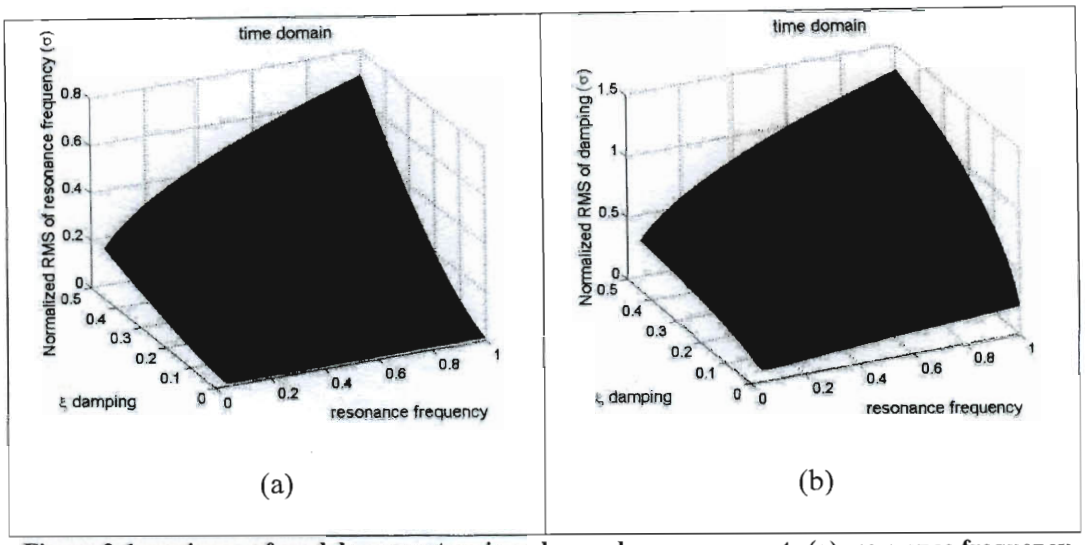

Figure 2-1, variance of model parameters in pulse mode measurements (a) resonance frequency, (b) damping

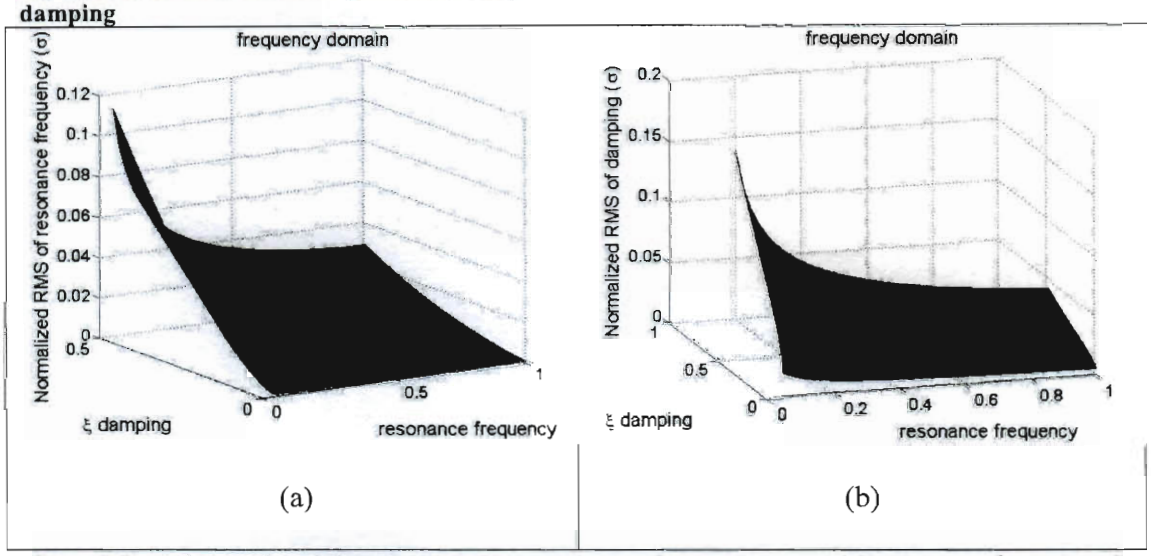

Figure 2-2, variance of model parameters in sweeping mode measurement (a) resonance frequency (b) damping;

RMS uncertainty of fitted resonance frequency determines mass resolution. Frequency shift with respect to mass change is given by

$$\frac{\delta m}{m} = -\frac{2\delta f}{f_0} \tag{2.10}$$

Ekinci[59] deduced that $\delta M \sim (1/Q\omega_0)^{1/2}$. Analytic expressions given in Appendix can be approximated using simple function form $a\xi^b f_0^c$ to fit normalized RMSs in frequency domain. The approximate functional form is $\delta M \sim 1/\omega_0^{1/2} Q^{3/2}$. Compared with Eknici's result, statistical uncertainty error indicates that mass detection sensitivity has higher order of dependency on the Q factor.

In conclusion, damped NEMS resonators in both time domain and frequency domain were analyzed. The RMSs of fitted resonance frequency and damping factor, which are proportional to mass sensing resolution, were calculated. The trend of RMSs in time domain is in contrast with trend of RMSs in frequency domain. For NEMS system with high resonance frequency and low damping, frequency domain measurement gives better sensing resolution than time domain measurement. For NEMS system with low resonance frequency and high damping, time domain measurement produces better resolution. It has also been found the resolution for measurement in frequency domain is highly dependent on the damping.

2.3 Modeling mass sensitivity in fluid

Large amount of literatures are available discussing operating NEMS resonators in vacuum. In current literature, a vibration NEMS beam was modeled either using simple harmonic oscillator (SHO)[86-88] with effective mass and spring constant considering real geometry or using full Euler beam theory[34, 89-90]. SHO model ignores geometries of NEMS oscillators and thus is not able to predict damping due to interaction with external fluid. It is known that continuous Navier-Stokes equations may not be used

in nanoscale even in atmosphere pressure [72]. In liquid, however, continuous model can still be used[37]. Many papers discuss frequency response of beam structure in fluid [24, 77, 91-92] targeting at AFM cantilevers and other MEMS devices. The influences of fluid to oscillation objects can be categorized into two parts; one is the added mass taking account of fluid particles moving with oscillating solid, another is the friction dissipation due to fluid viscosity. Analytical theory[24, 76-77] and finite element analysis[93] are available in analysis fluid effect on oscillating beam. However, no literature discussed about the attachment of particles to oscillating beams in fluid and the influence of fluid to mass sensitivity for NEMS. In this section, Euler beam theory and continuous fluid model were used to analyze point mass detection sensitivity in fluid.

2.3.1 Model description

We are interested in response of a vibrating beam in liquid before and after a point mass attached to the free vibration end as illustrated in Figure 2-3.

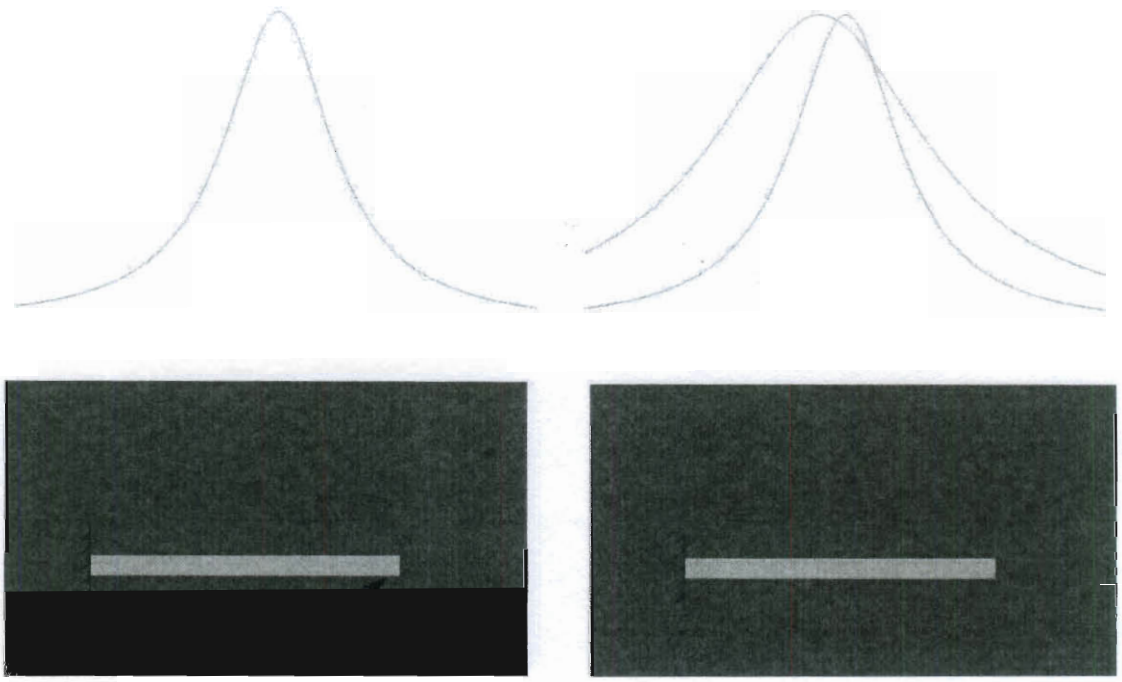

Figure 2-3, Illustration of the model: a one end fixed vibrating beam in liquid, before and after mass attachment. Resonance peak shifts down and broadened.

The model begins with standard Euler beam theory with beam length L, width b and thickness h ($b \ll L$, and $h \ll L$).

$$EI\frac{\partial^4 u(x,t)}{\partial x^4} + \mu\frac{\partial^2 u(x,t)}{\partial t^2} = f(x,t) \tag{2.11}$$

E is Young's modulus, I is moment of inertia, m is unit length mass, and u is beam displacement.

For beam before point mass attachment to the end point, the boundary conditions are:

$$u(0,t) = \partial_x u(0,t) = \partial_x^2 u(L,t) = \partial_x^3 u(L,t) = 0 \tag{2.12}$$

For beam with a point mass of m attached to the end of the beam, the boundary conditions are[94]:

$$u(0,t) = \partial_x u(0,t) = \partial_x^2 u(L,t) = 0$$
$$\partial_x^3 u(L,t) = \frac{m}{EI}\partial_t^2 u(L,t) \tag{2.13}$$

Fourier transfer of equation (2.11) is:

$$EI\frac{\partial^4 U(x,\omega)}{\partial x^4} - \omega^2 \mu U(x,\omega) = F(x,\omega)$$
$$F(x,\omega) = F_{hydro}(x,\omega) + F_{excite}(x,\omega) \tag{2.14}$$
$$F_{hydro}(x,\omega) = \frac{\pi}{4}\rho\omega^2 b^2 \Gamma(\mathrm{Re})U(x,\omega)$$

Using separation of variables, $U(x,\omega)$ can be written as $U(x,\omega) = \sum_{i=1}^{\infty} h_i(\omega)\varphi_i(x)$. $\varphi_i(x)$ are eigen solutions of homogeneous equation

$$EI\frac{\partial^4 \varphi(x)}{\partial x^4} - \omega^2 \mu \varphi(x) = 0 \tag{2.15}$$

The general solution of equation (2.15) can be written as

$$\varphi(x) = A\cosh(kx) + B\sinh(kx) + C\cos(kx) + D\sin(kx) \tag{2.16}$$

With A, B, C, D constant determined by boundary conditions and $k = \frac{\alpha_n}{L}$ (α_n are dimensionless wavelength at n^{th} mode with $\cos(\alpha_n) + 1/\cosh(\alpha_n) = 0$).

Constants in (2.16) for boundary condition (2.12) has been solved[95] and $\varphi_i(x)$ can be written as:

$$\varphi_i(x) = \left\{ [\cosh(\alpha_n x) - \cos(\alpha_n x)] - \frac{\sinh(\alpha_n L) - \sin(\alpha_n L)}{\cos(\alpha_n L) + \cosh(\alpha_n L)} [\sinh(\alpha_n x) - \sin(\alpha_n x)] \right\} \tag{2.17}$$

For boundary condition(2.13), the solution form will be the same as (2.17) but with different α_n (with α_n given by $\cos(\alpha)+1/\cosh(\alpha)+\zeta\alpha(\tanh(\alpha)\cos(\alpha)-\sin(\alpha))=0$, and $\zeta=\frac{m}{M}$, m is the point mass and M is the beam mass[94]).

The resonance frequency in vacuum can be written as

$$\omega_n=\frac{\alpha_n^2}{L^2}\sqrt{\frac{EI}{m}} \tag{2.18}$$

Following Xin et. al.[96], the transfer function can be written as

$$h_i(\omega)=\frac{\int_0^L\varphi_i dx \Big/ \left(\mu\int_0^L\varphi_i^2 dx\right)}{\omega_i^2-\omega^2(1+\frac{\pi}{4\mu}\rho_f b^2\Gamma)} \tag{2.19}$$

In equation (2.19), fluid effect has been taken account by hydrodynamic function Γ given by Sader[24]. Hydrodynamic function Γ is a function of Reynolds number given by

$$\mathrm{Re}=\frac{\rho\omega b^2}{4\eta} \tag{2.20}$$

Then, transfer functions of a beam in fluid with and without point mass attached to the end can be evaluated from equation (2.19) with corresponding α_i and φ_i. Mass ratio from 0.001 to 0.5 and their first five α values are listed in Table 2-2.

ζ	α				
0	1.875	4.694	7.855	10.996	14.137
0.001	1.873	4.689	7.847	10.985	14.123
0.01	1.857	4.650	7.783	10.898	14.015
0.1	1.723	4.400	7.451	10.522	13.614
0.5	1.420	4.111	7.190	10.298	13.421

Table 2-2, values of attached mass to total beam mass ratio and their corresponding α values

The α values for different ζ are plotted in Figure 2-4.

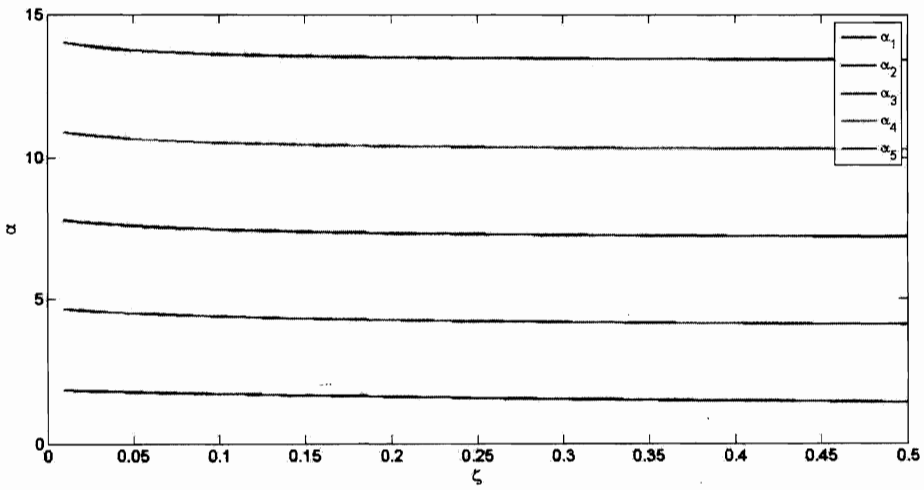

Figure 2-4, first five α values for different ratio of attached masses

2.3.2 Transfer function of NEMS Au NW

Transfer functions for no point mass loading and with point mass loading can be calculated as followed. For a gold beam with geometry listed in Table 2-3, the transfer function can be written as

$$h_i(\omega) = \frac{\int_0^1 \varphi_i dx / \int_0^1 \varphi_i^2 dx}{398.25\alpha_i^4 - \omega^2(19.3 + \frac{\pi}{4}\rho_f \Gamma)} \tag{2.21}$$

The chosen liquids are water and air with density and viscosity listed in Table 2-4.

Gold density g/cm^3	Width (nm)	Height (nm)	Length (um)	Young's modulus (Gpa)[97]
19.3	70	70	3	79

Table 2-3, Parameters for modeling gold nanowire

Water density kg/m^3	Air density kg/m^3	Water dynamic viscosity Ns/m^2	Air dynamic viscosity Ns/m^2
1000	1.18	10^{-3}	1.983×10^{-5}

Table 2-4, Properties of liquids

Figure 2-5 and Figure 2-6 demonstrate the first resonance mode amplitude of transfer functions ($|h_i(\omega)|$) of the gold beam described above in water and air in response to end point load masses. Clearly, resonance peaks in water are broader and smaller than those in air. These effects can be attributed to the fluid viscous damping and added mass effect respectively. With added mass, the effective mass increased due to fluid moving with the beam. For viscous damping effect, beam's energy is lost due to friction with fluid. Curves of response functions, although not the same; are similar to Lorentz function.

Resonance frequency is defined as frequency where amplitude reaches maximum. Q factor is defined as $Q = \omega_0 / \text{FWHM}$, FWHM is the full width half maximum of the curves.

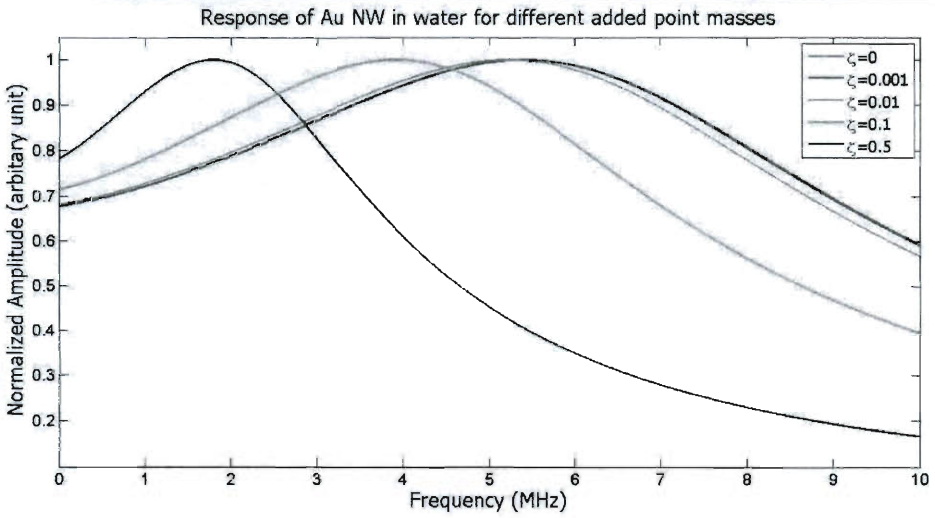

Figure 2-5, First resonance response mode of the beam end with excitation frequency in water for different end point masses

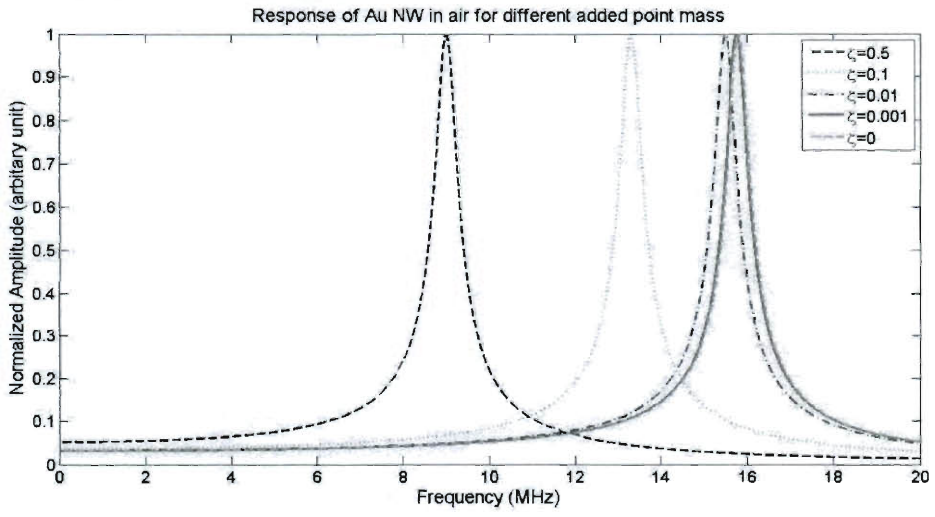

Figure 2-6, First resonance mode response of the beam end with excitation frequency in air for different end point masses

For NEMS inert mass sensors based on peak detection technique, the mass sensitivity can be expressed as $\delta m = 1/\frac{\partial \omega}{\partial m}\delta\omega$, simple harmonic oscillator model predicted[59] that $\frac{\delta m}{m} = -2\frac{\delta\omega_0}{\omega_0}$. The mass sensitivity for full beam theory in water and air is demonstrated in Figure 2-7.

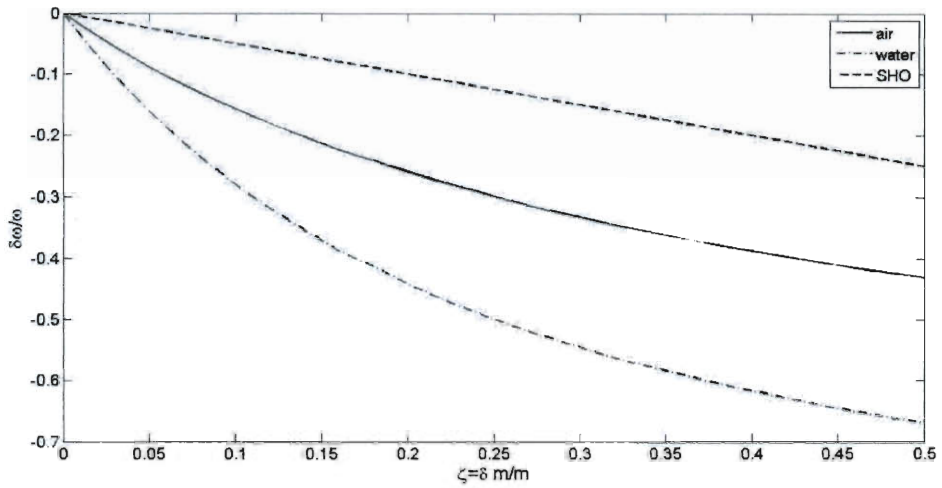

Figure 2-7, relative change of resonance frequency with respect to added mass for NEMS operate in water and air, compared with prediction from simple harmonic oscillator model

The relative change of resonance frequency with respect to added mass predicted by the full beam theory is larger than SHO model. As the added mass increases, the slope approaches the value predicted by SHO; which is expected because as the point mass increases, mass from the beam contribute less and the whole system approaches SHO. The mass response is higher in water with higher density and viscosity than in air. This might be related to the point mass induced model shape change, which affects added mass from fluid. The point mass effect is thus amplified by surround fluid. Another noticeable liquid effect is the decrease of quality factor; lowering quality factor reduces

sensitivity. Ekinci[59] predicted that for high Q factor, the sensitivity be inversely proportional to square root of quality factor $\delta m \propto \sqrt{\frac{1}{Q}}$. This is deduced based on the assumption that added mass won't affect quality factor. In reality, however, added mass will affect the Q factor due to the change of mode shapes, which affect energy dissipation to liquid. Figure 2-10 and Figure 2-11show that increased added point mass causes the decrease of Q factor.

As can be seen in Figure 2-11, in water, Q factors are close to 1/2 for all conditions of added masses. For system with Q factor smaller than 1/2, it is over damped and may not be able to be actuated.

Higher modes transfer function can be calculated with the same procedure as the first mode. Figure 2-8 demonstrates the second mode transfer function of Au NW in water for different added mass.

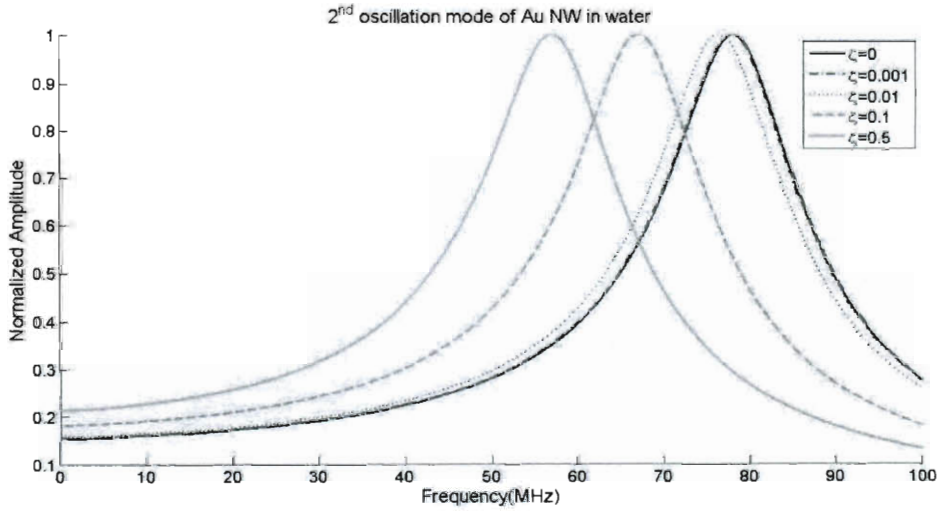

Figure 2-8, Second mode of Au NW in water in response to added point mass

Compared with first mode shown in Figure 2-5, second mode has higher Q factor. In fact, higher modes are less affected by surrounding fluid than lower modes[76]. Sensitivity might be increased by operating NEMS in higher modes. However, there are limitations with higher modes. Amplitude of transfer functions for higher mode is orders of magnitude smaller than its previous lower mode. Figure 2-9 plots transfer function of the first and the second modes together; the second mode peak is buried in the tail of the first mode. Enhanced higher harmonics technique used in MEMS cantilever[98] may be applied to NEMS.

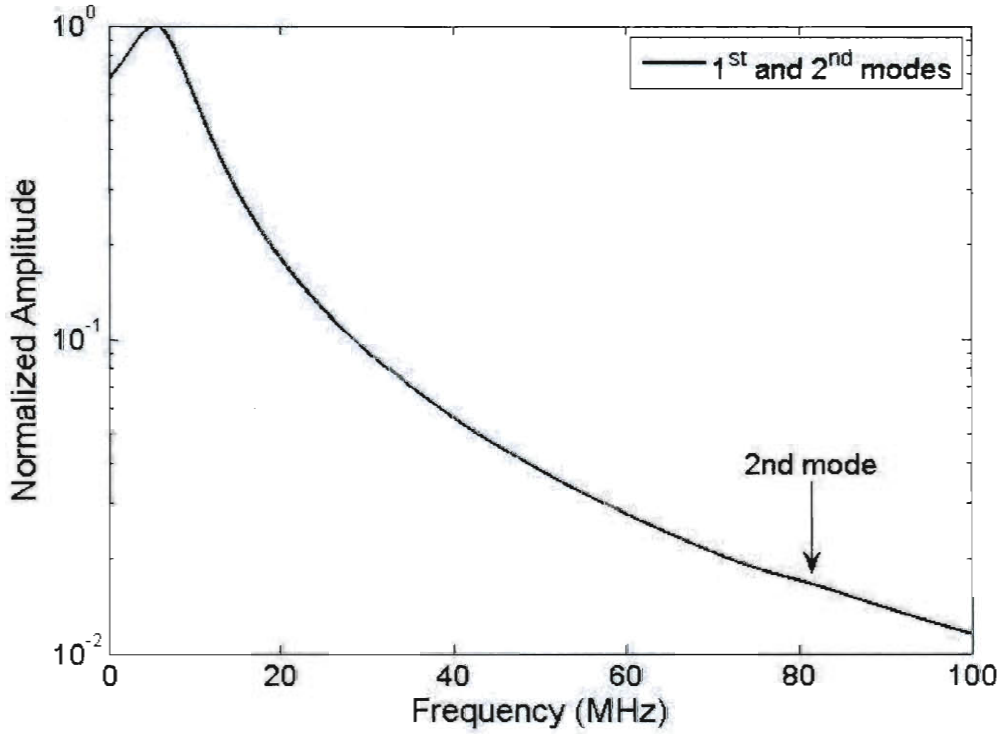

Figure 2-9, Transfer functions of the first and the second modes of Au NW in water with no added mass. The second mode peak is buried in the tail of the first mode

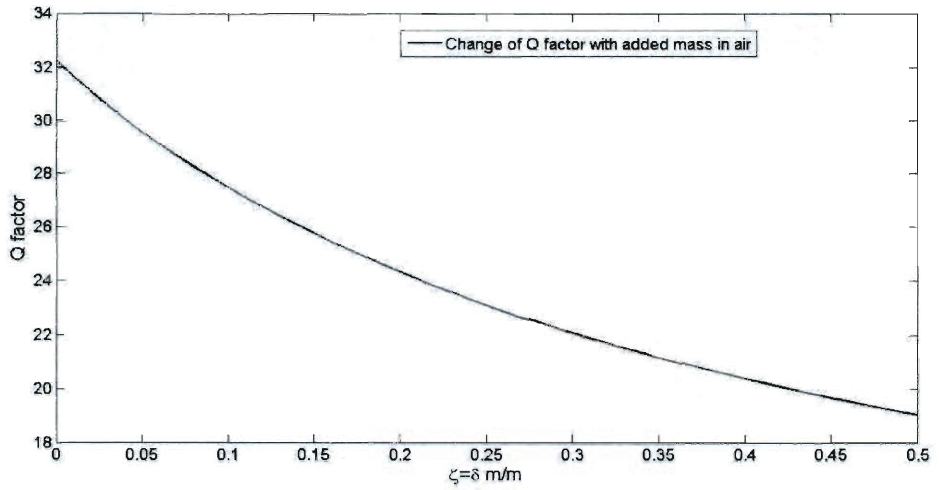

Figure 2-10, Q factor change due to added mass for NEMS in air

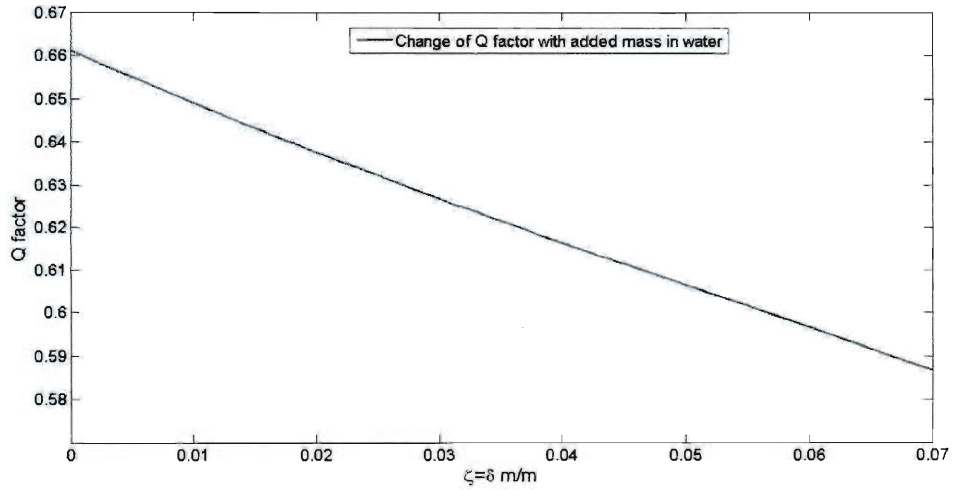

Figure 2-11, Q factor change due to added mass for NEMS in water

2.3.3 Mass sensitivity in liquid

Liquid reduces both resonance frequency and Q factor for NEMS devices; this will significantly affect inert mass sensitivity. Equation (2.19) can be written as

$$|h_i(\omega)|^2 = \frac{C_n}{\left(\omega_n^2 - \omega^2\left(1+\frac{\pi}{4}\frac{\rho_f b^2}{\mu}\Gamma_r\right)\right)^2 + \left(\frac{\pi}{4}\frac{\rho_f b^2}{\mu}\Gamma_i\omega^2\right)^2} \qquad (2.22)$$

In low dissipation and near resonance frequency, resonance frequency and Q factor have been given by Sader[24]. Plugging in Sader's equations into function given by Ekinci[59], minimum resolvable mass can be written as

$$\delta M = K_n \left[\frac{T^{1/2}\Gamma_i}{(1+T\Gamma_r)^{1/2}} \right]^{1/2} \equiv K_n f(T, \mathrm{Re}) \tag{2.23}$$

While K_n is a constant independent of fluid, $T = \frac{\pi \rho_f b^2}{4\mu}$ is the ratio of liquid mass to solid mass. Thus, mass sensitivity in liquid is function of the mass ratio and Reynolds number. The minimum resolvable mass relative to Reynolds number and mass ratio are shown in Figure 2-12. Figure 2-12 indicates that to achieve higher sensitivity, larger Reynolds number and smaller liquid mass are desired. From definition of Reynolds number(2.20), larger Reynolds number means smaller viscosity; this is understandable because smaller viscosity means less dissipation. The overall impact of fluid to the mass sensitivity is detrimental.

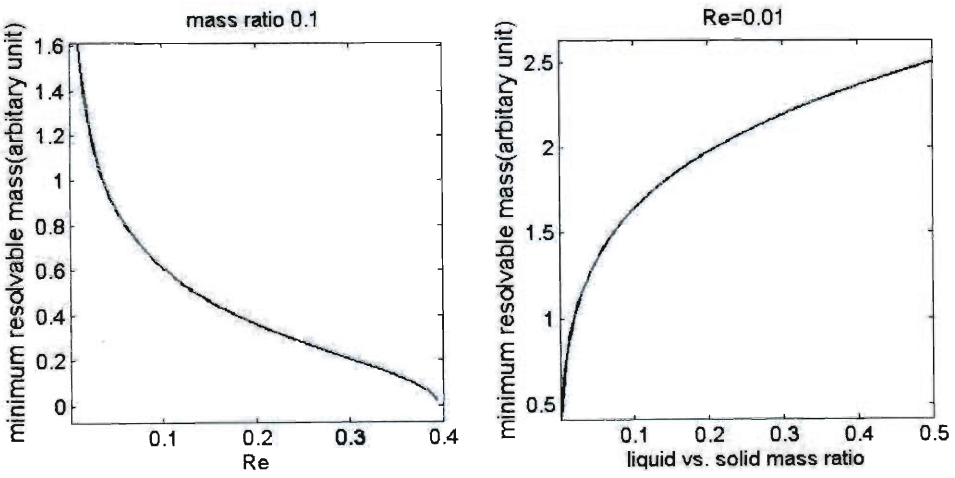

Figure 2-12, mass sensitivity with respect to Reynolds number (left figure) and mass ratio (right figure)

If we fix all material related constants and change the scale of the system, the scaling law of mass sensitivity under the influence of fluid can be obtained as followed.

$$\begin{aligned} \mathrm{Re} &= \frac{\rho\omega b^2}{4\eta} \sim \omega b^2 \sim \frac{1}{L}\sqrt{\frac{EI}{\mu}}b^2 \sim \frac{b^3}{L^2} \sim b \\ K_n &\sim M \sim \rho b^2 L \sim b^3 \\ \delta M &\sim b^3 f(T, \mathrm{Re}) \sim b^3 f(T, b) \sim \mathrm{Re}^3 f(\mathrm{Re}) \end{aligned} \tag{2.24}$$

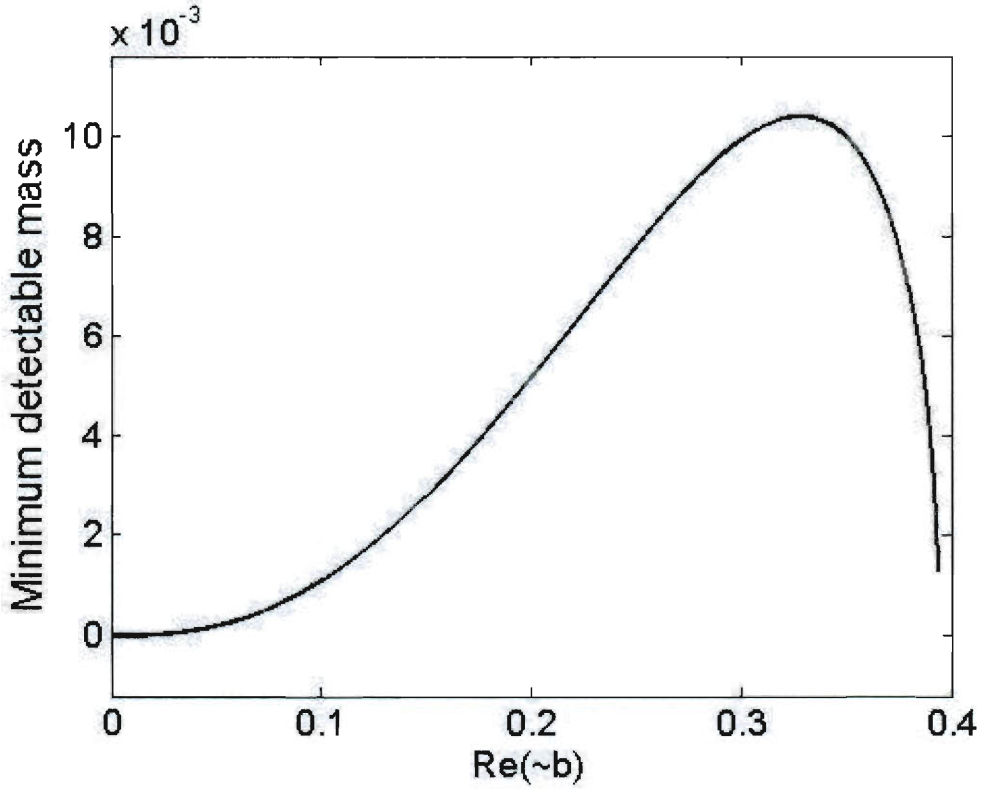

Figure 2-13, Scaling law of mass sensitivity due to influence of fluid

Figure 2-13 shows that minimum detectable mass decreases with scaling down of the system. It also predicts a "worst" sensitivity in some middle range of Re. Increasing size of the system even higher over the "worst" sensitivity range predicts comparable sensitivity with smaller scale. However, this scaling law may not describe the system

with larger scale due to ignorance of other dominant dissipations in larger system. This scaling law applies to smaller system because at lower scale and viscous fluid, fluid effect dominates other dissipations.

Furthermore, above calculations assume high Q factor. This assumption breaks down in large density and viscous fluid. Complete calculation of power spectral density (PSD) has to be considered. The PSD from fluctuation of liquid can be written as

$$S_x(\omega) = |h_i(\omega)|^2 G_f(\omega) \tag{2.25}$$

$h_i(\omega)$ is the transfer function given by (2.19) and $G_f(\omega)$ is spectral density function of fluctuation force given by[96].

$$G_f(\omega) = 4k_B T \omega \Gamma_i(\omega)\left(\frac{\pi}{4}\rho_f b^2\right) \tag{2.26}$$

PSD for liquid fluctuation ($S_x(\omega)$) and PSD for unit force excitation ($|h_i(\omega)|^2$) at the first mode are demonstrated in Figure 2-14.

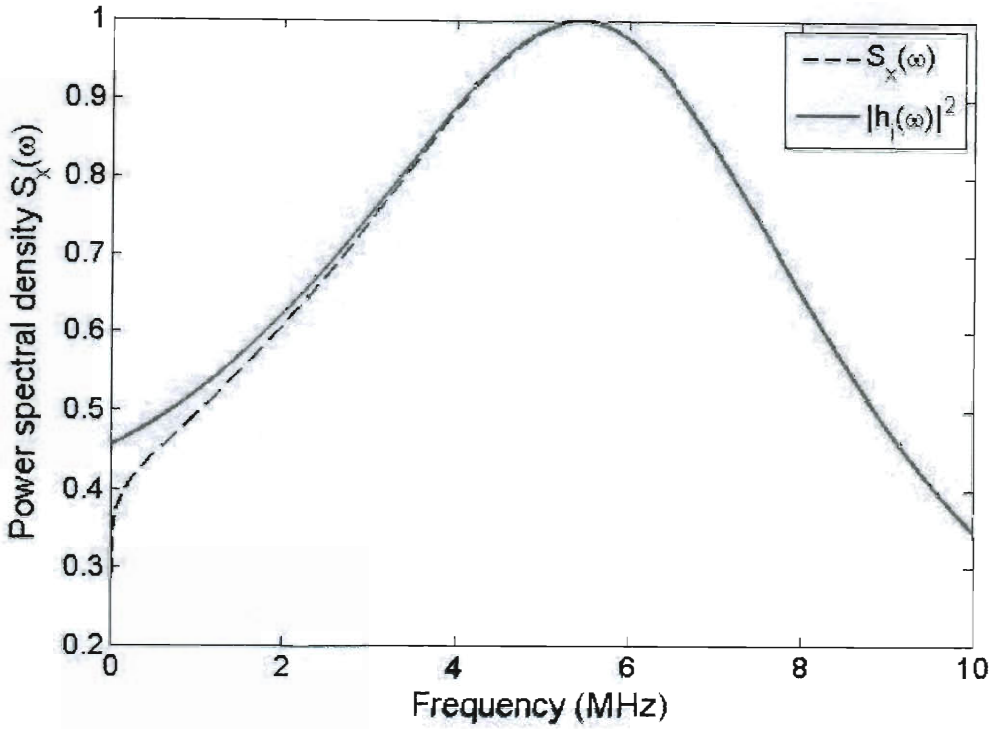

Figure 2-14, Power spectral density of liquid fluctuation and unit excitation

PSD of liquid fluctuation has smaller Q factor compared with that of unit excitation; and their peak frequencies are almost the same. Given the same bandwidth, more energy is concentrated near peak frequency for PSD of liquid fluctuation. While the mass sensitivity is proportional to excitation energy vs. liquid fluctuation ratio $\delta m \propto \frac{\int_{\omega_0-\Delta\omega}^{\omega_0+\Delta\omega} S_{liquid}(\omega)d\omega}{E_{excite}}$, sensitivity is smaller than the case of white thermal spectral discussed by Ekinci[59].

2.4 Actuation of NEMS in liquid

Magnetomotive method was used to actuate NEMS device of suspended gold nanowire.

Coplanar waveguide (CPW) was defined with characteristic impedance of 50Ω to match that of coaxial cables. Line width and space were calculated using an online calculator[1]. A patterned CPW is shown in Figure 2-15.

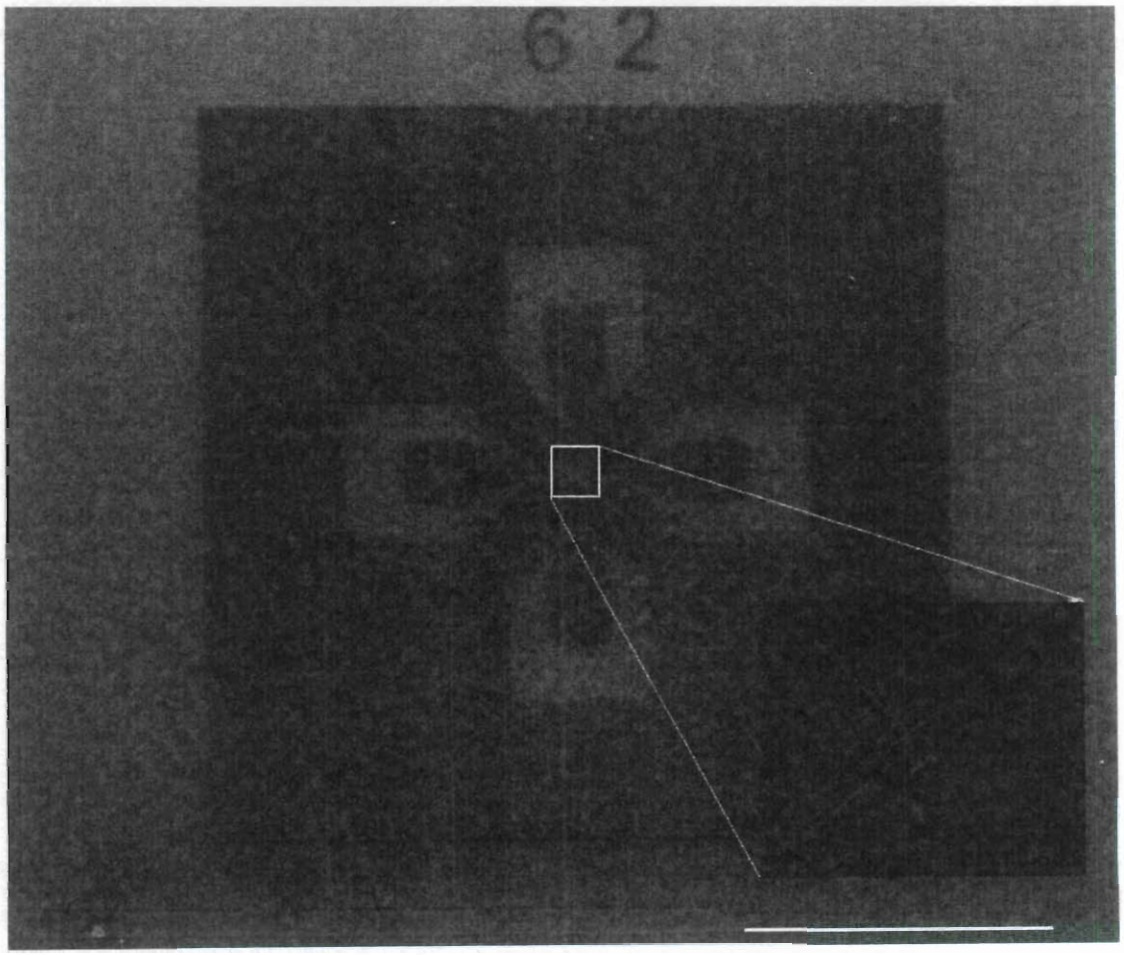

Figure 2-15, CPW with clamped nanowire, scale bar is 500um

[1] http://www1.sphere.ne.jp/i-lab/ilab/tool/cpw_e.htm

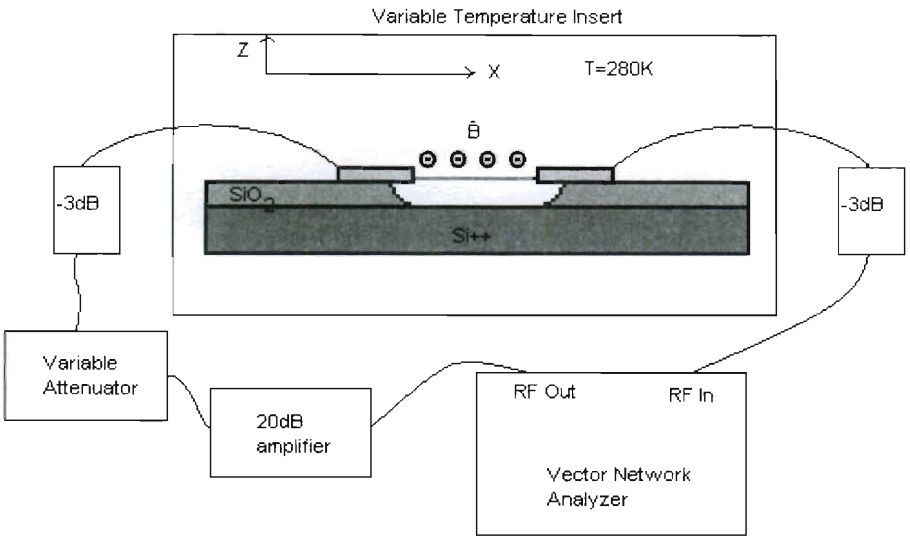

Figure 2-16, Schematics of the magnetomotive experiment[99]

Device was mounted in a chip carrier and inserted into a variable temperature insert (VTI)[99]. RF current was provided by a network analyzer[2] and S_{21} transmission signal was measured. Sample was characterized both in vacuum and silicon oil with kinematic viscosity of 10 cSt. The oil was sealed into the cavity of chip carrier using glass lid. Two peaks were seen in vacuum, but only one peak was found in silicon oil as shown in Figure 2-17.

[2] Anritsu

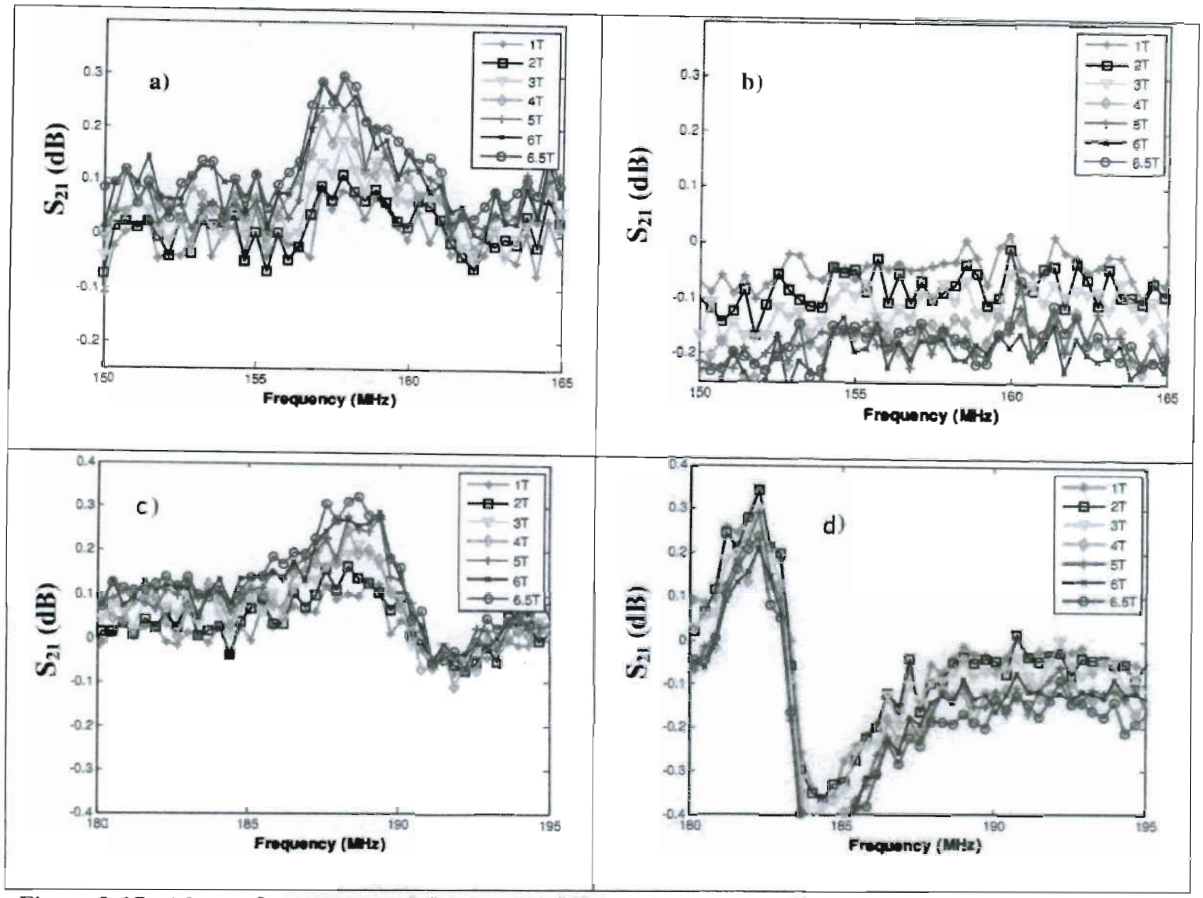

Figure 2-17, a) lower frequency peak in vacuum, b)lower frequency peak disappeared in oil c) higher frequency peak in vacuum c) higher frequency peak in oil[99]

Data in Figure 2-17 a) and c) demonstrated location of the two peaks at 157MHz and 188MHz respectively. Theoretical calculation of the resonance frequency for a 1um long, 70nm diameter gold nanowire is about 400MHz, the discrepancy might be related to the uncertainties of geometry measurement of nanowire. For all resonance modes, amplitude should decrease when sample is immersed into liquid. Furthermore, the peaks at lower and higher frequencies could not be assigned to adjacent resonance modes (equation(2.18)). Further investigation is required.

2.5 Conclusion

NEMS devices can be characterized using forced oscillation or free damping techniques. Common way to extract system parameters as resonance frequency and Q factor involves nonlinear fitting to noisy experiment data. Transfer of measurement noise to fitted parameters uncertainty is thus nonlinear. Relative parameters uncertainties are closely related to mean system parameters; and they also depends on measurement techniques. For low Q factor, it would be advantageous to use free damping technique; while for high Q factor, forced oscillation would be better.

Damping of NEMS devices in fluids had been studied using Euler beam theory and Navier-stokes equations. Point mass at the end of the beam changes beam's resonance frequency and Q factor. It had been shown the change of relative resonance frequency due to added mass predicted from beam theory was larger than formula given by SHO. The fluid, due to energy loss and added fluid mass, decreases Q factor significantly, which might restrict using NEMS resonator in fluid. Change of NEMS resonator materials and using higher resonance modes are possible ways to solve these problems.

Attempts to actuate suspended gold nanowires using magnetomotive force resulted in questionable results; further investigation is needed in the future.

Chapter 3 Piezoresistive effect of gold nanowires

3.1 Introduction

Strain induced electrical resistance change has been discovered more than one hundreds year ago. Strain gauge factor (GF) was introduced to quantify this effect and was defined as $GF = \frac{\Delta R / R}{\varepsilon}$. And this effect is highly related to NEMS signal as shown below.

Recall from 1.2.2 and 1.2.3 about magnetomotive actuation and sensing technique, the signal can be written as

$$\begin{aligned} V &= V_0 e^{i\omega t} \\ F &= IBl \\ F &= kx \\ v &= \xi Bl\dot{x} = \xi Bl\frac{\dot{F}}{k} = \xi B^2 l^2 \frac{\dot{I}}{k} = \xi B^2 l^2 \frac{1}{k}\left(\frac{i\omega V}{R} - V\frac{\dot{R}}{R^2}\right) \end{aligned} \tag{3.1}$$

There are two terms in $v(t)$, one is $i\omega V$, and another is $V\frac{\dot{R}}{R^2}$. The ratio between these depends on gauge factor (GF) as proven below.

Time derivative of R is proportional to strain by $\dot{R} = GF \times \dot{\varepsilon} R = i\omega GF\varepsilon R$. The ratio between the first term and the second term in $v(t)$ is thus

$$\frac{\frac{V\dot{R}}{R^2}}{\frac{i\omega V}{R}} = GF\varepsilon \le GF\varepsilon_0 \tag{3.2}$$

ε_0 is maximum strain; for magnetomotive excitation setup, ε_0 is small ($\sim 10^{-4}$). For bulk materials, GF is smaller than ten for metal and within hundreds for semiconductors.

Recently, nanomaterials have shown higher strain gauge factor than traditional strain sensors. Different kinds of materials from metallic and semiconductor Carbon Nanotube (CNT) [100-103] to piezoelectric Zinc Oxide (ZnO) [104] and silicon nanowires[105] have been found to have extraordinary strain gauge sensitivity. The novel materials listed above, on the one hand have large gauge factor, and on the other hand are sensitive to other stimulus as chemical environment[106-107], temperature[108]. Separation strain effect from other stimulus will be challenging. Gold, as a noble metal, is inertial to chemical environment and has been used in traditional thin film strain gauge. On the other hand, it has been found that size dependent conductivity due to surface scattering and grain boundary scattering play important role in nanosize metal materials [109-111]. It would be interesting to study how the size effect affects the strain gauge factor in metal nanomaterials. In this chapter, strain gauge factor of suspended gold nanowire was studied.

3.2 Sample preparation

Samples were prepared on silicon wafers with 300nm of silicon dioxide sacrificial layer. Two levels of electrodes were used: larger electrodes (mm) were used for wire bonding to chip carriers, and smaller electrodes (nm) connected nanowires to larger electrodes. Large electrodes were defined on silicon wafer with photolithography and Electron Beam (Ebeam) evaporation technique. Gold nanowires (NWs) obtained from Professor Zubarev[112] were sprayed onto the silicon wafer. Ebeam lithography was then used to make smaller electrodes. Finally, the NWs were suspended by etching away underneath silicon dioxide layer. Critical Point Dryer (CPD) was used to prevent surface tension that

might pull suspended NWs/NTs down to the wafer surface. Detailed steps and conditions are listed in Table 3-1. Following sections described fabrication steps.

3.2.1 Liftoff with positive photoresist S1813

Liftoff is a technique of creating structures on substrate with sacrificial materials. An ideal liftoff step is demonstrated in Figure 3-1. In this ideal case, the wall of the patterned photoresist is vertical and after liftoff, metal deposited on sacrificial photoresist is gone. However, in reality, the side wall of patterned photoresist is not vertical to the substrate and metal is continuous all over the surface, which makes it hard to remove metal on top of photoresist. This results in metal hangover as demonstrated in Figure 3-2. To solve this problem, the metal must be discontinuous at the edge of the pattern. This discontinuity is realized by using another sacrificial layer formed of LOR5B. LOR5B is etched by developer MF319 quicker than exposed S1813 if properly prepared, thus, an undercut is created and unwanted residual metal is removed.

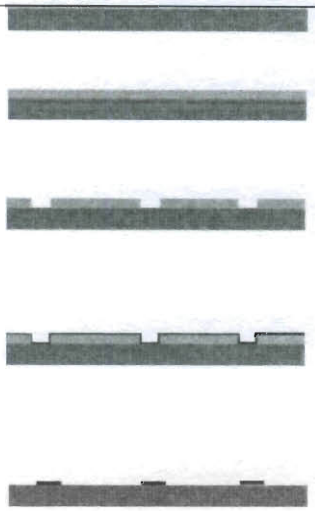

Figure 3-1, ideal liftoff process; the wall is vertical and no residual metal after liftoff

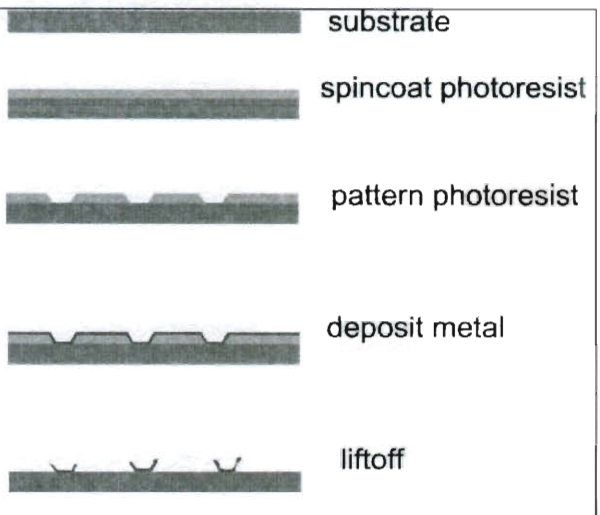

Figure 3-2, patterned photoresist with sloped sidewall results in continuous metal and residual metal after liftoff

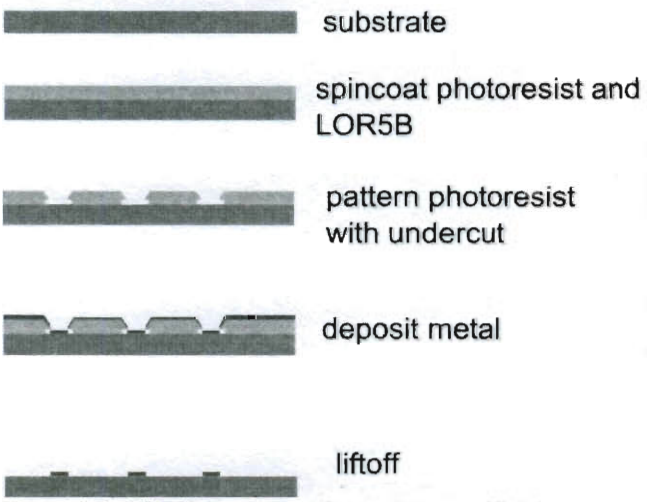

Figure 3-3, Liftoff process with another sacrificial layer LOR5B. Undercut is created and deposited metal is discontinuous.

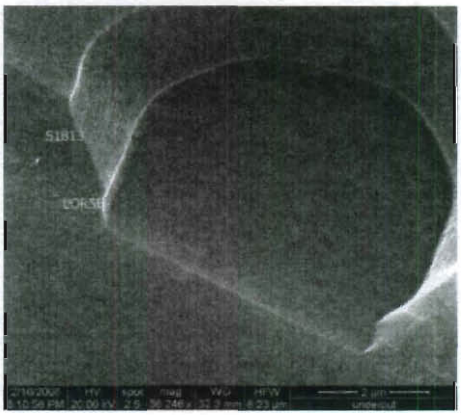

Figure 3-4 SEM image of the undercut of LOR5B below S1813 after patterning, before metal deposition

3.2.2 Ebeam lithography

Unlike photolithography, Ebeam lithography doesn't require a mask and pattern is written once. This one-time writing is desired because the Ebeam lithography was used here to create electrical connections between randomly orientated nanomaterials and

photolithography defined contact pads. To make electrical connections, the location of nanomaterials with respect to contact pads must be found. Fine patterns can be created on PMMA (Poly (methyl methacrylate)) film because polymer chain of PMMA can be broken by energetic electron beams (30kV). Using SEM to look at PMMA coated sample enough time will exposure the PMMA; thus, locating of nanowires by SEM after PMMA coating is prohibited. Nanowires were located before coating of PMMA. After PMMA is coated, a quick SEM picture was taken. This quick scan exposed the area to be written with a scan rate of 300ns per line, which was not long enough to break enough PMMA chains. Image processing software was used to align pictures taken before and after PMMA coating. Then patterns could be defined based on the new picture. There is no residual metal problem in Ebeam lithography because the back scattered electrons from the silicon substrate create undercut in PMMA film (Figure 3-6).

After writing, chrome and gold were evaporated and a liftoff process finalized the connections. Chrome was used as adhesion layer to increase bonding between gold and SiO_2. Another typical adhesion material is titanium; however, since titanium is etched quickly by hydrofluoric acid used in later step, use of titanium was avoided here. In order to firmly clamp the nanowires, thick enough metal layers must be deposited. On the other hand, thicker film caused peel off problem during releasing step (Figure 3-8). As the thickness of film increases, internal stress built up[113]; and this large internal stress lead to failure of electrodes when device was being released in hydrofluoric acid.

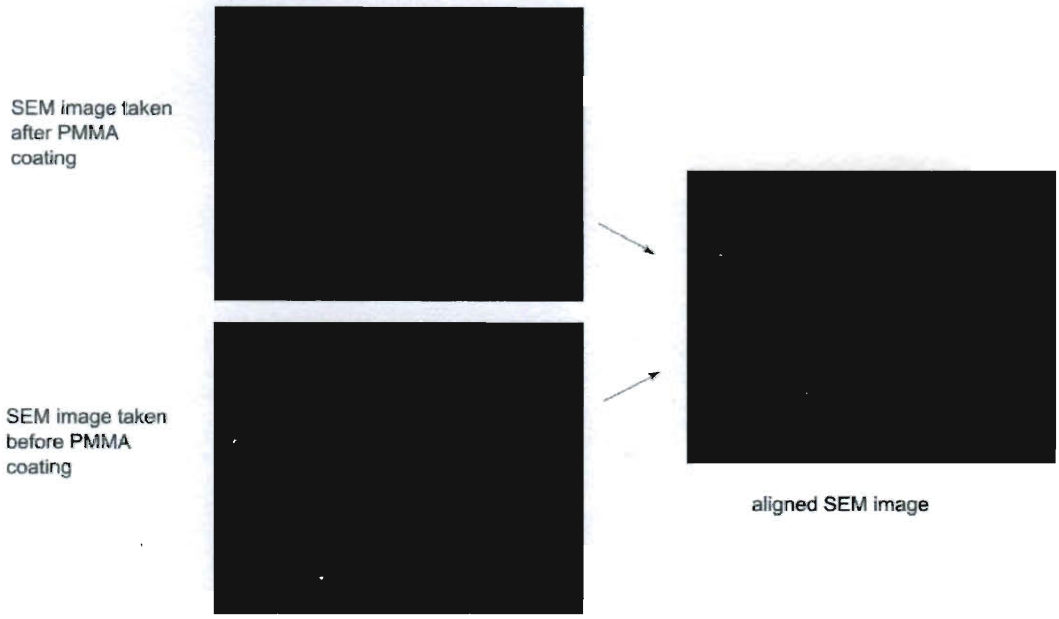

Figure 3-5, Alignment for Ebeam lithography, a high resolution SEM image taken before PMMA coating was aligned with low resolution SEM image taken after PMMA coating using imaging processing software[3].

Special SEM stage, which includes a Faraday cup, and a standard sample, was used for lithography. The Faraday cup was made of a cylinder recess covered with a disk that has a hole of 100um in diameter. The standard sample was a piece of silicon with nanometer size nickel particles made using high temperature annealing.

[3] Gimp

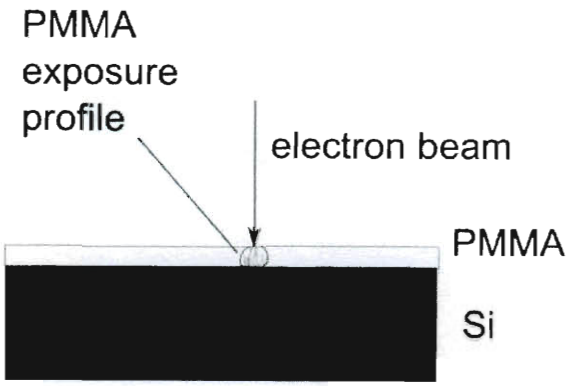

Figure 3-6, demonstration of PMMA exposure profile, undercut is automatically formed because of the back scattered electrons from Si substrate

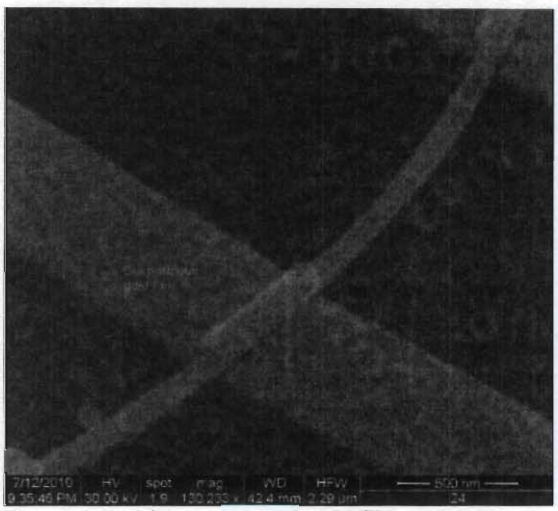

Figure 3-7, thin evaporated gold film was not able to firmly clamp large diameter nanowire

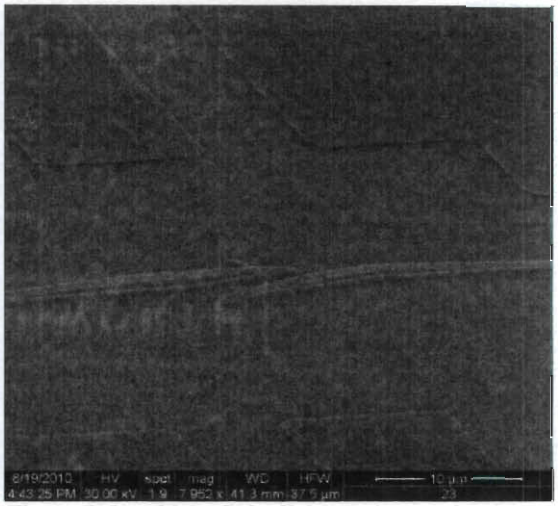

Figure 3-8, gold peeled off due to internal stress

3.2.3 Suspension and Critical Point Drying

Suspension of nanomaterials was achieved by removing materials underneath them. The layer to be removed underneath the nanomaterials is called sacrificial layer. Silicon dioxide (SiO_2) was used here. It can be removed with anisotropic Reactive Ion Etching

(RIE) or isotropic wet chemical etching. RIE is good at etching high anisotropic profile nearly vertical at the edge. The nanowire device with RIE etched was shown in Figure 3-9a, from which the formation of a thin SiO_2 wall underneath the gold nanowire is visible.

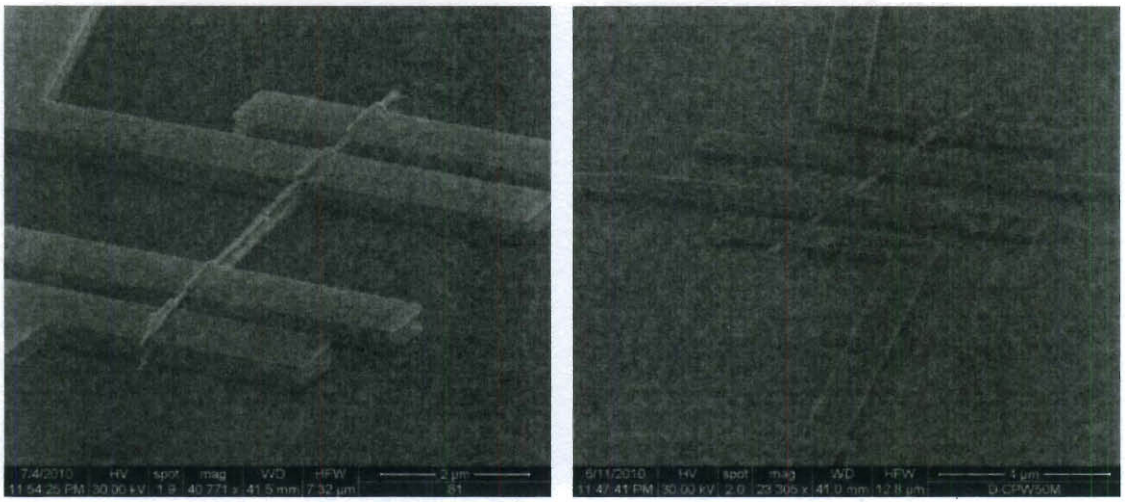

a **b**

Figure 3-9, (a) RIE etched. (b) hydrofluoric acid etched

Hydrofluoric acid (HF) was used to isotropically etch SiO_2. A typical result shown in Figure 3-9b demonstrates the suspended nanowire. HF attacks same amount of SiO_2 in the vertical and horizontal directions. This feature on the one hand results in desired suspension of nanowire; and on the other hand, creates undercut on electrodes. It also limits the maximum suspension height to half of the electrodes width if electrodes are not suspended.

To overcome the problems with RIE etching and wet chemical etching, the sacrificial SiO_2 layer was removed using two step etching technique. The first step was anisotropic RIE etching of SiO_2 vertically down to hundreds of nanometers and the second step was

an isotropic etching by diluted HF (1 HF: 10 water by volume, 23nm/min [106]). Anisotropic etching was used to etch deep down which determines the suspension height of the nanowires. Isotropic wet etching was used to remove thin SiO_2 wall underneath the nanowire. By using two step etching, suspension height will not be restricted by width of electrodes. Result of the two step etching technique was demonstrated in Figure 3-10.

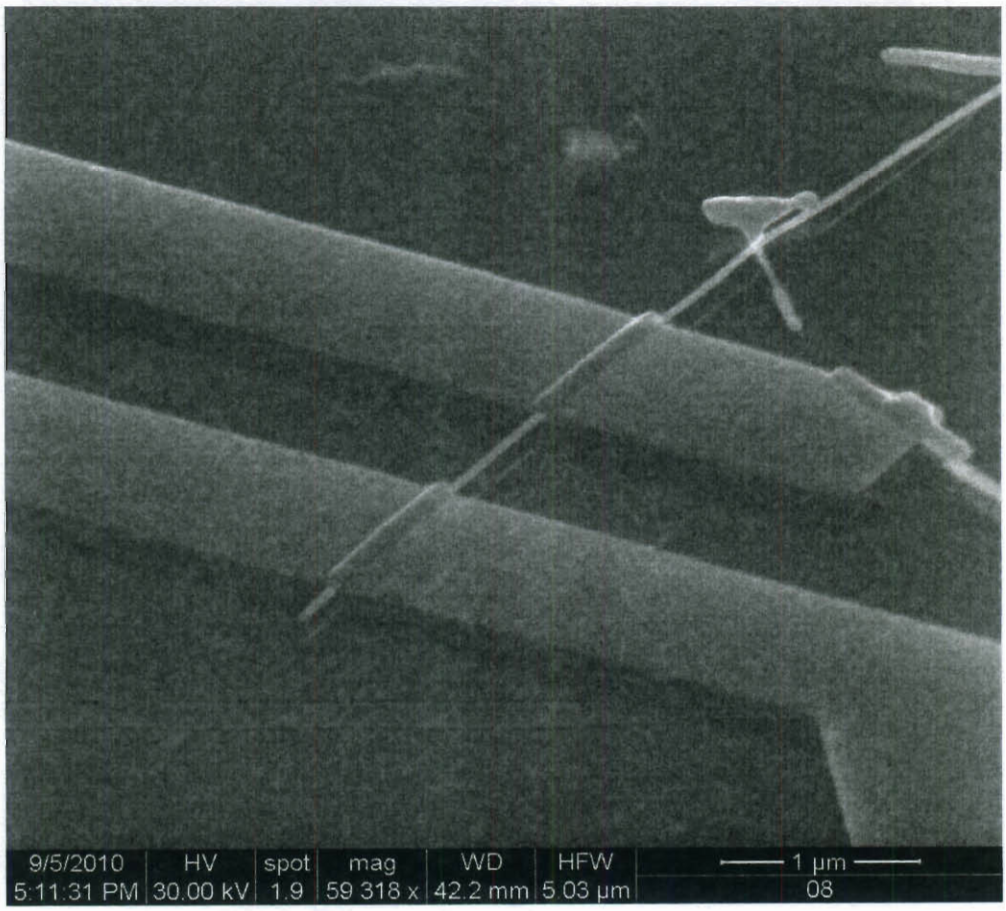

Figure 3-10, Suspended gold nanowire using two-step SiO_2 etching technique, suspension height is about 200nm with few undercut below electrodes.

After wet chemical etching, samples must be dried surface tension free or the suspended nanowire will be pulled down by surface tension. Critical Point Drying (CPD) was used

to dry samples without surface tension. CPD brings the initial liquid phase to supercritical region where no distinction exists between liquid and gas; CPD then removes matter in supercritical state. Sample was dried out under triple point of CO_2. A custom designed Teflon cup was used to transfer samples without exposure to air. Samples were placed in the cup and immersed into hydrofluoric acid for about 90 seconds and then transferred to DI water tank. After cleaning the acid, water was first replaced by ultra pure alcohol outside; and then replaced by liquid CO_2 inside CPD chamber.

Steps	Detailed conditions
Photolithography	• Spincoat LOR5B[4] 4000rpm, 44secs • Bake @ 150 °C for 5mins[5] • Spincoat S1813[6] 4000rpm, 44secs • Bake @ 115 °C for 1min • UV light 365nm exposure[7] 150mw/cm^2 • Developer MF319 50secs
Ebeam evaporation	• 5nm chromium (Cr) at rate of 4Å/s • 70nm gold at rate of 1Å /sec
Liftoff	• Acetone 3 hours (removes S1813) • MF319 2mins (removes LOR5B) or Remover 1165 @60 °C for 30mins
Ebeam lithography[8]	• Spincoat PMMA 3000 rpm, 40secs • Line dose 1.3nC • Developed MIKB:IPA (methyl–isobutyl–ketone:isopropanol)=1:3, 35 secs
Ebeam evaporation	• 5nm Cr • 70nm gold

[4] Microchem
[5] Dissolving speed of LOR5B depends on baking temperature and time. Lower temperature and shorter time results in faster dissolving speed. A reasonable speed is desired because faster speed causes extra undercut and collapse of top layer film while slower speed causes residual of LOR5B film.
[6] Microchem
[7] SUSS mask aligner MJB4
[8] FEI Quanta400 and NPGS

Liftoff	• Cut a line on PMMA film • Soak in acetone 3 hours
suspension	RIE (power 150W, ICP 200W, pressure 45, O_2 2sccm, CHF_3 23sccm, 1:30 min) Diluted (Hydrofluoric acid) HF (1:10 water) for 1:30 min
Critical point drying[9]	Alcohol and liquid CO_2

Table 3-1, Steps of sample preparation and detailed experimental conditions

3.2.4 Pattern Design for photolithography

The electrodes for wire bonding are designed to fit AFM scanner. The Agilent AFM 5500 features top scan configuration; scanner head driven by piezo tubes is moving above sample, while the sample stage stays stationary. A schematic configuration of relative position of the AFM scanner head, the sample, and bonding wire is demonstrated in Figure 3-11. Electrodes were designed to be as large as millimeters and the ends of all six electrodes were oriented to the same direction to avoid bonding wires crashing AFM

[9] Automegasamdri-915B

probes.

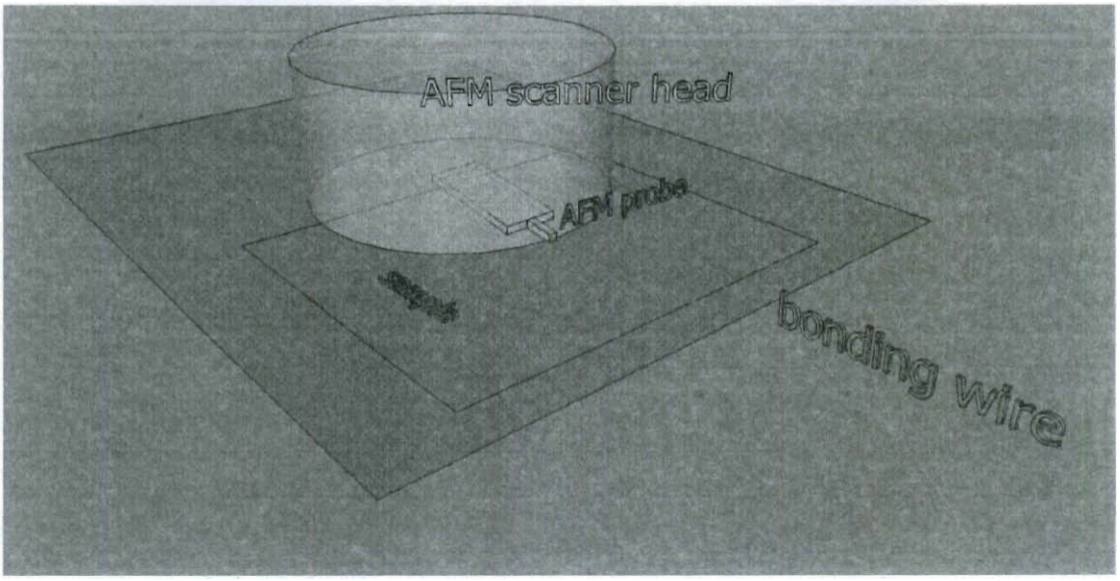

Figure 3-11, relative locations of the AFM scanner, sample and bonding wire

3.3 Measurement

3.3.1 Electromechanical testing

AFM was used to provide mechanical deformation on suspended nanostructure while electrical properties of the nanowire were monitored with Keithley source meter. Schematic of the setup was demonstrated in Figure 3-12.

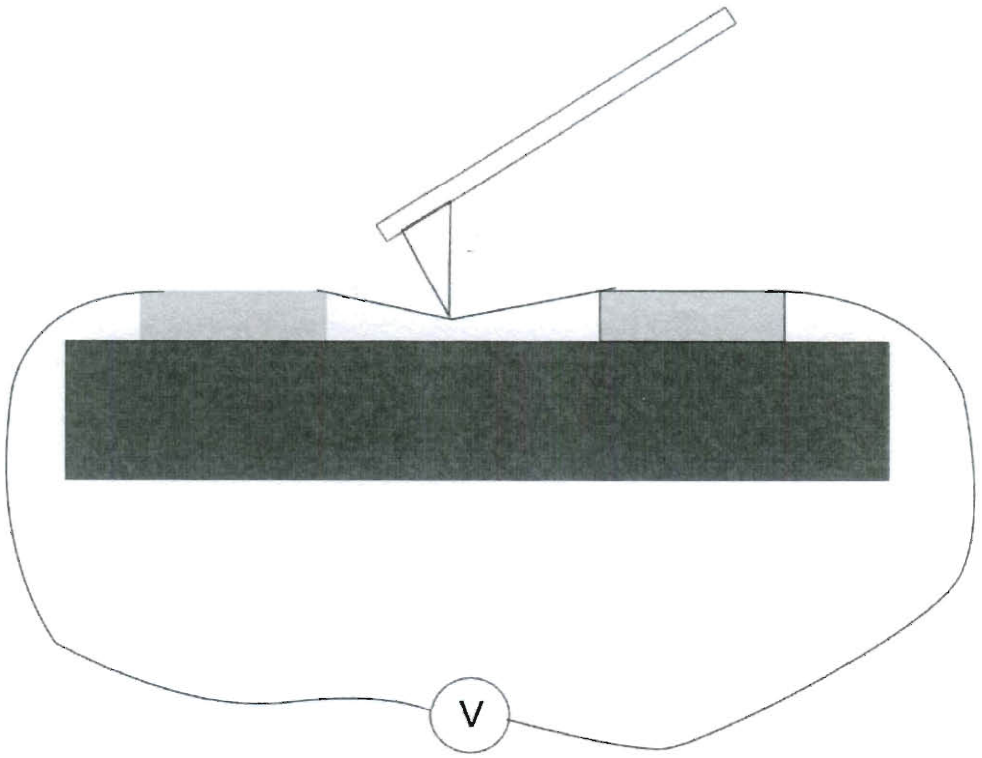

Figure 3-12, Schematics of electromechanical coupling measurement with AFM and DC source meter

A system was built to provide interface from electrical characterization system to the AFM. The system was composed of a metal switch box and a PCB board. An aluminum box with BNC bulkheads was used to control electrical connection from sample to measurement apparatus. Samples were taped down inside a LCC (Leadless Ceramic

Carrier) chip carrier and electrodes on sample were wire-bonded to LCC's electrodes. The chip carrier itself was soldered to a PCB SchmartBoard©. Shielded twisted pair cable with one end solder inside the BNC switching box; and the other connected to a female RS232 connector. An AFM holder designed based on original one was built to hold the PCB SchmartBoard with metal clips.

Extra care is required to handle gold nanowires, which are vulnerable to static discharge (Figure 3-13). Grounding experimentalist would not solve the problem because of the low resistance and small diameter of nanowire. Instead, experimentalist was isolated from the devices. After evaporation of gold (Table 3-1), devices were handled with insulating plastic tweezers. All electrodes were shorted before testing. Two short circuits, one inside switch box and the other on the SchmartBoard, provided static discharge protection. The short circuit inside the switch box was composed of six independent toggle switches; and DIP (Dual in-line package) switch was soldered on SchmartBoard.

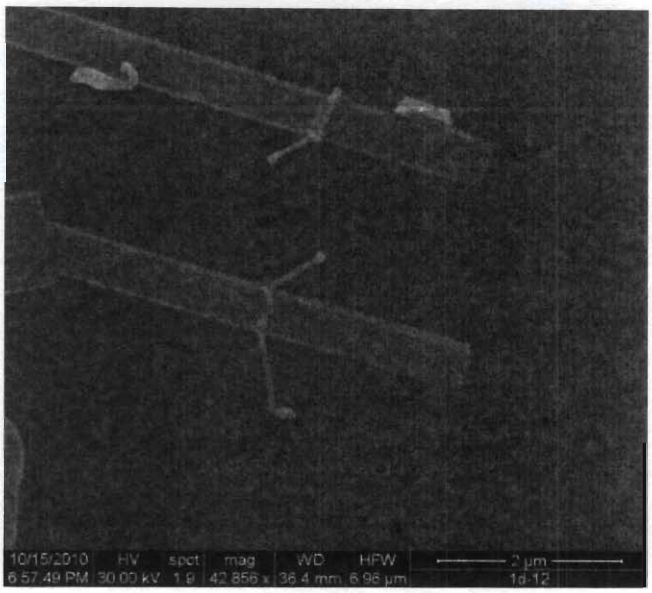

Figure 3-13, gold nanowire damaged by static discharge

3.3.2 Environment control chamber

In order to test sensing abilities of nanodevices, an environmental control chamber is required. The Agilent PicoPlus 5500 AFM has a commercial glass environmental control chamber, however, lack of electrical interface rules out the possibility of using it. A vacuum chamber was designed based on a commercial one[10]. The chamber should be:

1. Large enough to enclose the whole AFM scanner head
2. Have electrical feedthroughs for AFM controller signals and electrical measurement
3. Have gas inlet and outlet

The final design was shown in Figure 5-2 (Appendix). The top three electrical feedthroughs were for AFM controllers. One DB44, one DB9, and one micro-D9 feedthroughs were placed on the top. A few DB44 female to female gender changers

[10] Abbess Instrument, Thomas Driscoll

were used. On the left side of the wall were one gas inlet and one DB9 feedthrough. The left side DB9 was used to provide electrical characterization signal pathway. Two NW40 ports on the right side were reserved for future use.

3.3.3 Optimizing AFM operation conditions

Sample was first located by AFM with large scan area; then scan area was reduced to center on the sample. Vertical force was applied on suspended gold nanowire after the nanowire was clearly visible in the view.

It is critical to setup an optimum working condition for imaging and indenting suspended nanostructure. First of all, AFM was used in tapping mode to avoid shear force by contact mode. It is idea to have AFM work in low vertical tapping force and fast response to topography change, while obtaining clear images. However, there are tradeoffs for those requirements. The average tapping force is given by[114] $F_{av} = 0.5ka_0\Delta A / A_0$, while k is the AFM cantilever spring constant, a_0 is the driving amplitude, ΔA is the set point amplitude, and A_0 is the free amplitude. Based on the formula, to reduce tapping force, soft cantilever is desired. However, soft cantilever is prone to adhesion force and lead to instability of the oscillation [115]. It is also desired that low set point and low driving amplitude, but lowering set point introduces instabilities[114]. It was found the optimum operation conditions were:

- Drive amplitude 10%-30% below resonance amplitude
- Setpoint 90% of free amplitude
- Stiff AFM cantilever (40N/m)

Another important parameter is the scan speed. Although theoretically tapping mode AFM won't introduce lateral shear force to samples, in practice, AFM's electrical feedback system may not able to response fast enough for the terrace change and result in large shear force[116]. This situation happens when AFM tip is climbing a step higher than oscillation amplitude (~10nm). An example of damaged suspended gold nanowires by fast scanning were shown in Figure 3-14.

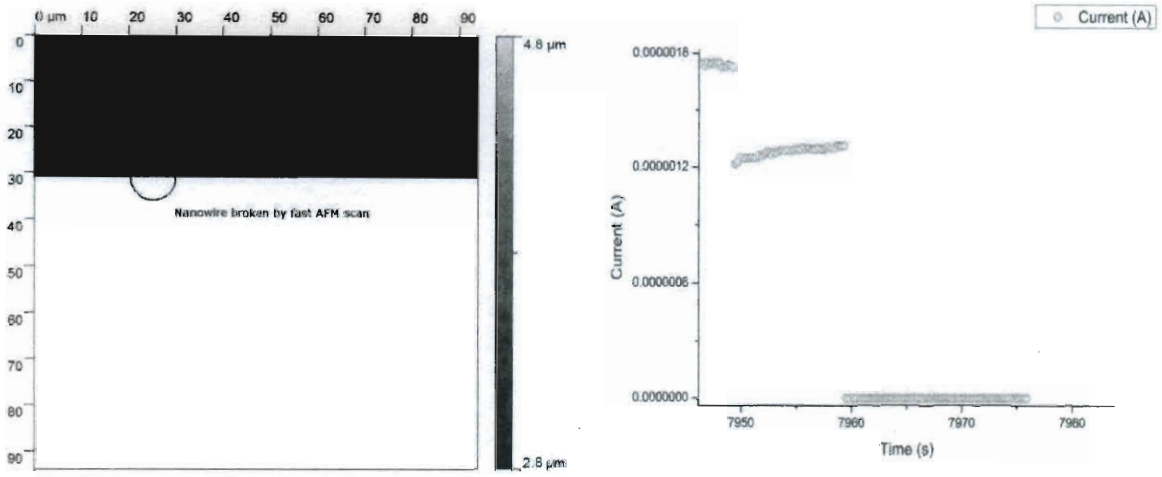

a b

Figure 3-14, a) Half AFM image showing the fast scan destroyed suspended gold nanowire. (b) The corresponding current measurement confirmed damage of the nanowire.

Even though scan speed was reduced to minimum (0.1Hz/line), absolute scan speed for large scan area was much larger than scale of nanowire (~20um/sec). During large scan mode, approximate locations of suspended nanowires could be estimated based on SEM images and partial AFM image. Before AFM probe reached the suspended nanowire,

scan area was reduced; reduced scan speed was thus achieved using the same scan frequency.

If the sample has loosely attached particles, AFM probe might pick one of them up. This added mass reduces cantilever free resonance frequency, as a result, the AFM becomes unstable. It is possible to get rid of the attached particle by driving the AFM to maximum amplitude (100% driving). If it doesn't, the probe has to be taken out and rinsed with IPA (Isopropyl alcohol).

3.3.4 Synchronization of AFM and Keithley

Agilent AFM was controlled by commercial software PicoScan 5.5, while Keithley 2400 source meter was managed by in house LabVIEW software. Synchronization is important to match mechanical data with electrical data. Custom LabVIEW program[11] was used to synchronize measuring time of the AFM and the Keithley using PicoScan's exported groups of ActiveX™ methods and properties. Detailed block diagrams can be found in the Appendix. Due to the slow sampling rate of Keithley source meter, AFM force vs. displacement curve was slowed down.

3.4 Result and discussion

3.4.1 Mechanical properties of gold nanowire

Mechanical properties of suspended gold nanowire can be measured with AFM. The AFM probe was being driven down towards sample by piezo and a piezo travel distance vs. AFM cantilever deflection curve were shown in Figure 3-15. As AFM probe moving

[11] See Appendix

down, the AFM probe touched Au NW, deflection of AFM cantilever increased due to repulsive force between probe and Au NW. The deflection kept on increasing linearly until the NW plastically yielded. Shown in Figure 3-15, it can be seen that after plastic deformation of the NW, cantilever deflection dropped suddenly which probably due to AFM probe slipping off the nanowire. As the probe travelled further down, it touched silicon chip, which corresponds to a faster rise of deflection compared with that of on Au NW.

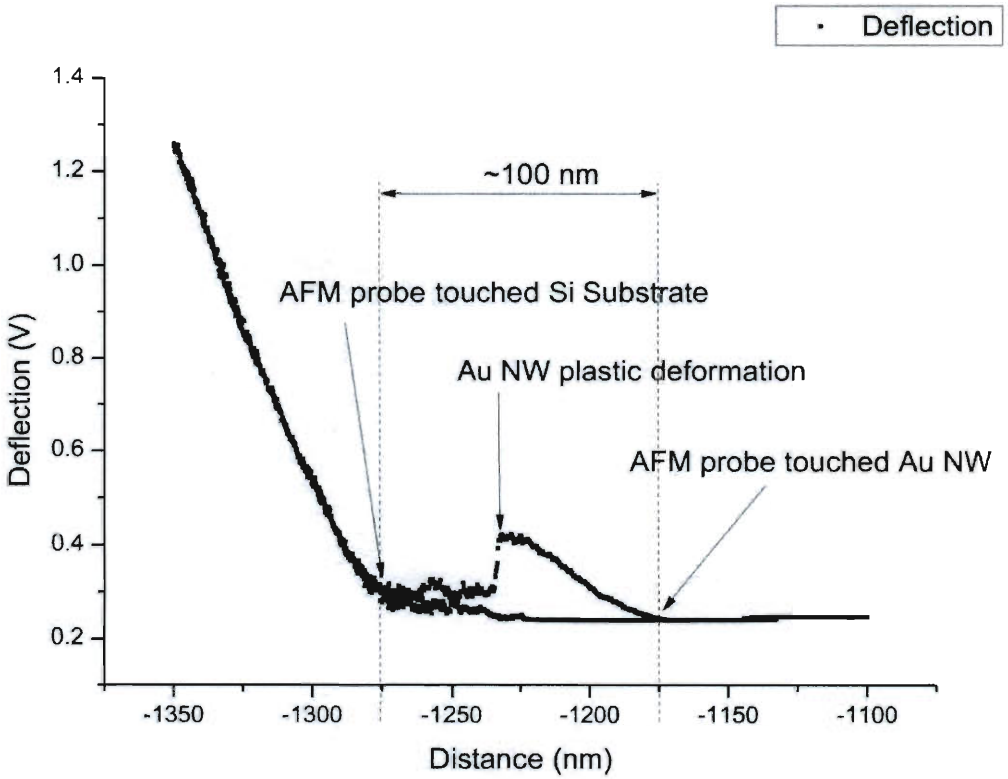

Figure 3-15, Raw AFM deflection vs. distance data, different events were marked, distance between AFM starting to touch Au NW to AFM touched Si substrate is about 100nms, which is the depth of the trench.

The system can be modeled with a double end fixed beam loaded with a point force at the center as shown in Figure 3-16, the shear force v, bending momentum M, and vertical deformation δ can be written as in (3.3).

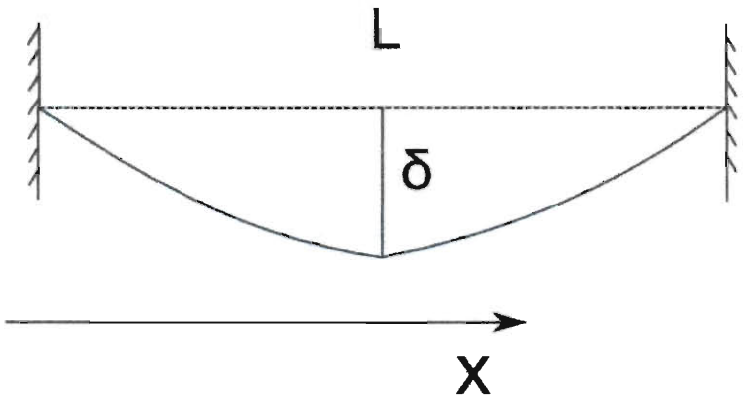

Figure 3-16, bending of the gold nanowire

$$
\begin{aligned}
v &= \begin{cases} \dfrac{F}{2}, & (x < L/2) \\ -\dfrac{F}{2}, & (x > L/2) \end{cases} \\
M &= \begin{cases} -\dfrac{FL}{8} + \dfrac{Fx}{2}, & (x < L/2) \\ -\dfrac{FL}{8} + \dfrac{Fx}{2} - F(x - L/2), & (x > L/2) \end{cases} \\
\delta &= \begin{cases} \dfrac{F}{6EI}\left[\dfrac{x^3}{2} - \dfrac{3x^2 L}{8}\right], & (x < L/2) \\ \dfrac{F}{6EI}\left[\dfrac{x^3}{2} - \dfrac{3x^2 L}{8} - (x - L/2)^3\right], & (x > L/2) \end{cases}
\end{aligned}
\tag{3.3}
$$

F is the force, L is length of nanowire, and E is Young's modulus.

Young's modulus can be calculated as

$$E = \frac{FL^3}{192 I \delta_{l/2}} \tag{3.4}$$

And moment of inertial is given by $I = \frac{\pi r^4}{4}$ and r is radius of the nanowire. Young's modulus is thus proportional to the slope of force vs. deflection curve.

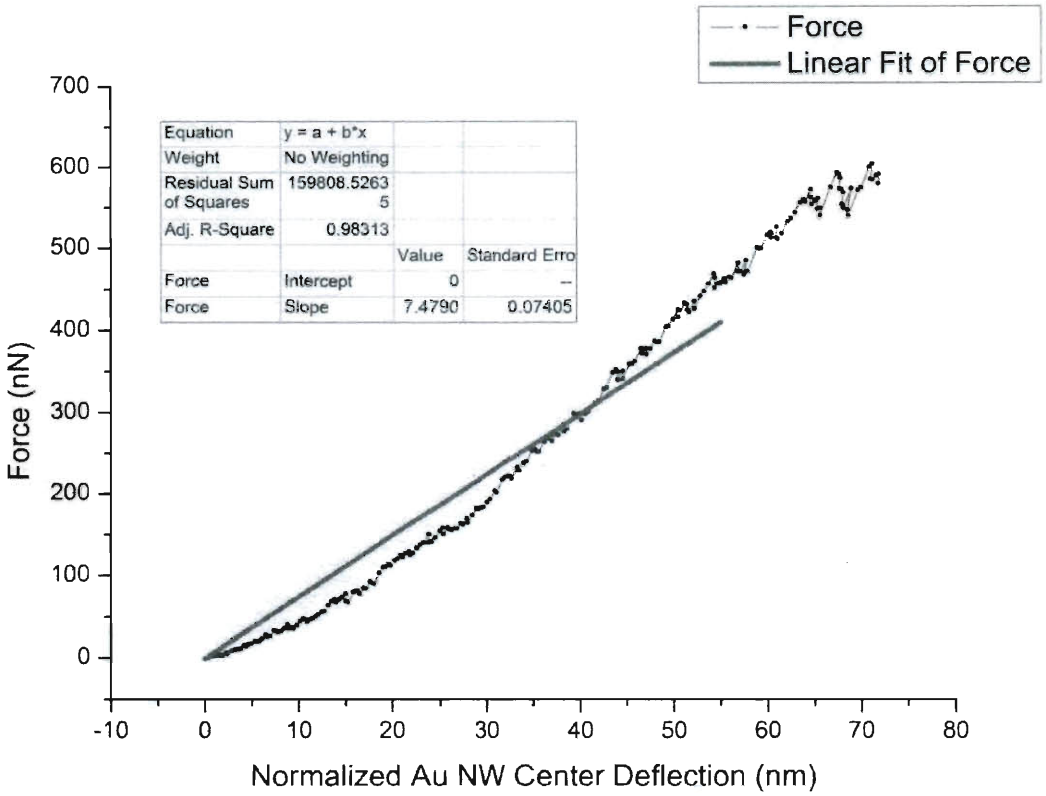

Table 3-2, force vs. Au nanowire center displacement curve fitting

Insert measured parameters $L = 850$, $r = 25$, $F / \delta_{L/2} = 7.48$ into equation (3.4), Young's modulus was about 76Gpa. The measured Young's modulus was comparable with bulk material 79Gpa and within the range given by literature[97]: $E = 70 \pm 11 Gpa$ for gold nanowires.

Yield strength can be calculated using force before plastic deformation with[97]

$$\sigma_y = \frac{F_y L}{2\pi r^3} \tag{3.5}$$

The yield force was chosen as 602.3nN, thus the yield strength being 5.21Gpa, which was comparable to literature result of $3.5 \pm 1.1 Gpa$ for gold nanowire, but larger than bulk gold (55-200MPa). Lager than bulk yield strength was due to less defects, supported by TEM images shown in 3.4.2.

3.4.2 Electromechanical properties of gold nanowire

Electrical resistance of the gold nanowire was monitored simultaneously with mechanical properties. The resistance was found closely correlated with mechanical force as shown in Figure 3-17.

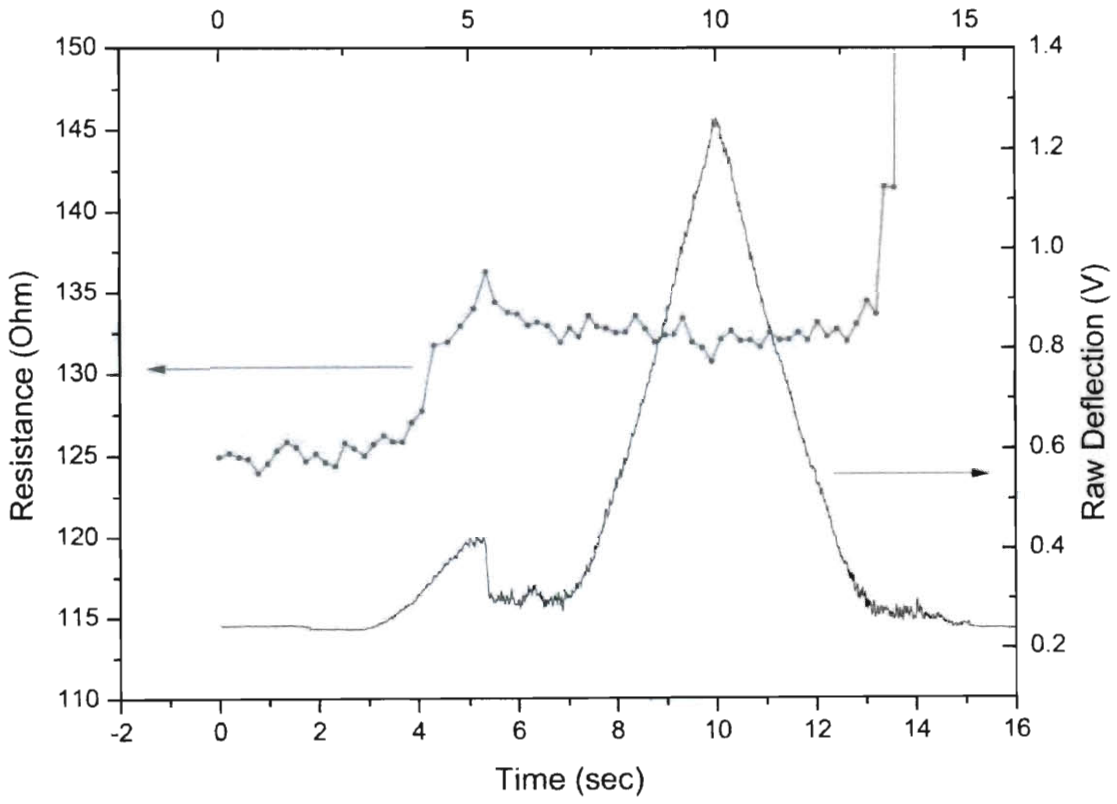

Figure 3-17, correlation of AFM force and resistance change of gold nanowire

Data was then calibrated using method described later in section 4.3. A typical Au NW bending induced resistance change curve is demonstrated in Figure 3-18.

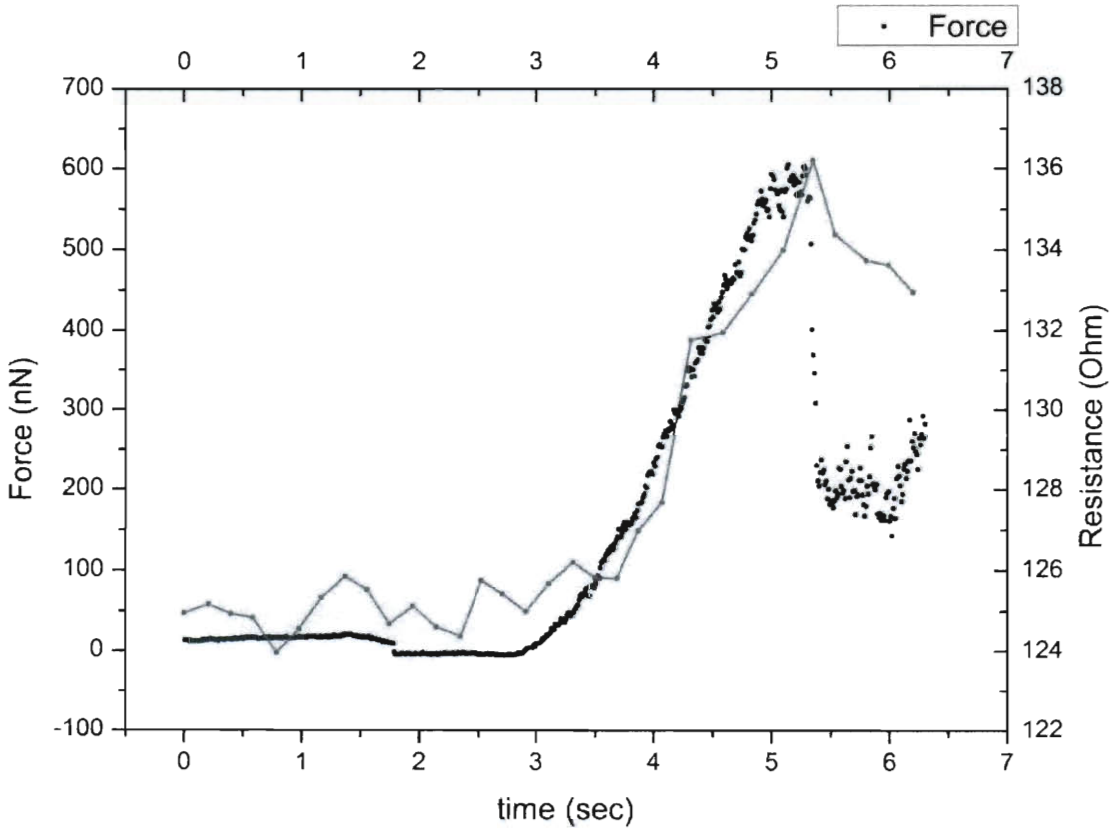

Figure 3-18, Deflection of Au nanowire matches increase of resistance

As seen in Figure 3-18, at 0 second, there was no interaction between AFM probe and the suspended Au NW. At about 1.5 second, deflection slightly dropped, this is due to the adhesion force between AFM probe and Au NW pulled AFM probe in. During this period, no obvious change of resistance was observed. As the AFM probe pushed down further, force changed from adhesive to repulsive and the suspended Au was deformed. At 3 second, both deflection of Au NW and its resistance started to increase. The Force

steadily increased, but at the point just before sudden drop, force fluctuated. Finally at about 5 second, the deflection dropped with reducing of resistance.

Strain of the Au NW could be calculated based on the geometry as shown in Figure 3-16. For an Euler beam, the longitudinal strain is proportional to the bending momentum and also depends on distance from the neutral axis. The signs of strain on two sides of neutral axis are reversed and thus the total effect cancels[117]. A uniform global strain defined by $\Delta L / L$ is used instead, ΔL is the elongation of the nanowire at neutral axis and can be calculated by

$$\Delta L = 2\int_0^{L/2} \sqrt{\left(\frac{32\delta_{L/2}}{L^3}\left(\frac{3x^2}{2} - \frac{3xL}{4}\right)\right)^2 + 1}dx - L \qquad (3.6)$$

And $\delta_{L/2}$ is the displacement at the middle of the nanowire.

The gauge factor of the gold nanowire was fitted using linear function as shown in Figure 3-19.

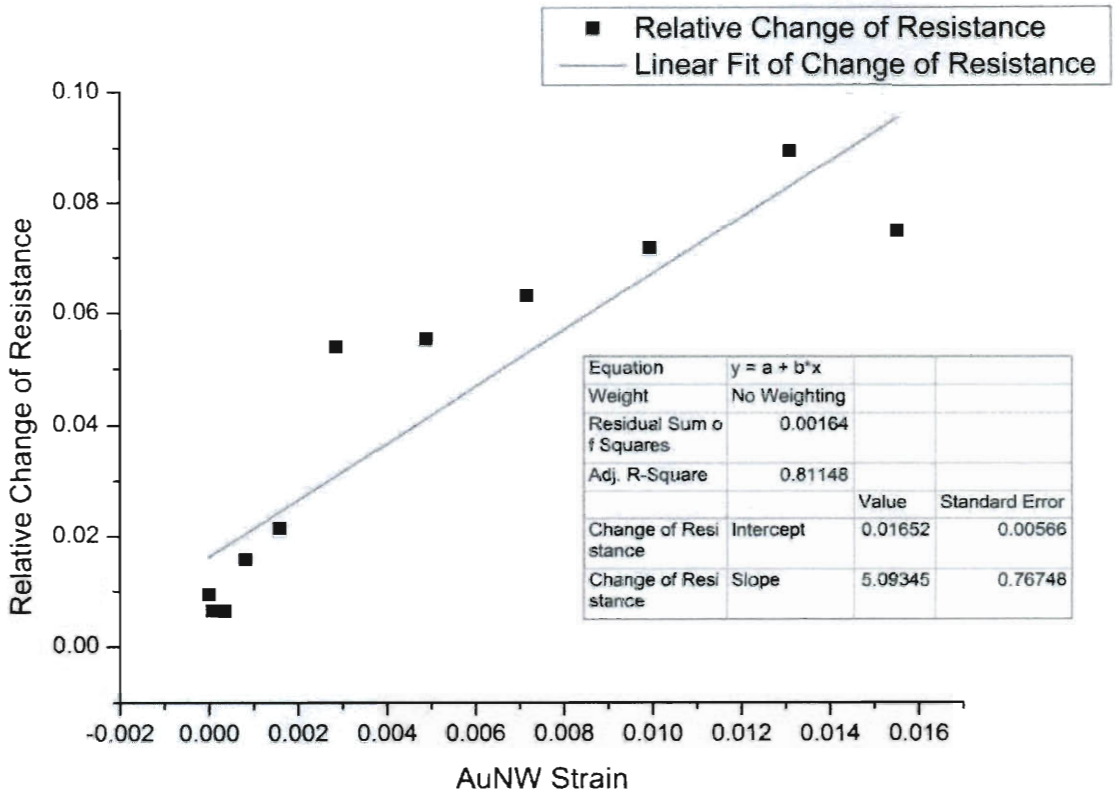

Figure 3-19, Strain in gold nanowire with respect to relative change of resistance

The measured gauge factor for the gold nanowire is $GF = \frac{\Delta R / R}{\varepsilon} = 5.09 \pm 0.77$

Compared with bulk value 4.89[118], the gauge factor for gold nanowire was slightly larger. Considering the diameter of the gold nanowire (50-70nm) was comparable to the mean free path of bulk gold (41nm[119]), electrical properties of the nanowires were expected to be size dependent.

The electrical resistance can be written as $R = \rho \frac{l}{A}$, the strain gauge factor can be written as[120]

$$GF = 1 + 2\mu + \frac{d \ln \rho}{\varepsilon} \tag{3.7}$$

μ is Poisson's ratio, and gold's Poisson ratio is 0.42[118].

From equation(3.7), the gauge factor depends on Poisson's ratio and change of resistivity due to strain. Resistivity of metal originals from two parts, one is electron-phonon scattering, another is scattering with impurities, defects, and grain boundaries and the surface scattering.

To choose a simple conductivity model of the nanowire as the starting point for piezoresistive model, gold nanowires were examined with TEM as shown in Figure 3-20.

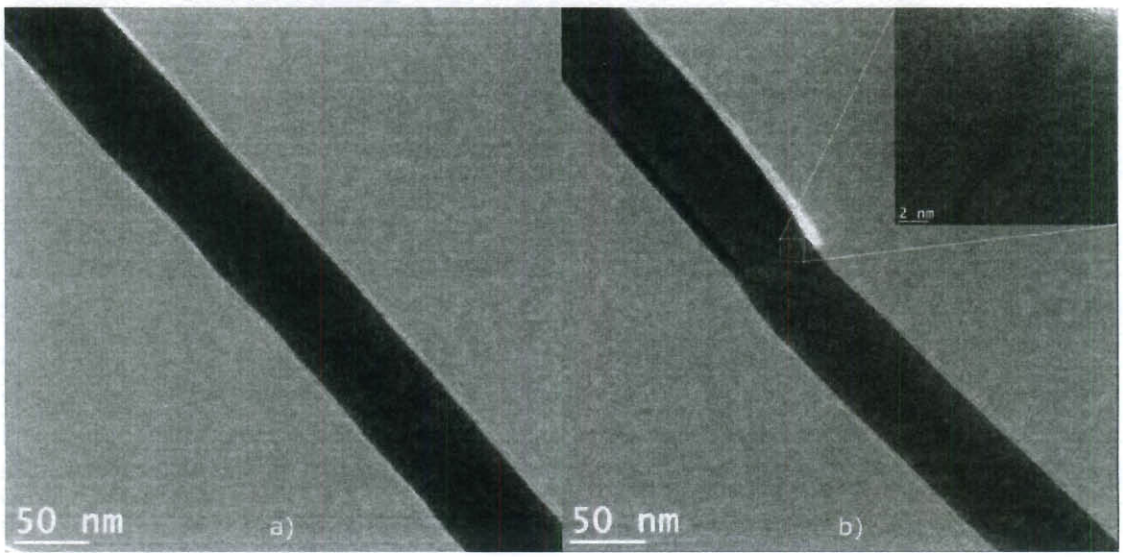

Figure 3-20, TEM images of gold nanowire a) single crystal nanowire with smooth diameter b) a twin boundary with close up image

In Figure 3-20 (a), a single crystal gold nanowire with uniform diameter was shown. Twin boundary could be observed in some nanowires as shown in Figure 3-20 (b). Since most of the nanowires were single crystal with no twin boundary and twin boundary was

believed to has less impact on electrical resistivity[121], twin boundary effect could be safely ignored.

The following assumptions were made based on TEM observation:

1. The gold nanowire is single crystal and thus grain boundary scattering doesn't exist before plastic deformation
2. Electron mean free path of gold nanowire is similar as bulk gold

Thus, the resistivity deviation of the nanowire from bulk gold was purely from surface scattering. And this assumption remains true during elastic deformation. When the gold nanowire was plastically deformed, scattering from defects have to be considered.

The conductivity of a nanowire, due to surface total inelastic scattering, compared with bulk conductivity, can be written as[122-123]

$$f(k) \equiv \frac{\sigma}{\sigma_0} = 1 - \frac{12}{\pi k}\int_0^{\pi/2} d\theta \cos^2\theta \sin^2\theta \left(1 - \int_0^{\pi/2} e^{-k\sin\psi/\sin\theta} \sin\psi d\psi\right) \tag{3.8}$$

And relative size with respect to mean free path $k = 2a/\lambda$, a is radius of the nanowire, and λ is mean free path of electrons. Insert equation (3.8) to (3.7) and note $d\ln\rho = -d\ln\sigma$, then

$$GF = 1 + 2\mu + \frac{d\ln\rho_0}{\varepsilon} + \mu\frac{kf'(k)}{f(k)} \tag{3.9}$$

Thus, the gauge factor for metal nanowire is size dependent given by(3.9).

Use equation(3.9), the size dependent strain gauge effect can be written as

$$\frac{kf'(k)}{f(k)} = \frac{GF_{nano} - GF_{bulk}}{\mu} \tag{3.10}$$

k can be calculated using either (3.10) or its definition. Equation(3.10) gives $k = 1.29$, which agrees with definition $k = \frac{2a}{\lambda} = \frac{50}{41} = 1.22$.

To evaluate magnitude of the size effect, size dependent strain gauge effect with respect to relative size of nanowires was plotted in Figure 3-21.

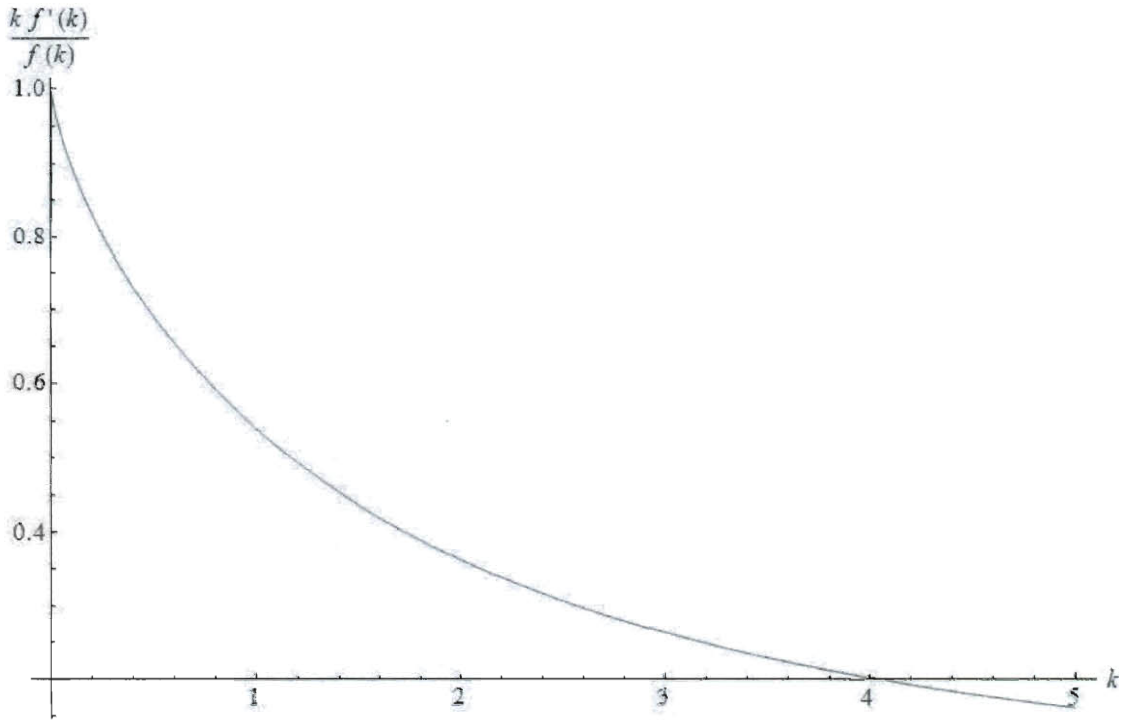

Figure 3-21, size effect of gauge factor

Equation (3.8) assumed all electrons at the surface were inelastically scattered. If elastic scattering is considered and the possibility of elastic reflection is p, the nanowire resistivity and bulk metal resistivity ratio would be [122]

$$\left(\frac{\sigma}{\sigma_0}\right)_{\varepsilon,k} = (1-p)^2 \sum_{1}^{\infty} \left(np^{n-1} \left(\frac{\sigma}{\sigma_0}\right)_{p=0,nk} \right) \tag{3.11}$$

Equation (3.9) would be modified as

$$GF = 1 + 2\mu + \frac{d \ln \rho_0}{\varepsilon} + \mu g(k)$$

$$g(k,p) \equiv \frac{k\sum_{1}^{\infty} n^2 p^{n-1} f'(nk)}{\sum_{1}^{\infty} np^{n-1} f(nk)} \tag{3.12}$$

Numerical calculation of (3.12) indicates summing up to $n = 15$ was sufficient to get accuracy up to 10^{-4}, as indicated in Figure 3-22; larger n was used when p was close to one. The size effect part of the gauge factor $g(k,p)$ with respect to nanowire relative size and elastic reflection coefficient is shown in Figure 3-23. Compared with result without considering elastic reflection shown in Figure 3-21, taking into account of the elastic reflected electrons decreases size dependent part of the strain gauge factor.

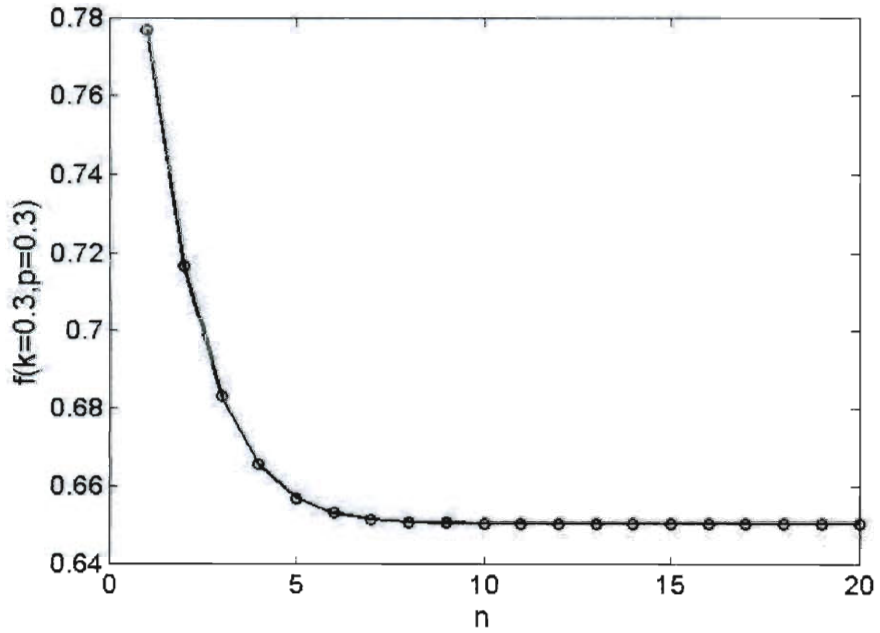

Figure 3-22, approximate(3.11) with more addition terms

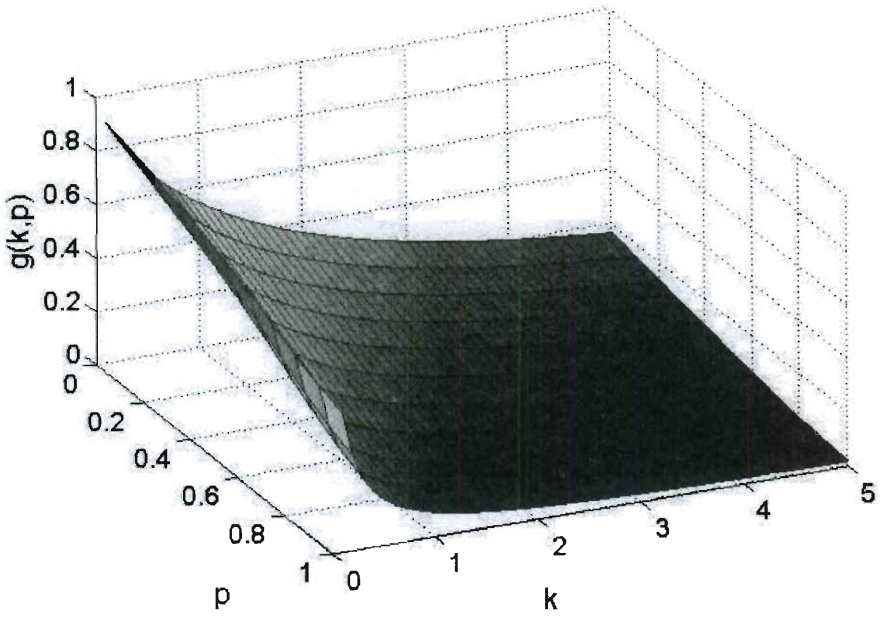

Figure 3-23, effects of relative size (k) and elastic reflection coefficient (p) to size effect of the strain gauge factor $g(k, p)$

Maximum $g(k, p)$ is always smaller than one as seen from Figure 3-23, thus the size dependent strain gauge factor is slightly larger than bulk by $\mu g(k, p) < \mu$. By reducing size, maximum gain of strain gauge factor is $\mu = 0.42$.

Considering elastic scattering, and relative wire size, the elastic reflection parameter is as low as 0.03, which means most of the electrons were inelastically scattered. Reflection parameter p was studied on polycrystalline film samples by measuring electrical conductivity [110, 124-125]. Due to convolution of grain boundary and surface effect, it was difficult to separate surface reflection p from grain boundary reflection and the reported p varied from low p value near zero[126-127] to higher p value 0.12[125]. Use of single crystal gold nanowire eliminates affect of grain boundary. Measuring size

dependent strain gauge factor provides a new alternative method to characterize the elastic reflection coefficient for metal nanomaterials.

3.5 Conclusion

Strain gauge factor of suspended gold nanowire was measured to be slightly larger than bulk gold. This difference could be attributed to size dependent strain gauge effect when material size is comparable to mean free path of electrons. It had been found this size dependent effect for metal was small. By measuring size dependent strain gauge factor of single crystal gold, the elastic reflection coefficient could be measured.

Chapter 4 Mechanical Properties of Few layer Boron Nitride film and Its Application for BN/G NEMS Devices

4.1 Introduction

In Chapter 2 and Chapter 3, it was concluded that gold nanowire may not be good candidate for NEMS resonator operating in liquid. Discovering new materials suitable for oscillating in liquid is important. Recent success in separating single layer graphene from graphite[128] has inspired great scientific interests. Graphene, with its unique electrical properties[129] and ultra strong mechanical strength[130], has demonstrated its use in NEMS devices[12]. Recent discovery that when graphene was placed on boron nitride film, its properties greatly improved compared to silicon dioxide substrate. Graphene and Boron Nitride (BN) could be candidate for future NEMS device building structure. While graphene has been intensively studied, BN is less investigated. Boron Nitride (BN) is a wide band semiconductor with excellent thermal and chemical stability. It has both hexagonal and cubic structure similar to carbon. Hexagonal BN (h-BN) comprises alternative boron and nitride arranged as a honeycomb in two dimensional layers. This honeycomb layers are bonded by weak Van der Waals force. Similar to graphene, few layer h-BN films have been made using mechanical exfoliation[131]. Other methods of making few-layer h-BN include sonication [132-133], electron beam knocking out[134], Reactive ion etching[135], and chemical reaction[136-137]. While

previous obtained films were as large as microns, obtaining a large continuous film would open new gate to study its properties and potential applications.

4.1.1 Mechanical properties testing techniques

It is important to measure BN film's mechanical properties before using it for NEMS building materials. Methods for measuring mechanical properties of nanomaterials have being actively studied. Common techniques include bulge test, beam bending, vibration, nanoindentation and MEMS platform based test.

Bulge test is one of the standard methods[138]. In bulge test, uniform pressure is applied on free standing thin film as shown in Figure 4-1; mechanical deformation of the film is measured and is related to Young's modulus and Poisson's ratio as $H = g(\nu, \frac{b}{a})\left(\frac{qa^4(1-\nu)}{Et}\right)^{1/3}$; a, b, t are geometries shown in Figure 4-1, E is Young's modulus and ν is Poisson's ratio. Bending test of beam structure [97, 139-140] (Figure 4-2) has also been widely used to determine nanomaterials' Young's modulus and strength from the bending force and center displacement. For a cylinder wire, Young's modulus is given by $E = FL^3/192dI$; with L beam length, d wire diameter, and I moment of inertial.

Another method actuates sample into mechanical resonance [34, 90, 141]. Classical beam theory is used to calculate Young's modulus from sample geometry and resonance frequency. Resonant frequency for a beam can be written as $f = \frac{\beta_n^2}{2\pi}\frac{d}{L^2}\sqrt{\frac{E}{16\rho}}$; β_n is a

constant determined by resonance mode, d is diameter of beam, L is beam length, E is Young's modulus, and ρ is density of material.

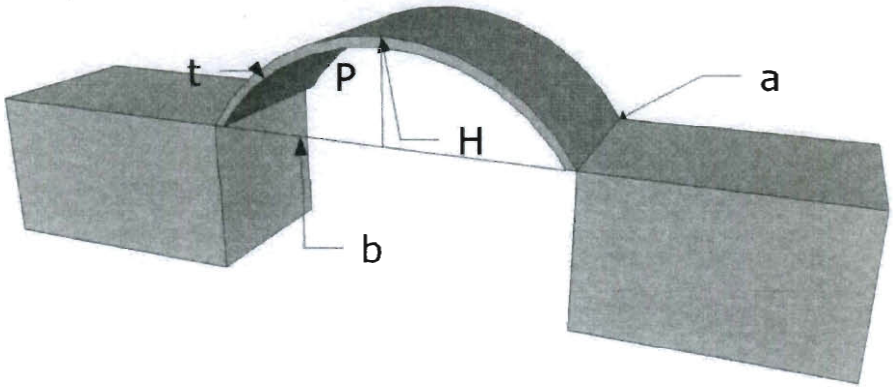

Figure 4-1, Bulge test, uniform pressure is applied on one side of a rectangular film.

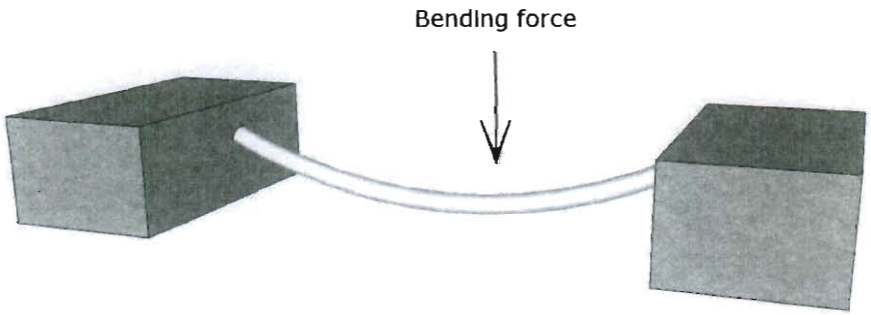

Figure 4-2, beam bending at the center point

In nanoindentation setup, a diamond tip is pressed into sample while force and displacement are recorded. The hardness is given by $H = \frac{F}{A}$, where A is projected area

under indenter and F is applied load. By measuring contact stiffness between sample and tip, which is defined as $S = \frac{\eta F_{\max}}{h_{\max} - h_c}$ ($h_{\max}$ is maximum indentation, $F_{\max}$ is maximum force, h_c is contact depth, and η is a constant); indentation modulus of the sample can be determined. Relationship between contact stiffness and indentation modulus is given by $\frac{\sqrt{\pi}}{2\beta\sqrt{A}} S = \left(\frac{1-\nu^2}{E} + \frac{1-\nu_i^2}{E_i} \right)$, where β is a parameter close to one, $E/(1-\nu^2)$ is indentation modulus of sample and $E_i/(1-\nu_i^2)$ is indenter tip indentation modulus. Mechanical properties measured by nanoindentation are sensitive to substrate material. Generally, the indentation depth should be smaller than 10% of film thickness to exclude substrate effect.

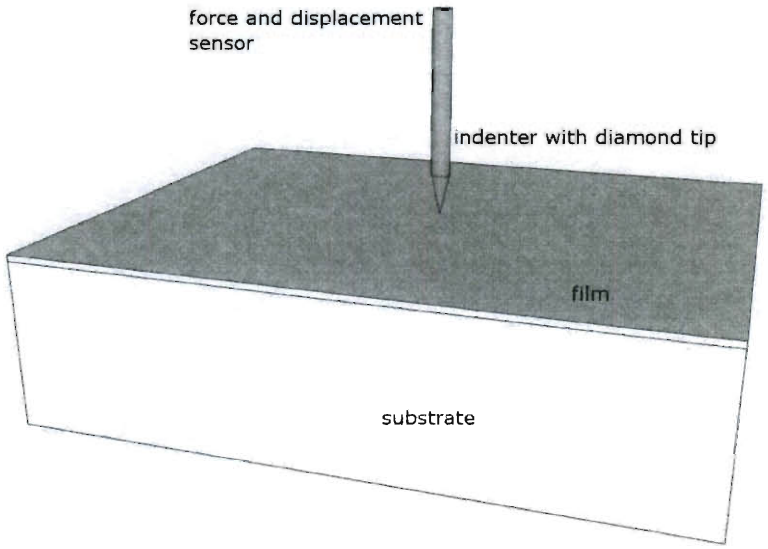

Figure 4-3, nanoindentation with diamond tip

For film with thickness of few nanometers, bulge test [142] and nanoindentation on suspended film[130] have been used. Here, nanoindentation on suspended film with AFM was used.

4.2 Sample preparation

Large scale h-BN film was synthesized based on CVD method on copper film substrate. Detailed synthesis method is available elsewhere [143].

Mechanical properties of the BN film was measured by indenting suspended film over a small hole similar to schematics used to test graphene mechanical properties[130]. Ebeam lithography and RIE were used to create small diameter holes on silicon. Ebeam lithography patterned PMMA was used as RIE mask, recipes that used to anisotropically etch silicon cannot be used because it contains oxygen which will etch PMMA quickly. BN film was transferred from copper foil by spinning coating a PMMA supporting layer. Then the backbone copper foil was dissolved in ferric chloride. After washing with DI water, the floating film was transferred from water to the patterned silicon. When water dried out, sufficient amount of acetone was dropped onto the film to dissolve PMMA, leaving BN film behind. As acetone dried, some part of the BN was suspended over holes as shown in Figure 4-4. That figure also indicates that some part of BN film over holes was broken probably due to surface tension. Corrugation of BN film was observed on silicon substrate; however, for suspended film, no visible corrugation can be found. A smooth film without corrugation before indentation is critical to use indentation technique [144].

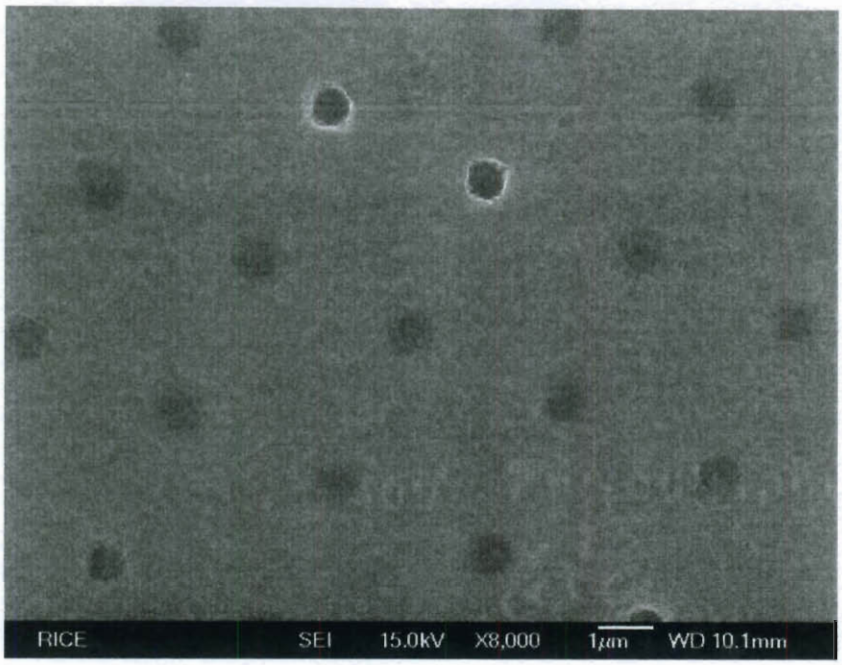

Figure 4-4, BN film covered holes observed in SEM

Continuous film as large as few centimeters was successfully transferred to silicon substrate. AFM topography image shown the thickness of the film was 1nm corresponding to a few atomic layers, which can be verified by Transmission Electron Microscope (TEM)[143].

4.3 Mechanical properties of suspended few layer BN

The suspended BN film was indented with AFM tip as sketched in Figure 4-5. Tapping mode AFM was used to scan the film and identify free standing film. As shown in Figure 4-6, AFM was able to discriminate broken film from continuous film. After a piece of intact film was identified, AFM tip was moved up 100nm away from surface and located above the membrane. AFM feedback loop that maintains constant amplitude at set point

was turned off; and the z piezo voltage was ramped up and drove the tip towards surface of the film, meanwhile, the deflection of the AFM was recorded. Mechanical properties of the BN film could be deduced from the force vs. displacement curve. Initial tests with ordinary silicon tip proved that strength of few layer BN film was stronger than silicon. SEM images of the tip before and after testing are shown in Figure 4-7 and Figure 4-8 respectively. It can be seen that sharp AFM silicon tip were significantly damaged by BN film.

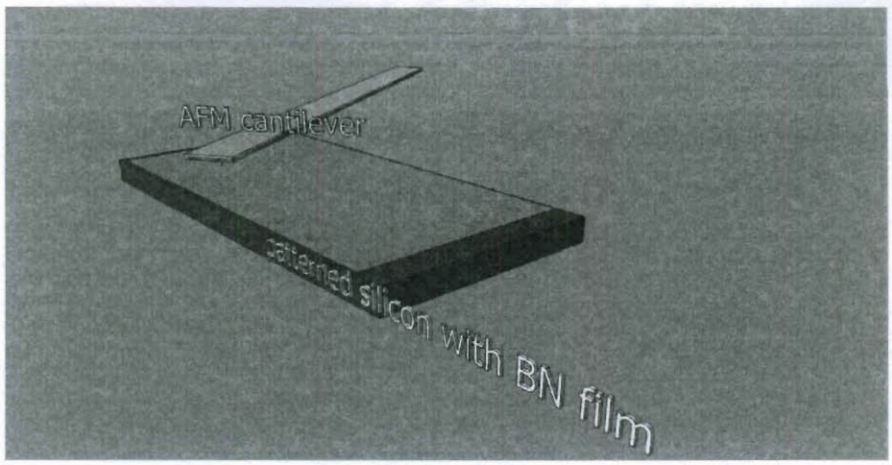

Figure 4-5, schematic of mechanical testing of the BN film with AFM

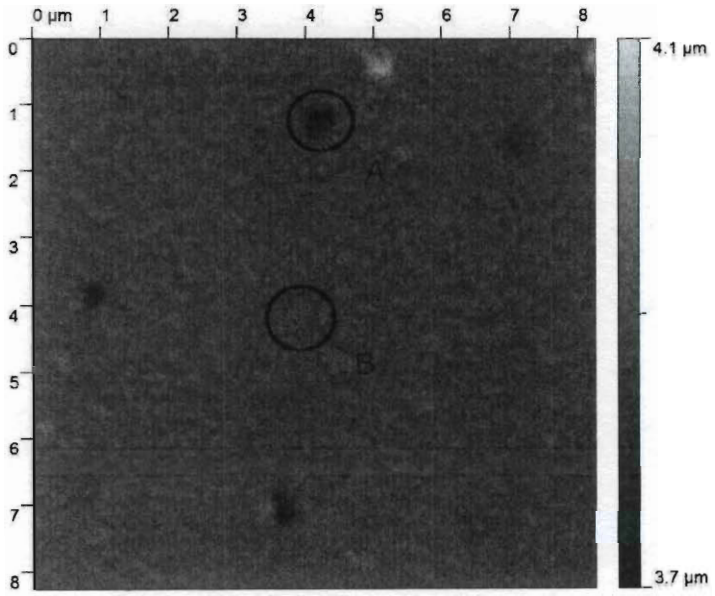

Figure 4-6, AFM topography image of BN film over holes. BN film over hole A is broken, while film over B is intact

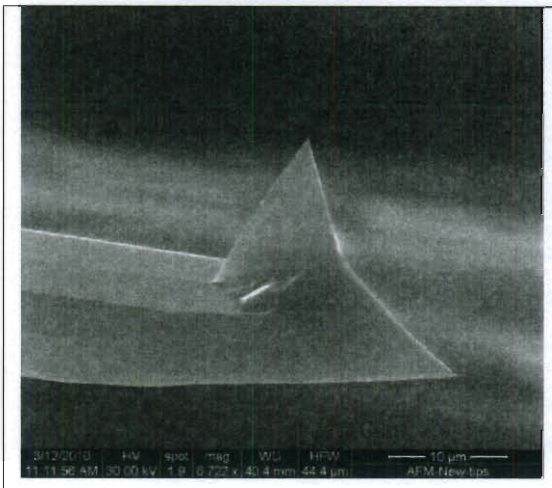

Figure 4-7, silicon AFM tip before indentation

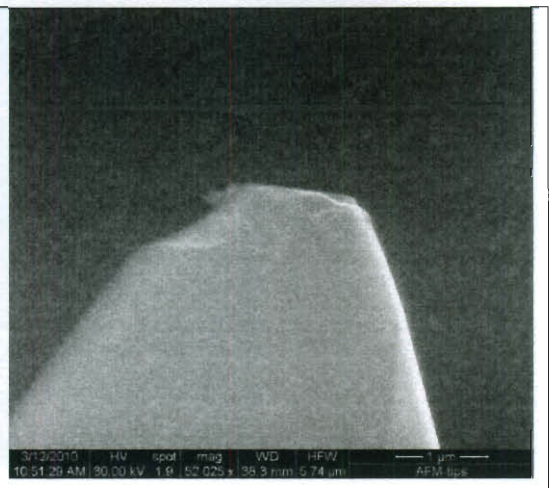

Figure 4-8, silicon AFM tip after indenting BN film, tip was seriously damaged

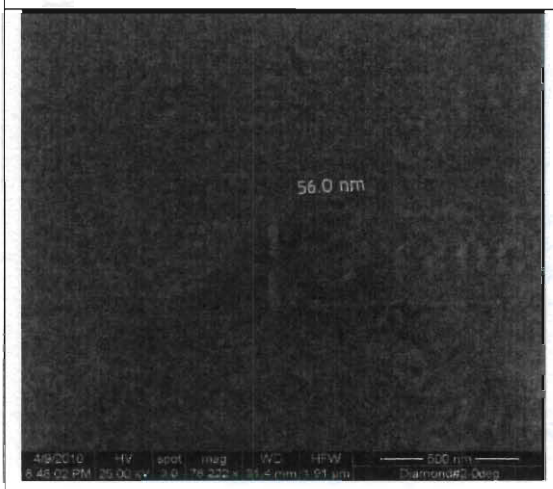

Figure 4-9, diamond tip after indenting BN film

Harder diamond AFM tips[12] were used to prevent tip damage during indentation. Post indentation SEM check (Figure 4-9) found that the very end of tip diameter was about 50nm, larger than render specified diameter (10nm) but still much sharper than damaged silicon tip. Some wear of diamond tip might happen during indentation [145].

---

[12] http://store.nanoscience.com/store/pc/viewCategories.asp?idCategory=157

Suspended BN film was broken by indenting with diamond AFM tip. AFM images of before and after indentation are shown in Figure 4-10.

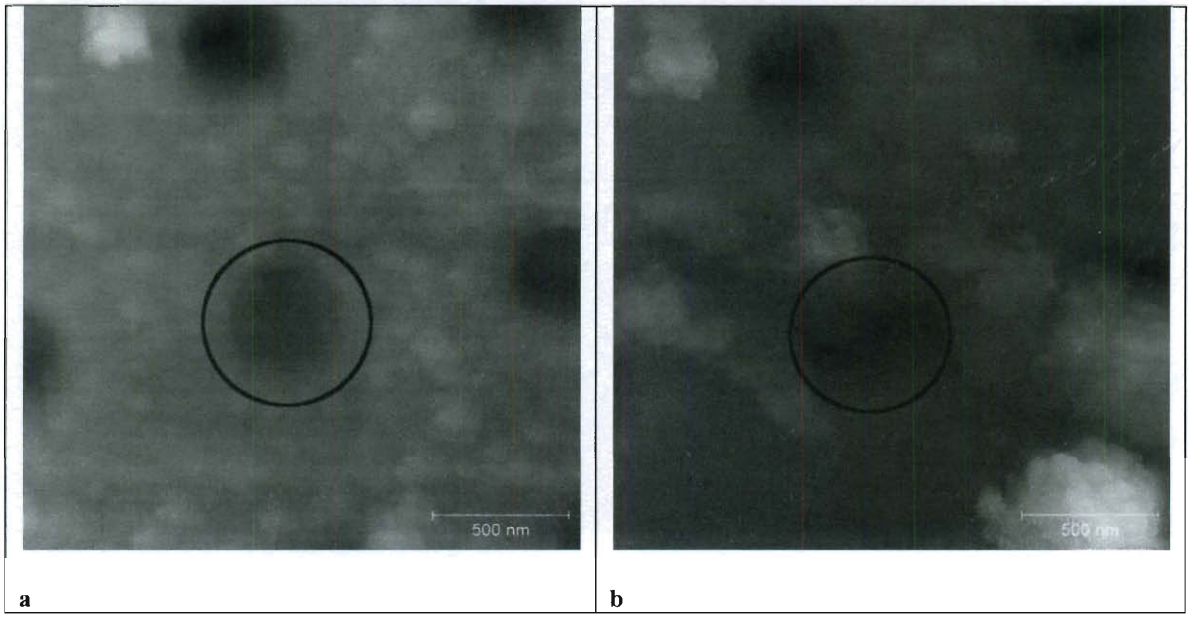

Figure 4-10, AFM images of suspended BN film before (a) and after (b) indentation; some material was plunged out by the AFM tip.

During indentation, AFM cantilever deflection signal and amplitude signal were simultaneously recorded. Both of them came from the photo detector: the amplitude signal is the high frequency part (equals piezo driving frequency in KHz), while the deflection signal is the low frequency part (depends on indentation speed, as low as few Hz). These two parts were separated by filters (low pass for deflection and high pass for amplitude). Just before the AFM probe touches sample surface, amplitude drops from free vibration to zero. From the distance vs. amplitude signal, two parameters could be measured: one is the free vibration amplitude in nanometers, another is the point where probe touches sample. The contact point is defined as when the amplitude of the AFM

cantilever drops to zero. The travel distance of the piezo tube from free oscillation to completely zero amplitude is the free oscillation amplitude measured in nanometers.

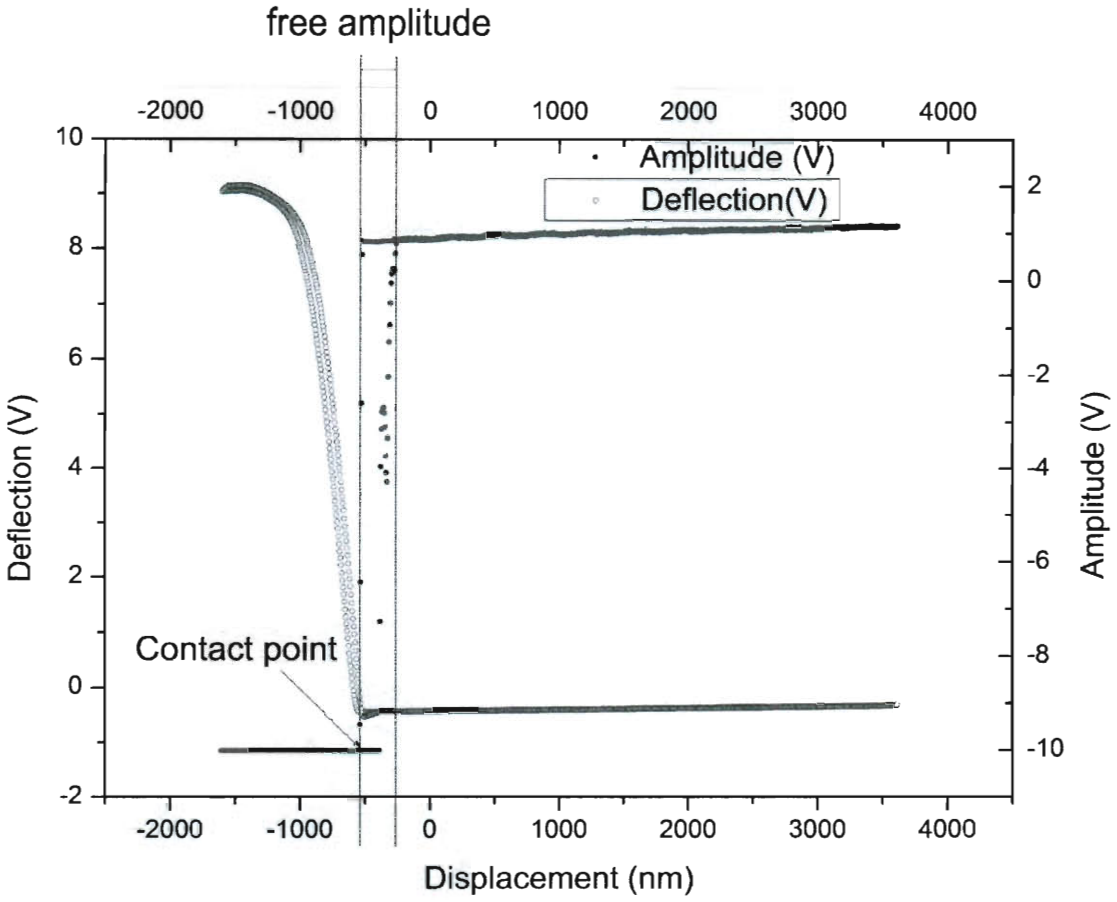

Figure 4-11, Raw cantilever deflection and amplitude vs. displacement data, the contact point between AFM probe and sample is identified; the free amplitude of the cantilever is also known

Once AFM probe contacts with free standing film and keeps on indenting, both the film and the AFM cantilever deform. The total travel displacement of the piezo is sum of deflection from the tip and the film as demonstrated in Figure 4-12. The true center displacement of film was thus calculated by $\delta = D - \Delta$.

Raw displacement vs. deflection data were transformed to indenter load vs. deflection using following steps:

1. Calibration of AFM cantilever deflection, convert unit from volts to nanometer
2. Determine AFM probe spring constant k (by pushing against a known spring constant cantilever[146] or getting excitation response[78]) and calculate indenting force $F = k\Delta$
3. Determine the point where AFM probe in contact with sample and shift origin to this contact point.

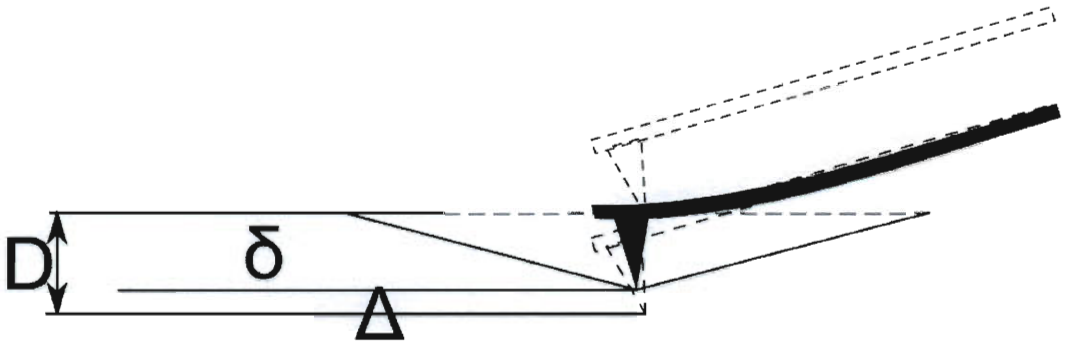

Figure 4-12, Relationship between total piezo tube displacement and film center displacement, AFM cantilever deflection. D is total displacement of piezotube, δ is the center displacement of film and Δ is deflection of AFM cantilever

An indentation vs. displacement curve on suspended BN film was shown in Figure 4-13. Once the AFM tip touches suspended film, force increases nonlinearly with respect to displacement. As the displacement further increased to about 70nm, the force dropped rapidly; which corresponded to penetration of the film.

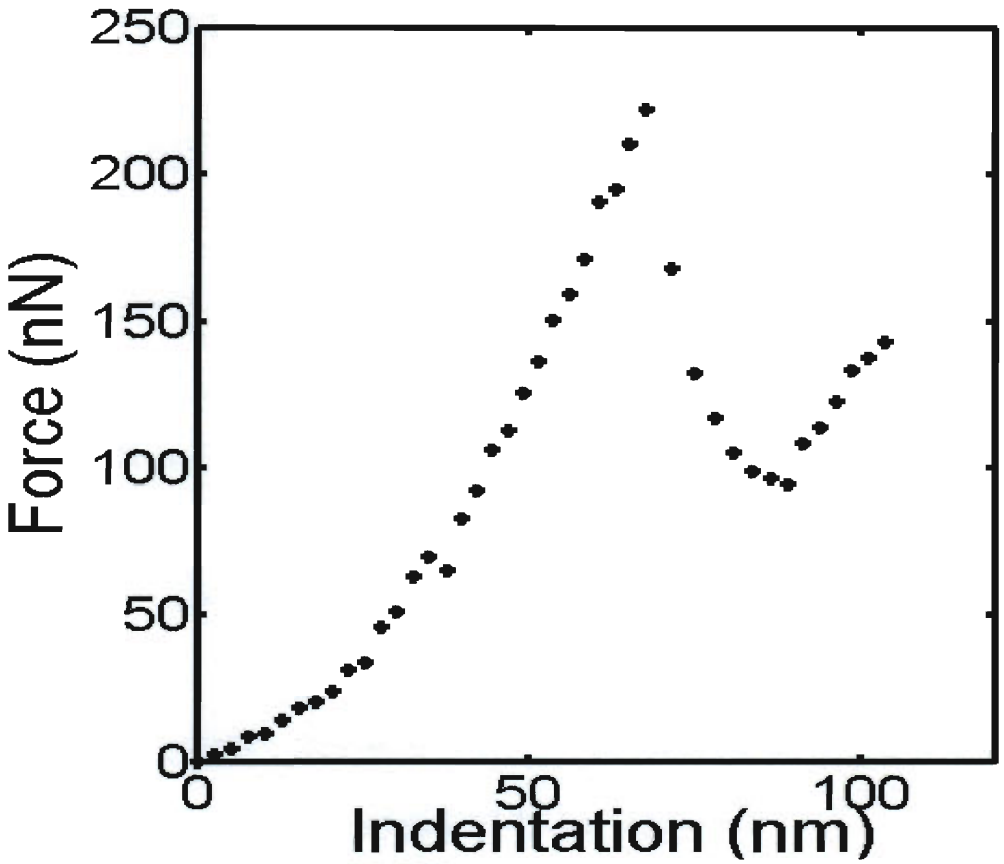

Figure 4-13, force vs. center displacement curve on suspended BN film

Due to relative size of the AFM probe (~50nm) to size of the film (~1um diameter), it cannot be modeled as a point load or a bulge test. Indentation of free suspended BN film is modeled as a sphere indenter displacing a circular thin film as demonstrated in Figure 4-14.

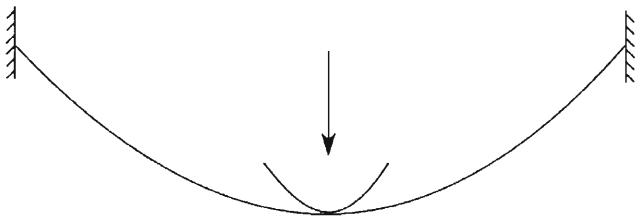

Figure 4-14, a sphere indenter displaces a circular clamped film

The load displacement relationship for the setup given in Figure 4-14 depends on magnitudes of film thickness, deflection, load, prestretch and elastic properties. These parameters determine if the system be modeled as plate, linear membrane or nonlinear membrane. Komaragiri [147] systematically studied and gave regions where different models can be used. In a nutshell, those regions include linear and third order relationship between load and displacement. If prestretch is large compared with load, linear relationship is correct; while in larger load region, third order nonlinear relationship is right. Without prior knowledge of film properties such as prestretch, Young's modulus, it would not be appropriate to determine which region is suitable. However, it was known that the film went from zero loads to disruption by large load; thus the relationship must go from linear region to nonlinear region. To include both regions and the transition region, load displacement relationship is described by combination of linear term and nonlinear term as given by

$$\begin{aligned} F &= Ad + Bd^3 \\ A &= \sigma_0 \pi \\ B &= Ef(v)^3 / a^2 \\ f(v) &= 1/(1.049 - 0.15v - 0.16v^2) \end{aligned} \tag{4.1}$$

Where A and B are fitting parameters, F is load, d is displacement, σ_0 is prestretch, E is two dimensional Young's modulus, $f(v)$ is a correction function fitted from numerical results[147], and v is Poisson's ratio. This form of formula has been adopted by different groups and been numerically verified [130, 148-149]. Two indentations were fitted using equation (4.1) as shown in Figure 4-15.

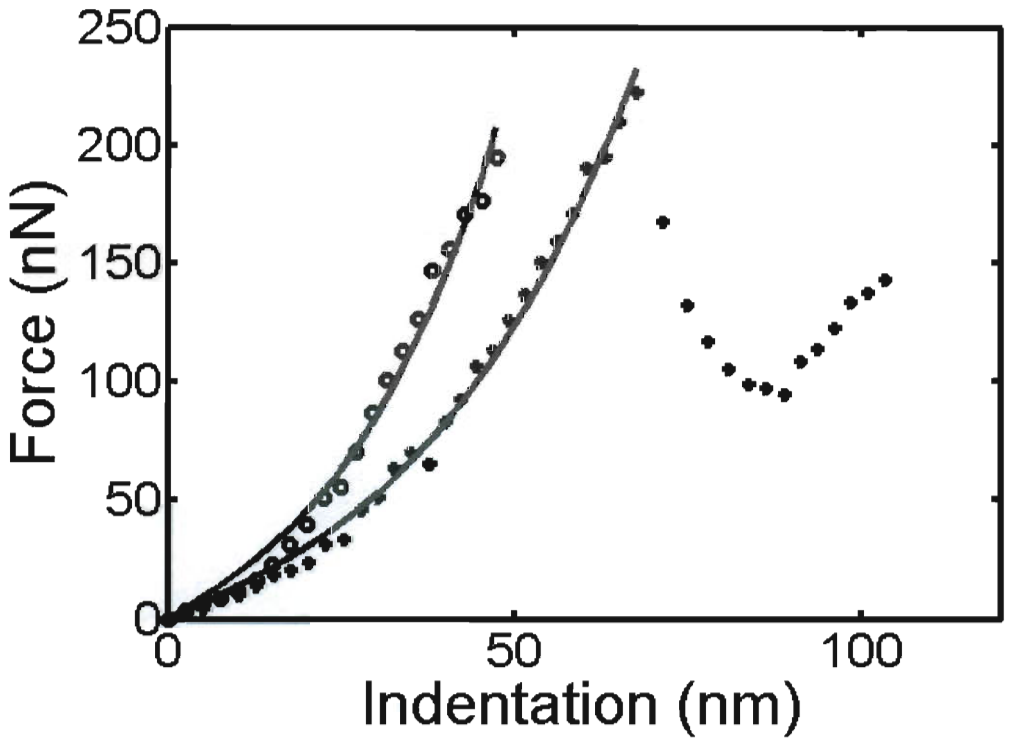

Figure 4-15, Indentation on two films fitting result, dotted points are experiment data, solid curve are fitted result

To calculate 2D Young's modulus, Poisson's ratio and diameter of the hole must be known. Poisson's ratio was assigned as 0.21[150] and diameter of the hole (~1.1um) was measured using SEM after indentation test. Diameter measured by AFM was not used because of errors from convolution of AFM tip with sample[151]. From Figure 4-15,

maximum force applied on the film before breaking is about 221nN. From continuum model, the stress of a circular membrane is given by

$$\sigma_m^{2D} = (FE^{2D} / 4\pi R)^{1/2} \qquad (4.2)$$

F is force applied on the center of the film, E^{2D} is 2D Young's modulus, R is diameter of the diamond tip. If we insert maximum force to equation(4.2), the maximum stress on the film can be deduced.

Calculated two dimensional Young's modulus and maximum stress from three indentations were listed in Table 4-1.

Sample	Thickness (nm)	Possible number of layers	E^{2D} (N/m)	σ_m^{2D} (N/m)
1	2	5	503±30	15.7±1.5
2	1.6	4	431±21	12.8±1.3
3	1.0	2	223±16	8.8±1.2
theoretical	0.33	1	292.1	71.7

Table 4-1, comparison of experimental results and theoretical predictions of different thickness samples' mechanical properties[143].

Obviously, measured Young's modulus and maximum stress are smaller than theoretical predictions. These lower values could be due to defects in CVD grown film.

Sorokin[143] did molecular dynamic simulations to understand effect of defects to the mechanical properties of the film. Simulated indentations of films without defect and with few percentages of defects were performed.

AFM tip was modeled by cone of frozen atoms. The modeled BN sheet has diameter of 14.8nm and the AFM tip's diameter is 1.63nm. A dynamic fracture of BN film under indentation is shown in Figure 4-16. Defects play an important role in reducing Young's modulus and maximum stress in BN film. The Young's modulus E^{2D} and maximum stress σ_m^{2D} decrease linearly with respect to defects concentration.

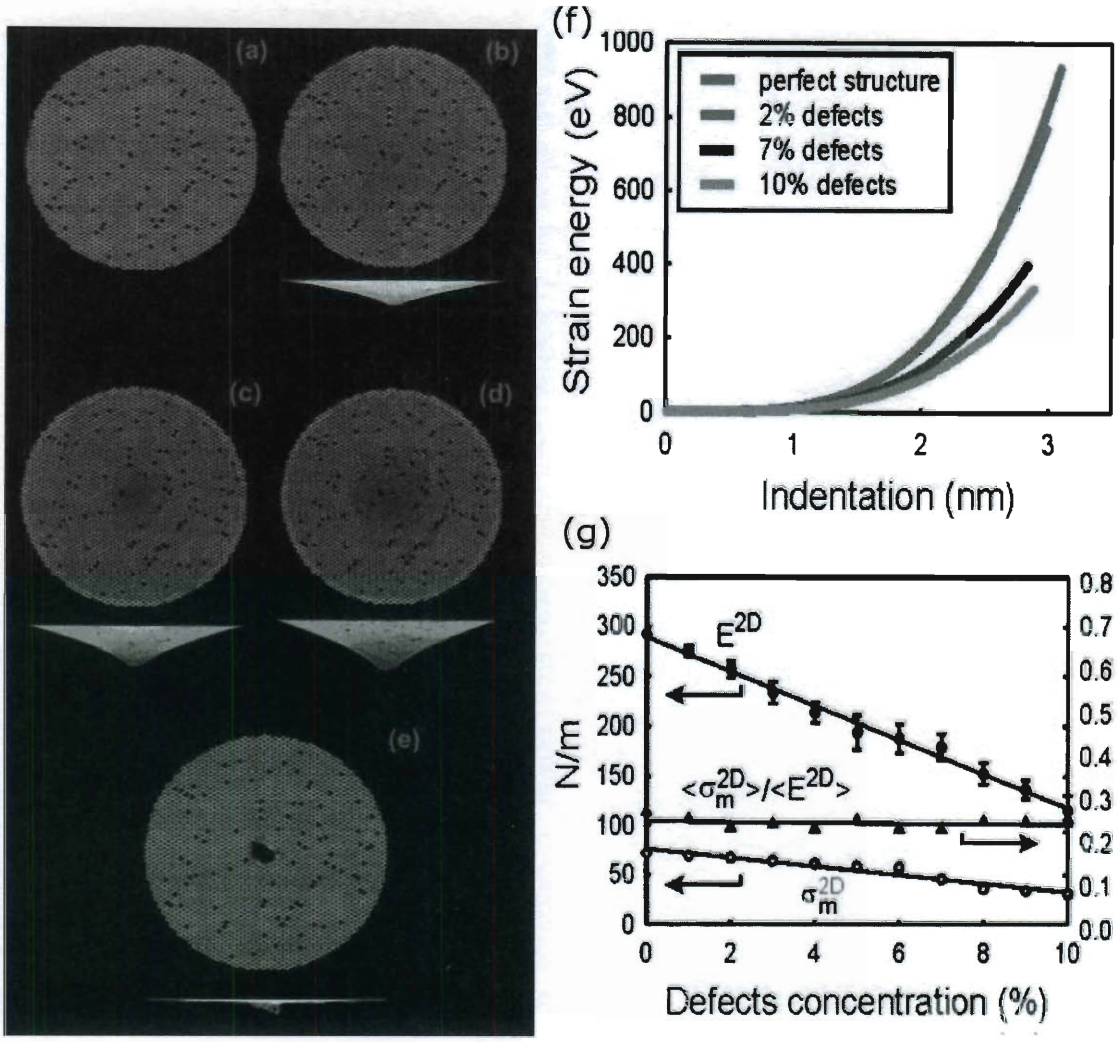

Figure 4-16, Indentation of BN film with 2% defects a) no deflection b) $\delta = 15\text{Å}$ c) $\delta = 25\text{Å}$ d) $\delta = 31\text{Å}$ d) fractured film. Bond length represented by color gradient shown in the bottom of each figure with red ($1.61-1.75\text{Å}$) and yellow ($1.44-1.46\text{Å}$) f) Strain energy with respect to indentation at different deflects level, with increasing defect population, strain energy drops at same indentation. (g) Young's modulus and maximum strain decreases with increasing defects concentration.[143]

4.4 Conclusion

Large scale of atomically thin BN films were grown with CVD method. Their mechanical properties were investigated using AFM indentation techniques. The experimental measured lower Young's modulus and maximum stress were attributed to defects in the film. Molecular dynamic studies confirmed our hypothesis that introduction of defects reduced BN film mechanical properties.

Chapter 5 Summary and future work

5.1 Summaries

In first part of the thesis, sensitivity of NEMS sensors was discussed from nonlinear fitting statistics consideration and best operation range was identified for two different measurements schematics. Physical model of single end clamped NEMS beam in liquid was built and mass sensitivity of the device was discussed. Suspended gold nanowire devices were magnetomotively actuated in vacuum and silicon oil and compared.

In the second part, the strain gauge effect of gold nanowire was measured. Model for calculating size effect of this electromechanical property of metals was built and compared with experimental measurement of gold nanowires. Both experiment result and model predict low size effect of strain gauge factor for metal. This low size effect of strain gauge factor with metal justifies use of bulk electromechanical properties for metal in nanomaterials.

In the third part, mechanical properties of novel two dimensional boron nitride films were measured using AFM indentation technique. Measured low breaking strength was attributed to the defects in the boron nitride films. Understanding the mechanical properties of few atomic layers thin boron nitride films lay down the road for future application of boron nitride in NEMS devices.

5.2 Suggested Future work

The NEMS resonator is highly damped in fluid, the low Q factor and significantly reduced resonance frequency lead to low mass sensitivity according to frequency domain measurement technique. As predicted in 2.2.3, switch to time domain measurement may reduce uncertainty and achieve better mass resolution. Calculation of sensitivity in time domain will complete theory of sensitivity limit of NEMS sensors. Further experiments are required to support our theories.

Size dependent strain gauge factor of metal nanomaterials have not been systematically studied. While the theory provided in this thesis considered size effect mainly in a semiclassical model, the possible size-dependent electron-phonon interaction has not been considered. It has been predicted that strain causes phonon spectral redistribution in atomic gold nanowires [152-153], however, no theory available about phonon behavior in the mesoscopic scale. It would be interesting to systematically study size dependent piezoresistance in mesoscopic metals.

Finally, characterization of mechanical properties of atomic layer BN film is the first step to explore the possibility of using it as future building block of NEMS devices. More characterization such as its dielectric constant, its compatibility with graphene requires a lot of continuous work of succeeding researchers.

Bibliography

1. Burg, T.P., et al., *Weighing of biomolecules, single cells and single nanoparticles in fluid.* nature, 2007. **446**: p. 1066.
2. Yang, Y.T., et al., *Zeptogram-Scale Nanomechanical Mass Sensing.* Nano Letters, 2006. **6**(4): p. 583-586.
3. Huang, H., et al., *Semiconductor gas sensor based on tin oxide nanorods prepared by plasma-enhanced chemical vapor deposition with postplasma treatment.* Appl.Phys.Lett., 2005. **87**: p. 163123.
4. Stampfer, C., A. Jungen, and C. Hierold, *Fabrication of Discrete Nanoscaled Force Sensors Based on Single-Walled Carbon Nanotubes.* IEEE sensor J., 2006. **6**: p. 613.
5. Svitelskiy, O., et al., *Pressurized Fluid Damping of Nanoelectromechanical Systems.* Phys. Rev. Lett., 2009. **103**(24): p. 244501.
6. Sawano, S., T. Arie, and S. Akita, *Carbon Nanotube Resonator in Liquid.* Nano Letters. **0**(0).
7. Tough, J.T., W.D. McCormick, and J.G. Dash, *Vibrating Wire Viscometer.* Review of Scientific Instruments, 1964. **35**(10): p. 1345-1348.
8. Burkhalter, R.L., Torrance, and C.W. Kayser, *Piezoelectric pressure transducer.* 1966.
9. Davis, Z.J. and A. Boisen, *Aluminum nanocantilevers for high sensitivity mass sensors.* Applied Physics Letters, 2005. **87**(1): p. 013102.
10. Huang, X.M.H., et al., *VHF, UHF and microwave frequency nanomechanical resonators.* New Journal of Physics, 2005. **7**(1): p. 247.
11. Xu, Y.-Q., A. Barnard, and P.L. McEuen, *Bending and Twisting of Suspended Single-Walled Carbon Nanotubes in Solution.* Nano Letters, 2009. **9**(4): p. 1609-1614.
12. Bunch, J.S., et al., *Electromechanical Resonators from Graphene Sheets.* Science, 2007. **315**(5811): p. 490-493.
13. Sekaric, L., et al., *Operation of nanomechanical resonant structures in air.* Applied Physics Letters, 2002. **81**(14): p. 2641-2643.
14. Rinaldi, M., C. Zuniga, and G. Piazza. *5-10 GHz AlN Contour-Mode Nanoelectromechanical Resonators.* in *Micro Electro Mechanical Systems, 2009. MEMS 2009. IEEE 22nd International Conference on.*
15. Olsson, P.A.T., H.S. Park, and P.C. Lidstrom, *The Influence of shearing and rotary inertia on the resonant properties of gold nanowires.* Journal of Applied Physics, 2010. **108**(10): p. 104312.
16. Husain, A., et al., *Nanowire-based very-high-frequency electromechanical resonator.* Appl. Phys. Lett., 2003. **83**: p. 1240.
17. Cimalla, V., et al., *Pulsed mode operation of strained microelectromechanical resonators in air.* Applied Physics Letters, 2006. **88**(25): p. 253501.

18. Verbridge, S.S., et al., *High quality factor resonance at room temperature with nanostrings under high tensile stress.* Journal of Applied Physics, 2006. **99**(12): p. 124304.
19. Unterreithmeier, Q.P., T. Faust, and J.r.P. Kotthaus, *Damping of Nanomechanical Resonators.* Phys. Rev. Lett., 2010. **105**(2): p. 027205.
20. Kozinsky, I., et al., *Tuning nonlinearity, dynamic range, and frequency of nanomechanical resonators.* Appl. Phys. Lett., 2006. **88**: p. 253101.
21. Dai, M.D., K. Eom, and C.-W. Kim, *Nanomechanical mass detection using nonlinear oscillations.* Applied Physics Letters, 2009. **95**(20): p. 203104.
22. Postma, H.W.C., et al., *Dynamic range of nanotube- and nanowire-based electromechanical systems.* Applied Physics Letters, 2005. **86**(22): p. 223105.
23. Dohn, S., et al., *Mass and position determination of attached particles on cantilever based mass sensors.* Review of Scientific Instruments, 2007. **78**(10): p. 103303.
24. Sader, J.E., *Frequency response of cantilever beams immersed in viscous fluids with applications to the atomic force microscope.* Journal of Applied Physics, 1998. **84**(1): p. 64-76.
25. Eysden, C.A.V. and J.E. Sader, *Resonant frequencies of a rectangular cantilever beam immersed in a fluid.* Journal of Applied Physics, 2006. **100**(11): p. 114916.
26. Ilic, B., et al., *Attogram detection using nanoelectromechanical oscillators.* Journal of Applied Physics, 2004. **95**(7): p. 3694-3703.
27. Kim, K., K. Jensen, and A. Zettl, *Tuning Nanoelectromechanical Resonators with Mass Migration.* Nano Letters, 2009. **9**(9): p. 3209-3213.
28. Wang, S.-C., et al., *Resonance frequency shift of a carbon nanotube with a silver nanoparticle adsorbed at various positions.* Applied Physics Letters, 2010. **97**(13): p. 133105.
29. Dohn, S., et al., *Position and mass determination of multiple particles using cantilever based mass sensors.* Applied Physics Letters, 2010. **97**(4): p. 044103.
30. Cleland, A.N. and M.L. Roukes, *Fabrication of high frequency nanometer scale mechanical resonators from bulk Si crystals.* Applied Physics Letters, 1996. **69**(18): p. 2653-2655.
31. Yang, Y.T., et al., *Monocrystalline silicon carbide nanoelectromechanical systems.* Applied Physics Letters, 2001. **78**(2): p. 162-164.
32. Olkhovets, A., et al. *Actuation and internal friction of torsional nanomechanical silicon resonators*: AVS.
33. Yum, K., et al., *Experimental measurement and model analysis of damping effect in nanoscale mechanical beam resonators in air.* Journal of Applied Physics, 2004. **96**(7): p. 3933-3938.
34. Suryavanshi, A.P., et al., *Elastic modulus and resonance behavior of boron nitride nanotubes.* Applied Physics Letters, 2004. **84**(14): p. 2527-2529.
35. Poncharal, P., et al., *Electrostatic Deflections and Electromechanical Resonances of Carbon Nanotubes.* Science, 1999. **283**(5407): p. 1513-1516.
36. Ekinci, K., *Electromechanical Transducers at the Nanoscale: Actuation and Sensing of Motion in Nanoelectromechanical Systems (NEMS).* Small, 2005. **1**(8-9): p. 786-797.

37. Sawano, S., T. Arie, and S. Akita, *Carbon Nanotube Resonator in Liquid.* Nano Letters, 2010. **10**(9): p. 3395-3398.
38. Sadek, A.S., et al., *Wiring Nanoscale Biosensors with Piezoelectric Nanomechanical Resonators.* Nano Letters, 2010. **10**(5): p. 1769-1773.
39. Sinha, N., et al., *Piezoelectric aluminum nitride nanoelectromechanical actuators.* Applied Physics Letters, 2009. **95**(5): p. 053106.
40. Padua, A.A.H., et al., *Electromechanical model for vibrating-wire instruments.* Review of Scientific Instruments, 1998. **69**(6): p. 2392-2399.
41. Cleland, A.N. and M.L. Roukes, *External control of dissipation in a nanometer-scale radiofrequency mechanical resonator.* Sensors and Actuators A: Physical, 1999. **72**(3): p. 256-261.
42. Li, T.F., et al., *High-frequency metallic nanomechanical resonators.* Applied Physics Letters, 2008. **92**(4): p. 043112.
43. Ekinci, K.L., et al., *Balanced electronic detection of displacement in nanoelectromechanical systems.* Appl. Phys. Lett., 2002. **81**: p. 2253.
44. Cross, J.D., et al., *Piezoresistive transduction in multilayer polycrystalline silicon resonators.* Applied Physics Letters, 2009. **95**(13): p. 133113.
45. Bargatin, I., et al., *Sensitive detection of nanomechanical motion using piezoresistive signal downmixing.* Applied Physics Letters, 2005. **86**(13): p. 133109.
46. Li, M., T. X, and R. L, *Ultra-sensitive NEMS-based cantilevers for sensing, scanned probe and very high-frequency applications.* Nat Nano, 2007. **2**(2): p. 114-120.
47. Jiang, Y., T. Ono, and M. Esashi, *Temperature-dependent mechanical and electrical properties of boron-doped piezoresistive nanocantilevers.* Journal of Micromechanics and Microengineering, 2009. **19**(6): p. 065030.
48. Jiang, Y.G., T. Ono, and M. Esashi, *Fabrication of piezoresistive nanocantilevers for ultra-sensitive force detection.* Measurement Science and Technology, 2008. **19**(8): p. 084011.
49. Belov, M., et al., *Mechanical resonance of clamped silicon nanowires measured by optical interferometry.* Journal of Applied Physics, 2008. **103**(7): p. 074304.
50. Karabacak, D., T. Kouh, and K.L. Ekinci, *Analysis of optical interferometric displacement detection in nanoelectromechanical systems.* Journal of Applied Physics, 2005. **98**(12): p. 124309.
51. LiuN, et al., *Time-domain control of ultrahigh-frequency nanomechanical systems.* Nat Nano, 2008. **3**(12): p. 715-719.
52. Kouh, T., et al., *Diffraction effects in optical interferometric displacement detection in nanoelectromechanical systems.* Applied Physics Letters, 2005. **86**(1): p. 013106.
53. Sanii, B. and P.D. Ashby, *High Sensitivity Deflection Detection of Nanowires.* Phys. Rev. Lett., 2010. **104**(14): p. 147203.
54. Ilic, B., et al., *Dynamic characterization of nanoelectromechanical oscillators by atomic force microscopy.* Journal of Applied Physics, 2007. **101**(4): p. 044308-9.
55. Garcia-Sanchez, D., et al., *Imaging Mechanical Vibrations in Suspended Graphene Sheets.* Nano Letters, 2008. **8**(5): p. 1399-1403.

56. Feng, X.L., et al., *A self-sustaining ultrahigh-frequency nanoelectromechanical oscillator.* nature nanotechnology, 2008. **3**: p. 342.
57. Weldon, J.A., et al., *Sustained Mechanical Self-Oscillations in Carbon Nanotubes.* Nano Letters, 2010. **10**(5): p. 1728-1733.
58. Lazarus, A., et al., *Simple modeling of self-oscillations in nanoelectromechanical systems.* Applied Physics Letters, 2010. **96**(19): p. 193114.
59. Ekinci, K.L., Y.T. Yang, and M.L. Roukes, *Ultimate limits to inertial mass sensing based upon nanoelectromechanical systems.* Journal of Applied Physics, 2004. **95**(5): p. 2682-2689.
60. Lifshitz, R., *Phonon-mediated dissipation in micro- and nano-mechanical systems.* Physica B: Condensed Matter, 2002. **316-317**: p. 397-399.
61. Zener, C., *Internal Friction in Solids. I. Theory of Internal Friction in Reeds.* Phys. Rev., 1937. **52**(3): p. 230-235.
62. Zener, C., *Internal Friction in Solids II. General Theory of Thermoelastic Internal Friction.* Phys. Rev., 1938. **53**(1): p. 90-99.
63. Lifshitz, R. and M.L. Roukes, *Thermoelastic damping in micro- and nanomechanical systems.* Phys. Rev. B, 2000. **61**(8): p. 5600-5609.
64. Hopcroft, M.A., et al., *Using the temperature dependence of resonator quality factor as a thermometer.* Applied Physics Letters, 2007. **91**(1): p. 013505.
65. Woodruff, T.O. and H. Ehrenreich, *Absorption of Sound in Insulators.* Phys. Rev., 1961. **123**(5): p. 1553-1559.
66. Hao, Z., A. Erbil, and F. Ayazi, *An analytical model for support loss in micromachined beam resonators with in-plane flexural vibrations.* Sensors and Actuators A: Physical, 2003. **109**(1-2): p. 156-164.
67. Photiadis, D.M. and J.A. Judge, *Attachment losses of high Q oscillators.* Applied Physics Letters, 2004. **85**(3): p. 482-484.
68. R.E, M. and M. N.C, *Dissipation measurements of vacuum-operated single-crystal silicon microresonators.* Sensors and Actuators A: Physical, 1995. **50**: p. 199-207(9).
69. Liu, X., et al., *A loss mechanism study of a very high Q silicon micromechanical oscillator.* Journal of Applied Physics, 2005. **97**(2): p. 023524.
70. Yasumura, K.Y., et al., *Quality factors in micron- and submicron-thick cantilevers.* Microelectromechanical Systems, Journal of, 2000. **9**(1): p. 117-125.
71. Henry, J.A., Y. Wang, and M.A. Hines, *Controlling energy dissipation and stability of micromechanical silicon resonators with self-assembled monolayers.* Applied Physics Letters, 2004. **84**(10): p. 1765-1767.
72. Bhiladvala, R.B. and Z.J. Wang, *Effect of fluids on the Q factor and resonance frequency of oscillating micrometer and nanometer scale beams.* Phys. Rev. E, 2004. **69**(3): p. 036307.
73. Vignola, J.F. and J.A. Judge, *Architectural considerations of micro- and sensor/nanoresonators for mass detection in the presence of a fluid.* Journal of Applied Physics, 2008. **104**(12): p. 124305.
74. Martin, M.J. and B.H. Houston, *Gas damping of carbon nanotube oscillators.* Appl. Phys. Lett., 2007. **91**: p. 103116.

75. Yakhot, V. and C. Colosqui, *Stokes' second flow problem in a high-frequency limit: application to nanomechanical resonators.* Journal of Fluid Mechanics, 2007. **586**(-1): p. 249-258.
76. Eysden, C.A.V. and J.E. Sader, *Frequency response of cantilever beams immersed in viscous fluids with applications to the atomic force microscope: Arbitrary mode order.* Journal of Applied Physics, 2007. **101**(4): p. 044908.
77. Green, C.P. and J.E. Sader, *Frequency response of cantilever beams immersed in viscous fluids near a solid surface with applications to the atomic force microscope.* Journal of Applied Physics, 2005. **98**(11): p. 114913.
78. Sader, J.E., J.W.M. Chon, and P. Mulvaney, *Calibration of rectangular atomic force microscope cantilevers.* Rev. Sci. Instrum., 1999. **70**(10): p. 3967-3969.
79. Sader, J.E. and S.P. Jarvis, *Accurate formulas for interaction force and energy in frequecy modulation force spectroscopy.* Appl. Phys. Lett., 2004. **84**: p. 1801.
80. Sazonova, V., et al., *A tunable carbon nanotube electromechanical oscillator.* nature, 2004. **431**: p. 284.
81. Lavrik, N.V. and P.G. Datskos, *Femtogram mass detection using photothermally actuated nanomechanical resonators.* Applied Physics Letters, 2003. **82**(16): p. 2697-2699.
82. Peng, H.B., et al., *Ultrahigh Frequency Nanotube Resonators.* Physical Review Letters, 2006. **97**(8): p. 087203.
83. Judge, J.A., J.F. Vignola, and J. Jarzynski, *Dissipation from microscale and nanoscale beam resonators into a surrounding fluid.* Applied Physics Letters, 2008. **92**(12): p. 124102.
84. Aster, R., B. Borchers, and C. Thurber, *Parameter Estimation and Inverse Problems (International Geophysics).* 2005: Academic Press.
85. Brueckner, K., et al., *Strain- and pressure-dependent RF response of microelectromechanical resonators for sensing applications.* Journal of Micromechanics and Microengineering, 2007. **17**(10): p. 2016.
86. Feng, X.L., et al., *Very High Frequency Silicon Nanowire Electromechanical Resonators.* Nano Letters, 2007. 7(7): p. 1953-1959.
87. Svitelskiy, O., et al., *A simple cell for the analysis of nanoelectromechanical systems under gas pressure.* Review of Scientific Instruments, 2008. **79**(9): p. 093701.
88. Chen, G.Y., et al., *Resonance response of scanning force microscopy cantilevers.* Review of Scientific Instruments, 1994. **65**(8): p. 2532-2537.
89. Riesch, C., et al., *Characterizing Vibrating Cantilevers for Liquid Viscosity and Density Sensing.* Journal of Sensors, 2008. **2008**: p. 697062.
90. Dikin, D.A., et al., *Resonance vibration of amorphous SiO[sub 2] nanowires driven by mechanical or electrical field excitation.* Journal of Applied Physics, 2003. **93**(1): p. 226-230.
91. Chon, J.W.M., P. Mulvaney, and J.E. Sader, *Experimental validation of theoretical models for the frequency response of atomic force microscope cantilever beams immersed in fluids.* Journal of Applied Physics, 2000. **87**(8): p. 3978-3988.

92. Green, C.P., et al., *Normal and torsional spring constants of atomic force microscope cantilevers.* Rev. Sci. Instrum., 2004. **75**(6): p. 1988-1996.
93. Basak, S., A. Raman, and S.V. Garimella, *Hydrodynamic loading of microcantilevers vibrating in viscous fluids.* Journal of Applied Physics, 2006. **99**(11): p. 114906.
94. Elmer, F.-J. and M. Dreier, *Eigenfrequencies of a rectangular atomic force microscope cantilever in a medium.* Journal of Applied Physics, 1997. **81**(12): p. 7709-7714.
95. Blevins, R.D., *Formulas for Natural Frequency and Mode Shape*. 1979: Litton Educational Pbulishing. 108.
96. Xu, X. and A. Raman, *Comparative dynamics of magnetically, acoustically, and Brownian motion driven microcantilevers in liquids.* Journal of Applied Physics, 2007. **102**(3): p. 034303.
97. Wu, B., A. Heidelberg, and J.J. Boland, *Mechanical properties of ultrahigh-strength gold nanowires.* Nat Mater, 2005. **4**(7): p. 525-529.
98. Sahin, O., et al., *High-resolution imaging of elastic properties using harmonic cantilevers.* Sensors and Actuators A: Physical, 2004. **114**(2-3): p. 183-190.
99. Yong P. Chen, L.A.J., Hao Lu, Jun Lou. 2010, MRS.
100. Hall, A.R., et al., *Electromechanical response of single-walled carbon nanotubes to torsional strain in a self-contained device.* Nat Nano, 2007. **2**(7): p. 413-416.
101. Li, C.-Y. and T.-W. Chou, *Strain and pressure sensing using single-walled carbon nanotubes.* Nanotechnology, 2004. **15**(11): p. 1493-1496.
102. Chang, N.-K., C.-C. Su, and S.-H. Chang, *Fabrication of single-walled carbon nanotube flexible strain sensors with high sensitivity.* Applied Physics Letters, 2008. **92**(6): p. 063501.
103. Minot, E.D., et al., *Tuning Carbon Nanotube Band Gaps with Strain.* Phys. Rev. Lett., 2003. **90**: p. 156401-1.
104. Zhou, J., et al., *Flexible Piezotronic Strain Sensor.* Nano Letters, 2008. **8**(9): p. 3035-3040.
105. He, R. and P. Yang, *Giant piezoresistance effect in silicon nanowires.* Nat Nano, 2006. **1**(1): p. 42-46.
106. Williams, K.R. and R.S. Muller, *Etch Rates for Micromachining Processing.* Journal of Microelectromechanical Systems, 1996. **5**: p. 256.
107. Kong, J., et al., *Nanotube Molecular Wires as Chemical Sensors.* science, 2000. **287**: p. 622.
108. Chen, C.-L., et al., *The heterogeneous integration of single-walled carbon nanotubes onto complementary metal oxide semiconductor circuitry for sensing applications.* Nanotechnology, 2009. **20**(22): p. 225302 (6pp).
109. Huang, Q., C.M. Lilley, and M. Bode, *Surface scattering effect on the electrical resistivity of single crystalline silver nanowires self-assembled on vicinal Si (001).* Applied Physics Letters, 2009. **95**(10): p. 103112.
110. Marom, H., J. Mullin, and M. Eizenberg, *Size-dependent resistivity of nanometric copper wires.* Phys. Rev. B, 2006. **74**(4): p. 045411.

111. Wu, W., et al., *Influence of surface and grain-boundary scattering on the resistivity of copper in reduced dimensions.* Applied Physics Letters, 2004. **84**(15): p. 2838-2840.
112. Khanal, B.P. and E.R. Zubarev, *Purification of High Aspect Ratio Gold Nanorods: Complete Removal of Platelets.* Journal of the American Chemical Society, 2008. **130**(38): p. 12634-12635.
113. Abermann, R. and R. Koch, *The internal stress in thin silver, copper and gold films.* Thin Solid Films, 1985. **129**(1-2): p. 71-78.
114. Kowalewski, T. and J. Legleiter, *Imaging stability and average tip-sample force in tapping mode atomic force microscopy.* Journal of Applied Physics, 2006. **99**(6): p. 064903.
115. *Handbook of Nanotechnology*, ed. B. Bhushan. 2010: Springer.
116. Sulchek, T., et al., *Characterization and optimization of scan speed for tapping-mode atomic force microscopy.* Review of Scientific Instruments, 2002. **73**(8): p. 2928-2936.
117. He, R., et al., *Self-Transducing Silicon Nanowire Electromechanical Systems at Room Temperature.* Nano Letters, 2008. **8**(6): p. 1756-1761.
118. Kuczynski, G.C., *Effect of Elastic Strain on the Electrical Resistance of Metals.* Phys. Rev., 1954. **94**(1): p. 61-64.
119. Ashcroft, N.W. and N.D. Mermin, *Solid State Physics*. 1976: Brooks Cole.
120. Parker, R.L. and A. Krinsky, *Electrical Resistance-Strain Characteristics of Thin Evaporated Metal Films.* Journal of Applied Physics, 1963. **34**(9): p. 2700-2708.
121. Lu, L., et al., *Ultrahigh Strength and High Electrical Conductivity in Copper.* Science, 2004. **304**(5669): p. 422-426.
122. Dingle, R.B., *The Electrical Conductivity of Thin Wires.* Proceedings of the Royal Society of London. Series A, Mathematical and Physical Sciences, 1950. **201**(1067): p. pp. 545-560.
123. Chambers, R.G., *The Conductivity of Thin Wires in a Magnetic Field.* Royal Society of London Proceedings Series A, 1950. **202**: p. 378-394.
124. Camacho, J.M. and A.I. Oliva, *Surface and grain boundary contributions in the electrical resistivity of metallic nanofilms.* Thin Solid Films, 2006. **515**(4): p. 1881-1885.
125. Rossnagel, S.M. and T.S. Kuan, *Alteration of Cu conductivity in the size effect regime.* Journal of Vacuum Science & Technology B: Microelectronics and Nanometer Structures, 2004. **22**(1): p. 240-247.
126. Liu, H.D., et al., *Thickness dependent electrical resistivity of ultrathin (<40 nm) Cu films.* Thin Solid Films, 2001. **384**(1): p. 151-156.
127. Lim, J.W., K. Mimura, and M. Isshiki, *Thickness dependence of resistivity for Cu films deposited by ion beam deposition.* Applied Surface Science, 2003. **217**(1-4): p. 95-99.
128. Novoselov, K.S., et al., *Electric Field Effect in Atomically Thin Carbon Films.* Science, 2004. **306**(5696): p. 666-669.
129. Bolotin, K.I., et al., *Ultrahigh electron mobility in suspended graphene.* Solid State Communications, 2008. **146**(9-10): p. 351-355.

130. Lee, C., et al., *Measurement of the Elastic Properties and Intrinsic Strength of Monolayer Graphene.* Science, 2008. **321**(5887): p. 385-388.
131. Pacile, D., et al., *The two-dimensional phase of boron nitride: Few-atomic-layer sheets and suspended membranes.* Applied Physics Letters, 2008. **92**(13): p. 133107.
132. Warner, J.H., et al., *Atomic Resolution Imaging and Topography of Boron Nitride Sheets Produced by Chemical Exfoliation.* ACS Nano, 2010. **4**(3): p. 1299-1304.
133. Zhi, C., et al., *Large-Scale Fabrication of Boron Nitride Nanosheets and Their Utilization in Polymeric Composites with Improved Thermal and Mechanical Properties.* Adv. Mater., 2009. **21**(28): p. 2889-2893.
134. Jin, C., et al., *Fabrication of a Freestanding Boron Nitride Single Layer and Its Defect Assignments.* Phys. Rev. Lett., 2009. **102**(19): p. 195505.
135. Alem, N., et al., *Atomically thin hexagonal boron nitride probed by ultrahigh-resolution transmission electron microscopy.* Phys. Rev. B, 2009. **80**(15): p. 155425.
136. Nag, A., et al., *Graphene Analogues of BN: Novel Synthesis and Properties.* ACS Nano, 2010. **4**(3): p. 1539-1544.
137. Corso, M., et al., *Boron Nitride Nanomesh.* Science, 2004. **303**(5655): p. 217-220.
138. J, V., et al., *A new bulge test technique for the determination of Young's modulus and Poisson's ratio of thin films*. 1992, Materials Research Society.
139. Namazu, T., Y. Isono, and T. Tanaka. *Nano-scale bending test of Si beam for MEMS.* in *Micro Electro Mechanical Systems, 2000. MEMS 2000. The Thirteenth Annual International Conference on.*
140. Ni, H., X. Li, and H. Gao, *Elastic modulus of amorphous SiO[sub 2] nanowires.* Appl. Phys. Lett., 2006. **88**(4): p. 043108.
141. Cuenot, S., et al., *Measurement of elastic modulus of nanotubes by resonant contact atomic force microscopy.* Journal of Applied Physics, 2003. **93**(9): p. 5650-5655.
142. Bunch, J.S., et al., *Impermeable Atomic Membranes from Graphene Sheets.* nanoletters, 2008. **8**: p. 2458-2462.
143. Song, L., et al., *Large Scale Growth and Characterization of Atomic Hexagonal Boron Nitride Layers.* Nano Letters, 2010. **10**(8): p. 3209-3215.
144. Small, M.K. and W.D. Nix, *Analysis of the accuracy of the bulge test in determining the mechanical properties of thin films.* Journal of Materials Research, 1992. **7**: p. 1553-1563.
145. Khurshudov, A.G., K. Kato, and H. Koide, *Wear of the AFM diamond tip sliding against silicon.* Wear, 1997. **203-204**: p. 22-27.
146. Tortonese, M. and M. Kirk, *Characterization of application-specific probes for SPMs.* Micromachining and Imaging, 1997. **3009**(1): p. 53-60.
147. Komaragiri, U., M.R. Begley, and J.G. Simmonds, *The Mechanical Response of Freestanding Circular Elastic Films Under Point and Pressure Loads.* Journal of Applied Mechanics, 2005. **72**(2): p. 203-212.
148. Zhang, R., et al., *Mechanical Characterization of Released Thin Films by Contact Loading.* Journal of Applied Mechanics, 2006. **73**(5): p. 730-736.
149. Frank, I.W., et al. *Mechanical properties of suspended graphene sheets*: AVS.

150. Kudin, K.N., G.E. Scuseria, and B.I. Yakobson, *C_{2}F, BN, and C nanoshell elasticity from ab initio computations.* Physical Review B, 2001. **64**(23): p. 235406.
151. Markiewicz, P. and M.C. Goh, *Atomic Force Microscopy Probe Tip Visulization and Improvement of Images Using a Simple Deconvolution Procedure.* Langmuir, 1994. **10**: p. 5-7.
152. Ju, S.-P., et al., *Phonon spectra in ultrathin gold nanowire under stretching.* Computational Materials Science, 2008. **42**(4): p. 595-599.
153. Lee, W.-J., et al., *Dynamical behaviour of 7-1 gold nanowire under different axial tensile strains.* Nanotechnology, 2006. **17**(13): p. 3253.

Appendix

Analytic expression of Root Mean Square for Chapter 2

I assumed RMSs of measurement data are independent of measurement time or frequencies $\sigma(x) \equiv \sigma$. Thus,

$$\sigma_{\omega_0} = \frac{\sigma}{\omega_0}\sqrt{\frac{\Delta x \int\left(\frac{\partial f}{\partial \xi}\right)^2}{\int\left(\frac{\partial f}{\partial \xi}\right)^2 dx \int\left(\frac{\partial f}{\partial \omega_0}\right)^2 dx - \left(\int\left(\frac{\partial f}{\partial \xi}\frac{\partial f}{\partial \omega_0}\right)dx\right)^2}}$$

$$\sigma_{\xi} = \frac{\sigma}{\xi}\sqrt{\frac{\Delta x \int\left(\frac{\partial f}{\partial \omega_0}\right)^2}{\int\left(\frac{\partial f}{\partial \xi}\right)^2 dx \int\left(\frac{\partial f}{\partial \omega_0}\right)^2 dx - \left(\int\left(\frac{\partial f}{\partial \xi}\frac{\partial f}{\partial \omega_0}\right)dx\right)^2}}$$

In frequency domain

$$\int\left(\frac{\partial f}{\partial \omega_0}\right)^2 dx = \frac{1}{32\omega_0}\left(\begin{array}{l}\dfrac{\left(-x^4+x^2-\sqrt{x^2-1}x+2\sqrt{x^2-1}x^3+1\right)\tan^{-1}\left(\dfrac{\omega}{\sqrt{2x^2+2\sqrt{x^2-1}x-1}\omega_0}\right)}{x^3\left(x^2-1\right)^{3/2}\sqrt{2x^2+2\sqrt{x^2-1}x-1}}- \\ \dfrac{\left(x^4-x^2-\sqrt{x^2-1}x+2\sqrt{x^2-1}x^3-1\right)\tanh^{-1}\left(\dfrac{\omega}{\sqrt{-2x^2+2\sqrt{x^2-1}x+1}\omega_0}\right)}{x^3\left(x^2-1\right)^{3/2}\sqrt{-2x^2+2\sqrt{x^2-1}x+1}}+ \\ \dfrac{16\omega\omega_0^5\left(\left(2x^2-1\right)\omega^2+\omega_0^2\right)}{\left(2\left(2x^2-1\right)\omega_0^2\omega^2+\omega^4+\omega_0^4\right)^2}+\dfrac{2\omega\omega_0\left(\left(2x^2-1\right)\omega^2+\left(-14x^4+14x^2+1\right)\omega_0^2\right)}{x^2\left(x^2-1\right)\left(2\left(2x^2-1\right)\omega_0^2\omega^2+\omega^4+\omega_0^4\right)}\end{array}\right)$$

$$\int\left(\frac{\partial f}{\partial \xi}\right)^2 dx = \frac{\omega_0}{32x^3}\left(\begin{array}{l}-\dfrac{3\left(3x^4-3x^2-\sqrt{x^2-1}x+2\sqrt{x^2-1}x^3+1\right)\tan^{-1}\left(\dfrac{\omega}{\sqrt{2x^2+2\sqrt{x^2-1}x-1}\omega_0}\right)}{\left(x^2-1\right)^{5/2}\sqrt{2x^2+2\sqrt{x^2-1}x-1}}+ \\ \dfrac{3\left(-3x^4+3x^2-\sqrt{x^2-1}x+2\sqrt{x^2-1}x^3-1\right)\tanh^{-1}\left(\dfrac{\omega}{\sqrt{-2x^2+2\sqrt{x^2-1}x+1}\omega_0}\right)}{\left(x^2-1\right)^{5/2}\sqrt{-2x^2+2\sqrt{x^2-1}x+1}}+ \\ \dfrac{16x^3\omega\omega_0^5\left(\left(2x^2-1\right)\omega^2+\omega_0^2\right)}{\left(x^2-1\right)\left(2\left(2x^2-1\right)\omega_0^2\omega^2+\omega^4+\omega_0^4\right)^2}-\dfrac{2x\omega\omega_0\left(\left(6x^2-3\right)\omega^2+\left(14x^4-14x^2+3\right)\omega_0^2\right)}{\left(x^2-1\right)^2\left(2\left(2x^2-1\right)\omega_0^2\omega^2+\omega^4+\omega_0^4\right)}\end{array}\right)$$

$$\int\left(\frac{\partial f}{\partial \xi}\frac{\partial f}{\partial \omega_0}\right)dx = -\frac{1}{32}x\omega_0^5\left(\begin{array}{l} -\dfrac{3\left(2x^2+\sqrt{x^2-1}x-1\right)\tan^{-1}\left(\dfrac{\omega}{\sqrt{2x^2+2\sqrt{x^2-1}x-1}\omega_0}\right)}{x^3\left(x^2-1\right)^{3/2}\sqrt{2x^2+2\sqrt{x^2-1}x-1}\omega_0^5}+ \\ \dfrac{3\left(-2x^2+\sqrt{x^2-1}x+1\right)\tanh^{-1}\left(\dfrac{\omega}{\sqrt{-2x^2+2\sqrt{x^2-1}x+1}\omega_0}\right)}{x^3\left(x^2-1\right)^{3/2}\sqrt{-2x^2+2\sqrt{x^2-1}x+1}\omega_0^5}- \\ \dfrac{32\omega^3}{\left(2\left(2x^2-1\right)\omega_0^2\omega^2+\omega^4+\omega_0^4\right)^2}-\dfrac{6\omega\left(\left(2x^2-1\right)\omega_0^2+\omega^2\right)}{x^2\left(x^2-1\right)\omega_0^4\left(2\left(2x^2-1\right)\omega_0^2\omega^2+\omega^4+\omega_0^4\right)} \end{array}\right)$$

In time domain

$$\int\left(\frac{\partial f}{\partial \xi}\right)^2 dx = \frac{e^{-2tx\omega_0}}{8x^3\left(x^2-1\right)\omega_0}\left(\begin{array}{l} 2t^2x^2\omega_0^2-\sqrt{1-x^2}x^3\left(2t^2\omega_0^2-1\right)\sin\left(2t\sqrt{1-x^2}\omega_0\right)+2tx\omega_0+1- \\ x^3\left(2t^2x\omega_0^2+2t\omega_0+x\right)\cos\left(2t\sqrt{1-x^2}\omega_0\right) \end{array}\right)$$

$$-\frac{1-x^4}{8x^3\left(x^2-1\right)\omega_0}$$

$$\int\left(\frac{\partial f}{\partial \omega_0}\right)^2 dx = \frac{e^{-2tx\omega_0}}{8x^3\omega_0^3}\left(\begin{array}{l} -2t^2x^2\omega_0^2-\sqrt{1-x^2}x^3\left(2t^2\omega_0^2-1\right)\sin\left(2t\sqrt{1-x^2}\omega_0\right)-2tx\omega_0-1- \\ -x^3\left(2t^2x\omega_0^2+2t\omega_0+x\right)\cos\left(2t\sqrt{1-x^2}\omega_0\right) \end{array}\right)-\frac{e^{-2tx\omega_0}}{8x^3\omega_0^3}$$

$$\int\left(\frac{\partial f}{\partial \omega_0}\frac{\partial f}{\partial \xi}\right)dx = \frac{e^{-2tx\omega_0}\left(\left(2t^2x\omega_0^2+2t\omega_0+x\right)\sin\left(2t\sqrt{1-x^2}\omega_0\right)-\sqrt{1-x^2}\left(2t^2\omega_0^2-1\right)\cos\left(2t\sqrt{1-x^2}\omega_0\right)\right)}{8\sqrt{1-x^2}\omega_0^2}-\frac{1}{8\omega_0^2}$$

Plots of the analytical formula taken with the same parameters as numerical calculations are shown in Figure 5-1 and agree well with numerical results.

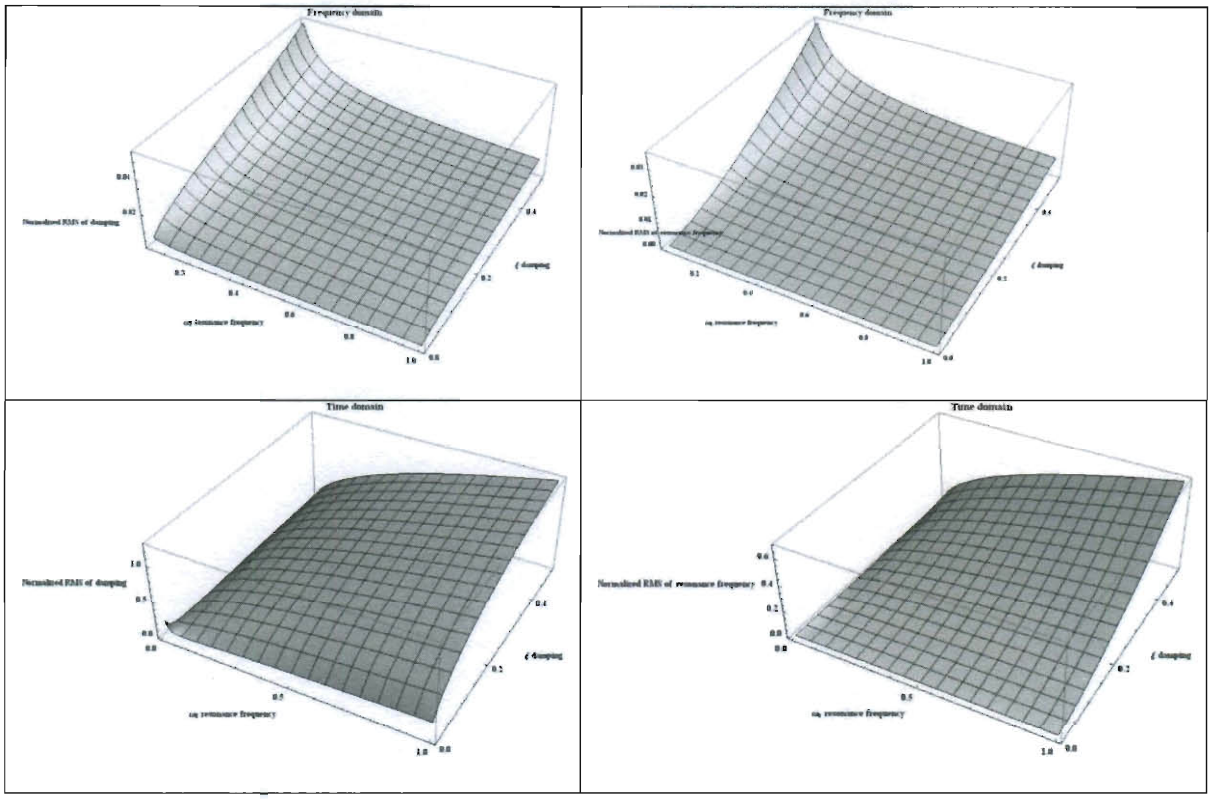

Figure 5-1, Plots of analytic formula for fitting errors in time domain and frequency domain

Design of AFM chamber

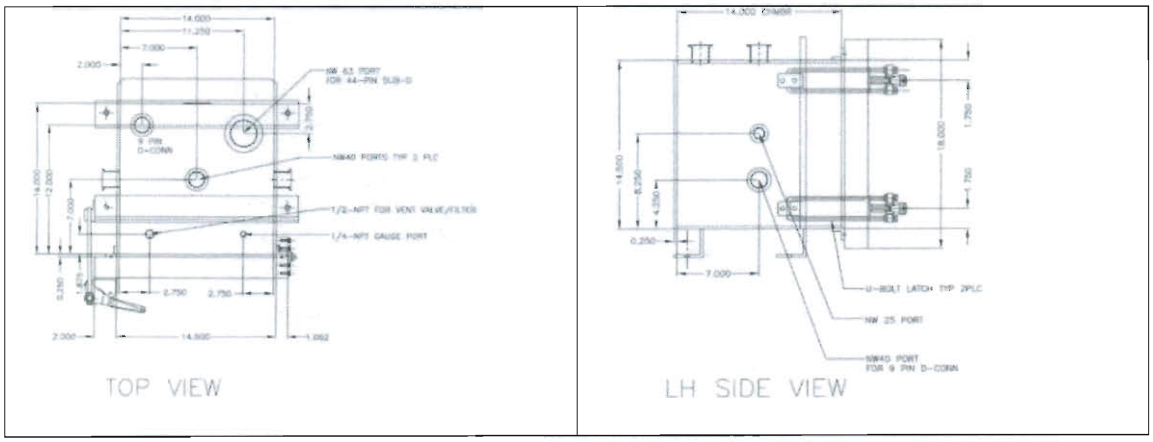

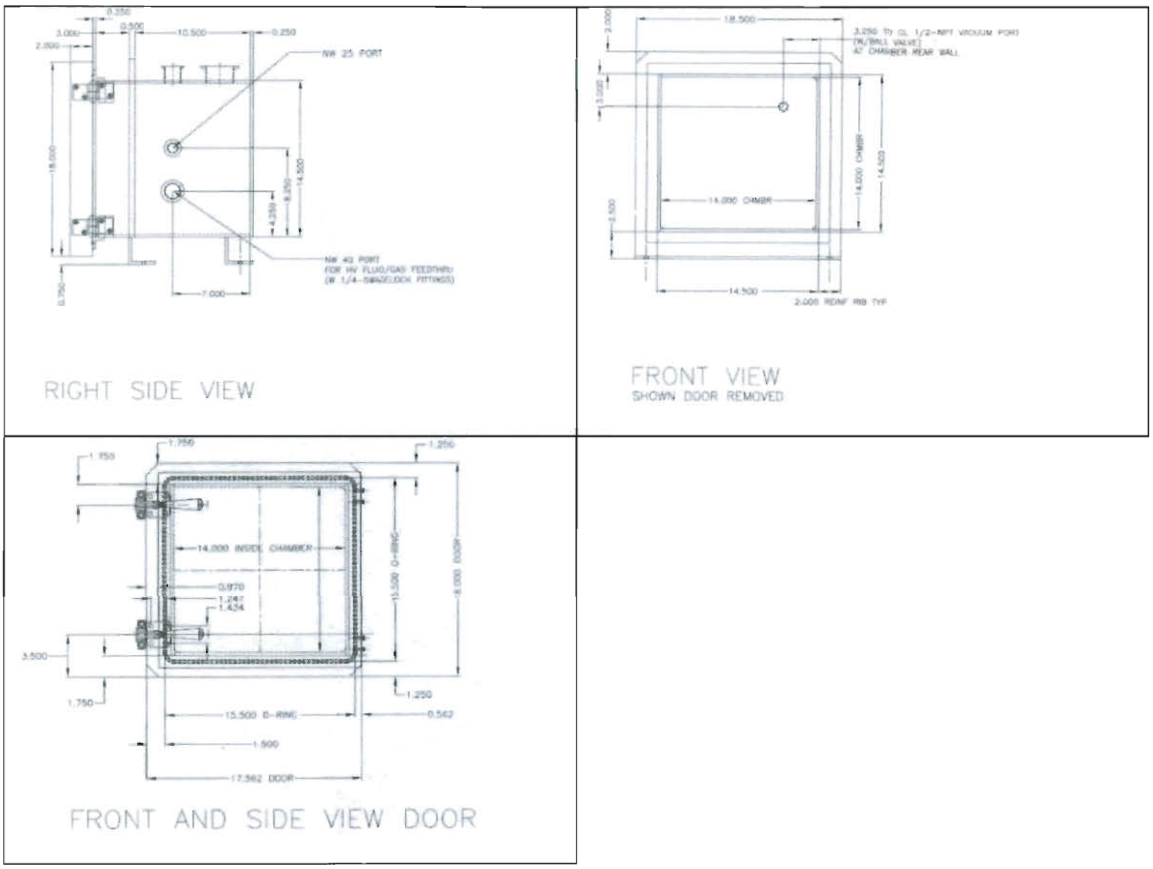

Figure 5-2, Environmental control chamber design

LabVIEW program

The Agilent 5500 AFM was controlled by PicoScan 5 software. This software enables ActiveX controls with rich set of methods and properties. The customized software used this feature to control the AFM and the source meter.

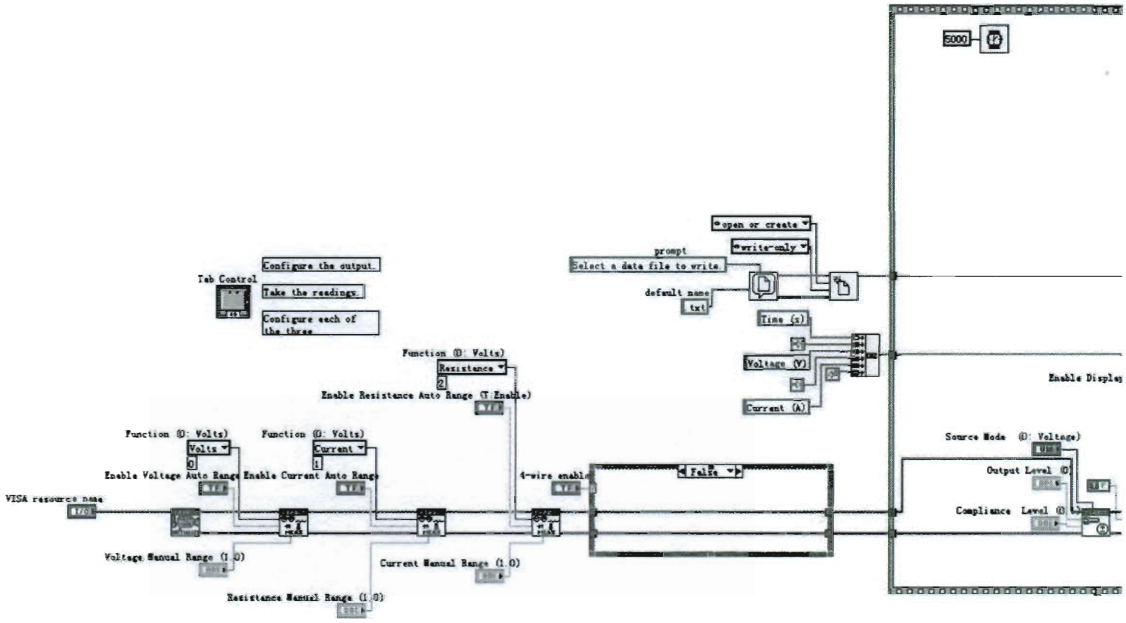

Figure 5-3 Block diagram this part initializes Keithley 2400

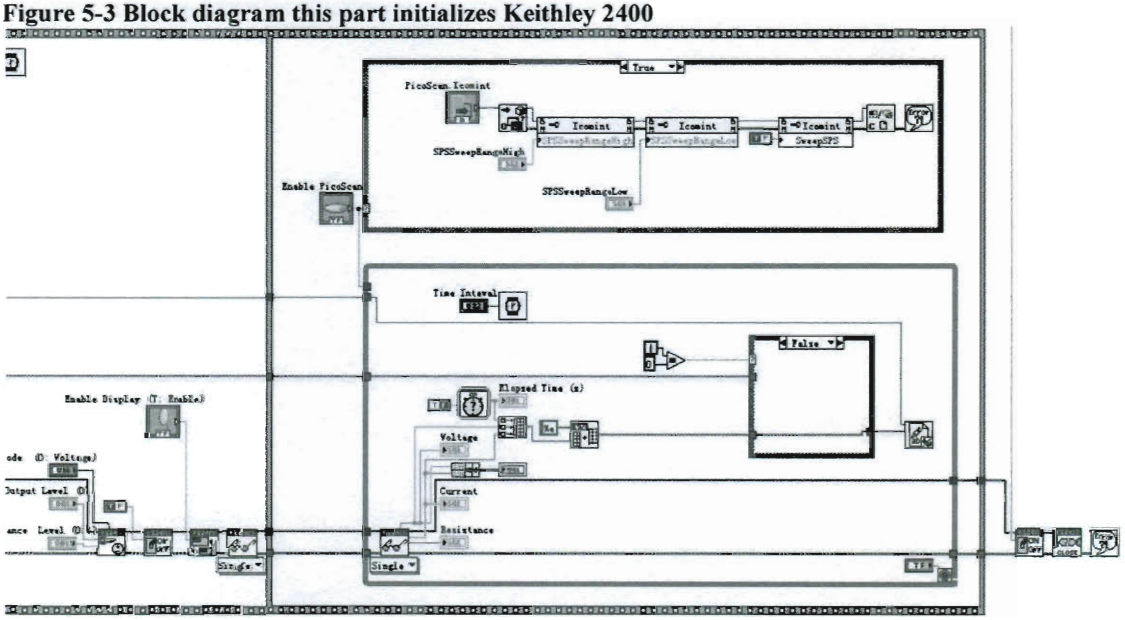

Figure 5-4 Block diagram, program first turn on Keithley 2400 and wait 5secs to let it set down then start to measure status of Keithley2400 and start up Force vs. Distance for AFM

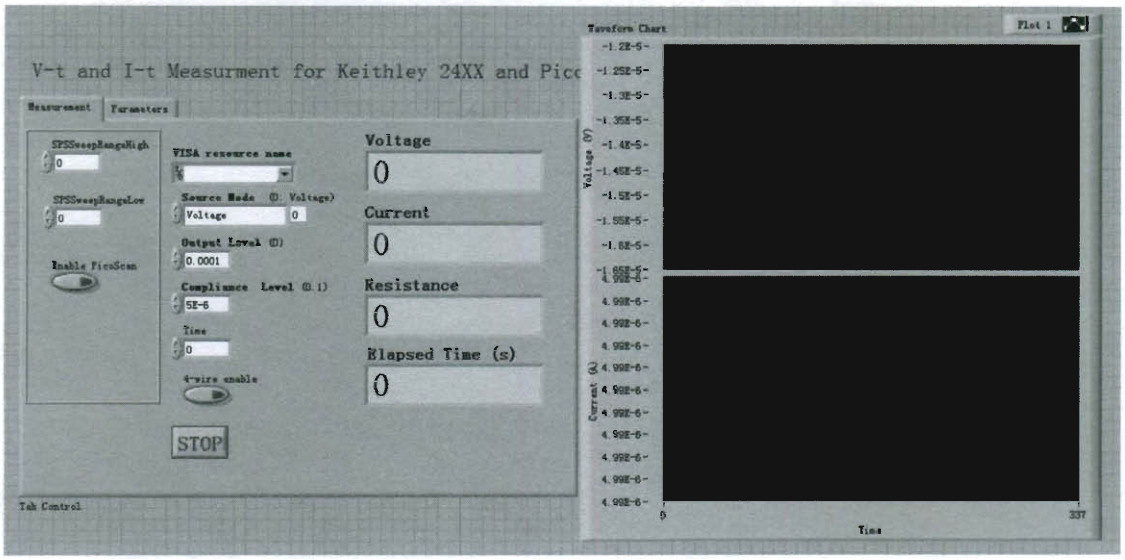

Figure 5-5, Front panel of synchronized electromechanical measurement LabVIEW program